

DEVELOPMENT AND EVALUATION OF  
EXCHANGE RATE MEASUREMENT METHODS

by

Edward A. Randtke

---

A Dissertation Submitted to the Faculty of the  
DEPARTMENT OF CHEMISTRY AND BIOCHEMISTRY

In Partial Fulfillment of the Requirements

For the Degree of

DOCTOR OF PHILOSOPHY

WITH A MAJOR IN CHEMISTRY

In the Graduate College

THE UNIVERSITY OF ARIZONA

2013

THE UNIVERSITY OF ARIZONA GRADUATE COLLEGE

As members of the Dissertation Committee, we certify that we have read the dissertation prepared by Edward Alexander Randtke entitled "Development and Evaluation of Exchange Rate Measurement Methods" and recommend that it be accepted as fulfilling the dissertation requirement for the Degree of Doctor of Philosophy.

\_\_\_\_\_  
L. Rene Corrales, Ph. D. Date: 12-06-13

\_\_\_\_\_  
Mark D. Pagel, Ph. D. Date: 12-06-13

\_\_\_\_\_  
Phillip Kuo, M.D., Ph. D. Date: 12-06-13

\_\_\_\_\_  
Julio Cárdenas-Rodríguez, Ph.D. Date: 12-06-13

Final approval and acceptance of this dissertation is contingent upon the candidate's submission of the final copies of the dissertation to the Graduate College.

I hereby certify that I have read this dissertation prepared under my direction and recommend that it be accepted as fulfilling the dissertation requirement.

\_\_\_\_\_  
Dissertation Director: L. Rene Corrales, Ph. D. Date: 12-06-13

\_\_\_\_\_  
Dissertation Director: Mark D. Pagel, Ph. D. Date: 12-06-13

## STATEMENT BY AUTHOR

This dissertation has been submitted in partial fulfillment of requirements for an advanced degree at the University of Arizona and is deposited in the University Library to be made available to borrowers under rules of the Library.

Brief quotations from this dissertation are allowable without special permission, provided that accurate acknowledgment of source is made. Requests for permission for extended quotation from or reproduction of this manuscript in whole or in part may be granted by the author.

SIGNED: Edward A. Randtke

## ACKNOWLEDGMENTS

It would not have been possible to complete the work in this thesis without the direct help from the following people:

L. Rene Corrales, Marty Pagel, Liu Qi Chen, Jie Min and Neil Jacobsen

The following provided helpful discussion that improved the work in this thesis:

Julio Cárdenas-Rodríguez and Oliver Monti

## DEDICATION

Dedicated to Friends and Family

## Contents

<i>List of Abbreviations</i> .....	8
<i>List of Tables</i> .....	10
<i>List of Figures</i> .....	10
<i>ABSTRACT</i> .....	12
<b>CHAPTER 1: INTRODUCTION TO THE QUANTIFICATION OF CHEMICAL EXCHANGE USING MAGNETIC RESONANCE TECHNIQUES</b> .....	<b>13</b>
1.1. <i>Introduction</i> .....	14
1.2. <i>Magnetic Resonance Imaging</i> .....	14
1.2.1. <i>MRI Detection Sensitivity</i> .....	15
1.2.2. <i>MR Chemical Shift</i> .....	16
1.2.3. <i>RF Power</i> .....	16
1.3. <i>MR Relaxation</i> .....	17
1.4. <i>Chemical Exchange Saturation Transfer</i> .....	18
1.4.1. <i>Bloch Fitting of CEST Spectra</i> .....	20
1.4.2. <i>Lorentzian Line Shape Fitting of CEST Spectra</i> .....	23
1.4.3. <i>Other Methods to Analyze CEST Spectra</i> .....	24
1.4.4. <i>CEST MR Acquisition Methods</i> .....	24
1.5. <i>Estimating Chemical Exchange Rates from CEST Spectra</i> .....	30
1.6. <i>Using the Chemical Exchange Rate as a Quantitative Imaging Biomarker</i> .....	31
1.7. <i>Conclusions</i> .....	33
<b>CHAPTER 2: THE HANES-WOOLF LINEAR QUESTP METHOD IMPROVES THE MEASUREMENTS OF FAST CHEMICAL EXCHANGE RATES WITH CEST MRI</b> .....	<b>34</b>
2.1. <i>Abstract</i> .....	35
2.2. <i>Introduction</i> .....	35
2.3. <i>Theory</i> .....	37
2.4. <i>Methods</i> .....	40
2.4.1. <i>Simulations</i> .....	40
2.4.2. <i>Experimental Studies</i> .....	41
2.5. <i>Results</i> .....	43
2.5.1. <i>Simulations</i> .....	43
2.5.2. <i>Experimental Results</i> .....	47
2.6. <i>Discussion</i> .....	51
2.7. <i>Conclusions</i> .....	53
<b>CHAPTER 3: THE RECIPROCAL LINEAR QUEST ANALYSIS METHOD FACILITATES THE MEASUREMENT OF CHEMICAL EXCHANGE RATES WITH CEST MRI</b> .....	<b>54</b>
3.1 <i>Abstract</i> .....	55
3.2 <i>Introduction</i> .....	55
3.3 <i>Theory</i> .....	57
3.4 <i>Methods</i> .....	58
3.4.1 <i>Simulations</i> .....	58
3.4.2 <i>Experimental Studies</i> .....	60
3.5 <i>Results</i> .....	62
3.5.1 <i>Simulations</i> .....	62
3.5.2 <i>Experimental Results</i> .....	63
3.6 <i>Discussion</i> .....	64
3.7 <i>Conclusions</i> .....	68
<b>CHAPTER 4: EXCITON SELF TRAPPING IN COVALENTLY BONDED DYE-SILICA SYSTEMS</b> .....	<b>69</b>
4.1. <i>Abstract</i> .....	70

4.2. Introduction.....	70
4.3. Theory.....	72
4.4. Methods.....	78
4.5. Results.....	83
4.6. Discussion.....	94
4.7. Conclusions.....	99
<b>CHAPTER 5: FUTURE DIRECTIONS.....</b>	<b>100</b>
5.1. Measuring Chemical Exchange Rates with CEST MRI Analysis Methods.....	101
5.1.1. Summary of Current Status.....	101
5.1.2. Further Method Developments.....	102
5.1.2.1. In vivo CEST-MRI Methods.....	102
5.1.2.2. Methods for Analysing CEST Spectra.....	102
5.1.2.3. Methods for Developing CEST Saturation Periods with Shaped Pulses.....	104
5.1.3. Biomedical Molecular Imaging Applications.....	106
5.2. Modelling Exciton Exchange Rates in Chemical Systems.....	108
5.2.1. Summary of Current Status.....	108
5.2.2. Weak Coupling.....	108
5.3. CEST Exchange Modelling.....	110
5.4. Preclinical & Clinical MRI.....	111
<b>APPENDIX A: REVIEW OF CALCULATIONS OF ELECTRON TRANSFER RATES.....</b>	<b>112</b>
A.1. Motivation for Developing Eyring-Landau-Zener Theory.....	113
A.2. Coupling.....	114
A.3. Adiabatic and Diabatic Basis.....	114
A.4. Exchange Models.....	116
A.4.1. Landau-Zener theory.....	116
A.4.2. Marcus theory.....	116
A.4.3. Eyring theory.....	117
<b>APPENDIX B: DERIVATION OF OMEGA PLOT, LINEAR QUEST, QUESP, QUEST AND QUESPT FROM THE BLOCH EQUATIONS.....</b>	<b>118</b>
B.1. Derivation of Omega Plot / Linear QUESP from the Bloch-McConnell Equations....	119
B.2. Derivation of QUEST from the Bloch McConnell Equations.....	121
<b>REFERENCES.....</b>	<b>124</b>
Chapter 1.....	124
Chapter 2.....	127
Chapter 3.....	128
Chapter 4.....	129
Chapter 5.....	131
Appendix A.....	132
Appendix B.....	132

**List of Abbreviations**

CERT	Chemical Exchange Rotation Transfer
CEST	Chemical Exchange Saturation Transfer
CI	Confidence Interval
CNR	Contrast to Noise Ratio
DFT	Density Functional Theory
DiaCEST	Diamagnetic CEST
DIIS	Direct Inversion of the Iterative Subspace
EH-Conc	Eadie-Hofstee Concentration
EH-QUEST	Eadie-Hofstee Quantifying Exchange with Saturation Power
ELZ	Eyring-Landau-Zener
FID	Free Induction Decay
FISP	Fast Imaging with Steady state free Precession
FLASH	Fast Low Angle Shot
FLEX	Frequency Labeled Exchange Transfer
FRET	Förster Resonance Energy Transfer
FT	Fourier Transform
HW-Conc	Hanes-Woolfe Concentration
HW-QUEST	Hanes-Woolfe Quantifying Exchange with Saturation Power
L-QUEST	Linear Quantifying Exchange with Saturation Time
LB-Conc	Lineweaver-Burke Concentration
LB-QUEST	Lineweaver-Burke Quantifying Exchange with Saturation Power
LOVARS	Length and Offset VARied Saturation
LZ	Landau-Zener
MEP	Minimum Energy Pathway
MRI	Magnetic Resonance Imaging
MR	Magnetic Resonance
MTR <sub>asym</sub>	Magnetization Transfer Ratio via asymmetry
NEB	Nudged Elastic Band
NMR	Nuclear Magnetic Resonance
OLED	Organic Light Emitting Diode
OPARACHEE	On-resonance Paramagnetic Chemical Exchange
ParaCEST	Paramagnetic CEST
Q	Quality Factor

QUESP	Quantifying Exchange with Saturation Power
QUESPT	Quantifying Exchange with Saturation Power and Time
QUEST	Quantifying Exchange with Saturation Time
QUESTRA	QUEST algorithm with ratiometric analysis
RARE	RApid imaging with Refocused Echos
RF	Radio Frequency
RL-QUEST	Reciprocal Linear Quantifying Exchange with Saturation Time
RMS	Root Mean Squared
SAR	Specific Absorption Ratio
SNR	Signal to Noise Ratio
SWIFT	SWEEPing Imaging with Fourier Transform
TDDFT	Time Dependant Density Functional Theory
TEOS	Tetraethyloxysilane
TRIM	Time domain Removal of Irrelevant Magnetization
UL-QUEST	Unitary Linear Quantifying Exchange with Saturation Time
WASSR	Water Saturation Shift Reference
WALTZ	Wonderful Alternating phase Technique for Zero residual splitting
ZAPI	Z-spectroscopy with Alternating Phase Irradiation
ZAPISM	Z-spectroscopy with Alternating Phase Irradiation and Sin Modulation

## **List of Tables**

Table 2.1: The estimated chemical exchange rates of iopromide (Hz). .....	50
Table 3.1: Estimates of chemical exchange rates (Hz) .....	63
Table 4.1: Transition energies and localization for various surface groups .....	84
Table 4.2: Vertical excitations found via TDDFT and DFT, 6-31+g* basis sets.....	85
Table 4.3: DFT vertical excitation energies at singlet minimum geometry.....	86
Table 4.4: DFT relaxation energies to minimum triplet geometry.....	86
Table 4.5: DFT vertical excitation energies at triplet minimum geometry .....	86
Table 4.6: DFT vertical excitation with eight substituents.....	87
Table 4.7: LZ transition probabilities with various sweep profiles. ....	92
Table 4.8: Exchange rate constants for butadienyl-silica system.....	93
Table 4.9: Exchange rate constants for allyl-butadienyl system. ....	93

## **List of Figures**

Figure 1.1: Free induction decay.....	19
Figure 1.2: CEST experiment.....	25
Figure 2.1: Lorentzian fitting.....	42
Figure 2.2: QUEST, QUESP and QUESPT simulation.....	43
Figure 2.3: Linear QUESP simulation .....	45
Figure 2.4: Linear concentration simulation .....	46
Figure 2.5: Nonlinear fitting of experimental data .....	47
Figure 2.6: Linear QUESP fitting of experimental data.....	48
Figure 2.7: Linear concentration fitting of experimental data.....	49
Figure 3.1: CEST spectra of iopromide.....	56
Figure 3.2: Linear QUEST simulation .....	59
Figure 3.3: Comparison of QUEST and RL-QUEST.....	61
Figure 3.4: Saturation Dependence of RL-QUEST.....	62
Figure 3.5: Estimation of $k_{ex}$ with RL-QUEST .....	65
Figure 3.6: Estimated exchange rate vs. saturation power .....	66
Figure 4.1: Model of excess spin density.....	82
Figure 4.2: Simulations of exchange rate as a function of coupling and energy deficit. ....	89
Figure 4.3: Probability measure as a function of time with linear sweep rate. ....	90
Figure 4.4: Probability measure as a function of time with parabolic sweep rate. ....	90
Figure 4.5: Probability measure as a function of time with linear sweep rate with added Brownian noise. ....	91
Figure 4.6: Total deviation of probability measure from unity.....	91
Figure 4.7: Diabatic and adiabatic energy levels for our silica-allyl dye system. ....	92
Figure 4.8: Snapshots from the minimum energy pathway for a silica-allyl system. ....	92
Figure 4.9: The simulated quantum yield as a function of decay. ....	94

Figure 4.10: The simulated emission intensity as a function of time. ....	94
Figure 5.1: Density of self trapped exciton states as a function of energy for our model cluster.....	109
Figure A.1: A visual representation of kinetic theories relevant to exciton transport. ....	113
Figure A.2: Energy level diagram of diabatic and adiabatic surfaces. ....	114
Figure A.3: Landau-Zener sweep.....	116

## ABSTRACT

Exchange rate determination allows precise modeling of chemical systems, and allows one to infer properties relevant to tumor biology such as enzyme activity and pH. Current exchange rate determination methods found via Contrast Enhanced Saturation Transfer agents are not effective for fast exchanging protons and use non-linear models. A comparison of their effectiveness has not been performed. In this thesis, I compare the effectiveness of current exchange rate measurement methods. I also develop exchange rate measurement methods that are effective for fast exchanging CEST agents and use linear models instead of non-linear models. In chapter 1 I review current exchange rate measurement methods. In chapter 2 I compare several of the current methods of exchange rate measurement, along with several techniques we develop. In chapter 3 I linearize the Quantifying Exchange through Saturation Transfer (QUEST) measurement method analogously to the Omega Plot method, and compare its effectiveness to the QUEST method. In chapter 4, I compare the effectiveness of current exchange rate theories (Transition State Theory and Landau-Zener theory) in the moderate coupling regime, and propose our own combined Eyring-Landau-Zener theory for this intermediate regime. In chapter 5 I discuss future directions for method development and experiments involving exchange rate determination.

## CHAPTER 1

### INTRODUCTION TO THE QUANTIFICATION OF CHEMICAL EXCHANGE USING MAGNETIC RESONANCE TECHNIQUES

## **1.1. Introduction**

Non-invasive biomedical imaging methods have revolutionized medical diagnoses. Current clinical imaging methods are primarily designed for anatomical identifications, such as the location, number, size, and shape of suspicious lesions (1). The ability to non-invasively and quantitatively assess morphological changes in diseased tissues provides opportunities to longitudinally monitor disease progression and response to therapy with excellent sensitivity. Some clinical imaging methods have also been developed to assess tissue function, such as cardiac flow and tumor angiogenesis (2,3). The ability to non-invasively quantify tissue function has substantially improved diagnostic specificity. More recently, the development of molecular imaging has provided opportunities to assess the molecular compositions of pathological tissues (4). However, molecular imaging methods are primarily limited to pre-clinical research studies with in vitro cell cultures and in vivo animal models, and few of these methods have been successfully translated to the clinic. A major impediment to the clinical translation of molecular imaging has been the quantification of imaging results that can provide sufficient sensitivity and specificity for assessing diseased tissues and treatment effects (5).

## **1.2. Magnetic Resonance Imaging**

Magnetic resonance imaging (MRI) has become a powerful tool within the armamentarium of biomedical imaging (6). MRI is generally considered to be a non-invasive diagnostic method. While it is possible to cause radio frequency (RF) burns from high RF power, or electrical burns from eddy currents generated by magnetic field gradients that are quickly ramped, the level of RF power and magnetic field gradients required for imaging is sufficiently low that physical damage from the imaging technique is not required in order to obtain images. These issues can be mitigated by preventing the hardware from exceeding the Specific Absorption Rate (SAR) that can cause damage to a patient.

MRI has many beneficial characteristics for anatomical, functional, and molecular imaging studies. Because the human body is transparent to RF radiation, there are no practical issues with penetration depth when imaging, providing opportunities to image deep tissues. MRI can generate three-dimensional images or a series of two-dimensional images that can represent the entire body volume. The quantity of protons in most tissues within the body is sufficient to generate images without requiring the injection of exogenous contrast agents (although chemical contrast agents may be included to improve image contrast and

increase measurement specificity in some types of studies). A variety of MRI protocols can generate different types of contrast, providing opportunities to optimize the MRI protocol for diagnosing specific pathologies.

### 1.2.1. MRI Detection Sensitivity

Unfortunately, the detection sensitivity of MRI is low, due to the inherent limitations as described by the physical chemistry of MRI. Like all fermions, protons have a half integer spin quantum number. Because a proton is charged, there is a magnetic moment along the axis about which it spins. This magnetic spin of each proton is aligned in a parallel ( $\uparrow$ ) or anti-parallel ( $\downarrow$ ) orientation with the external magnetic field. The ratio of the parallel and anti-parallel magnetic spins is modelled by the Boltzmann distribution (Eq. [1.1]).

$$\text{population}(\uparrow) = \exp\left(\frac{-E(\uparrow)}{kT}\right) \quad [1.1A]$$

$$\text{population}(\downarrow) = \exp\left(\frac{-E(\downarrow)}{kT}\right) \quad [1.1B]$$

$$\frac{\text{population}(\downarrow)}{\text{population}(\uparrow)} = \frac{\exp\left(\frac{-E(\downarrow)}{kT}\right)}{\exp\left(\frac{-E(\uparrow)}{kT}\right)} \quad [1.1C]$$

$$\frac{\text{population}(\downarrow)}{\text{population}(\uparrow)} = \exp\left(\frac{-(E(\downarrow)-E(\uparrow))}{kT}\right) \quad [1.1D]$$

$$\frac{\text{population}(\downarrow)}{\text{population}(\uparrow)} = \exp\left(\frac{-\Delta E}{kT}\right) \quad [1.1E]$$

Our research studies were performed at a magnetic field strength of 14.1 T. This equates to 600 MHz proton resonance frequency based on the gyromagnetic ratio ( $\gamma$ ) of 42.56 MHz/T for a proton. Our studies were performed at a temperature of 37.3°C (310.6 K). Also,  $\Delta E = h \nu$ , where  $h$  is Planck's constant ( $6.626 \times 10^{-34}$  Js) and  $\nu$  is the frequency of the proton in the magnetic field. Therefore, using the Boltzmann constant,  $k$  ( $1.381 \times 10^{-23}$  J K<sup>-1</sup>), the ratio shown in Eq. [1.1E] is 0.9999072. For every 1,000,000 magnetic spins, a net 46 magnetic spins are aligned parallel with the external field, known as the net spin. MRI can measure this net spin, yet detecting a sum of only 46 of every 1,000,000 magnetic spins demonstrates that MRI is a quite insensitive method of imaging. This restricts in-vivo MRI to detecting water, fat, and other materials that have a large amount of proton density. Our studies in chemical solutions were performed in water with only 10% D<sub>2</sub>O to address

the insensitivity of MR studies. Furthermore, we used ensemble averaging of MR acquisitions to obtain images with improved signal to noise during our research studies.

### 1.2.2. MR Chemical Shift

The unique magnetic resonance frequencies of protons in a magnetic field, known as the MR chemical shift, are a major advantage for MRI studies. Our research studies exploited the unique chemical shifts generated by two protons with different chemical shifts in the same molecule. Each proton in a different chemical environment within a molecule experiences a different electron density, which causes different electronic shielding that opposes the external magnetic field, resulting in a different effective net magnetic field experienced by each proton. The chemical shifts of each proton in the molecule are expressed in relation to a standard frequency ( $\omega_{\text{standard}}$ ) (Eq. [1.2A]). Furthermore, the effect of electronic shielding scales with the strength of the external magnetic field (Eq. 1.2B), so that the unique chemical shifts of each proton are typically expressed relative to the external magnetic field (also represented by  $\omega_{\text{standard}}$ ).

$$ppm = \left( \frac{\omega - \omega_{\text{standard}}}{\omega_{\text{standard}}} \right) \cdot 10^6 \quad [1.2A]$$

$$\omega = \gamma \cdot B \quad [1.2B]$$

where B is the external magnetic field,  $\gamma$  is the gyromagnetic ratio of the particle studied and  $\omega$  is the precession rate in Hz of the magnetic moment around the external magnetic field.

### 1.2.3. RF Power

An important consideration during MRI studies is the power of the RF pulse needed to excite the net spin from equilibrium, and to “saturate” the system to eliminate the net spin. Our studies carefully measured the RF power used for excitation and saturation, and the RF power of saturation was an important parameter of some of our analysis methods. The MR pulse power is typically expressed as field strength in units of  $\mu\text{T}$ . However, our studies expressed pulse power as a nutation rate in units of Hz, which is related to the field strength via the gyromagnetic ratio of the particle studied. The power density scales with the square of the nutation rate (Eq. [1.3]).

$$w = \gamma \cdot B_1 \quad [1.3]$$

Our RF power calibrations were affected by radiation damping (13), which arises from the interaction of the precessing net spin with an induced current in the coil surrounding the sample. The effect of this interaction is an added RF field caused by current induced in the coil that lags behind that of the applied RF field by  $90^\circ$ . This affects the phase of the signal in a way that depends on power of the excitation pulse, which makes power calibration challenging. Radiation damping is especially problematic with transceiver coils that have a high quality factor,  $Q$ , such as the transceiver coil used in our studies performed with a modern, state-of-the-art NMR spectrometer.

To mitigate the effects of radiation damping during RF power calibrations, we measured the RF power required to achieve a  $360^\circ$  pulse. The radiation damping RF field lags the tipping pulse  $90^\circ$  in phase at tip angles between  $0^\circ$  and  $180^\circ$ , then leads  $90^\circ$  in phase at tip angles between  $180^\circ$  and  $360^\circ$ . The end result is that radiation damping effects cancel for the  $360^\circ$  pulse, which provides a more accurate assessment of RF power. In addition, we reduced the effects of radiation damping on RF power calibrations by detuning the transceiver coil. This eliminated feedback from induced current in the coil with the sample. Also, detuning the coil subsequently required greater power to generate the same  $360^\circ$  pulse, which created a greater dynamic range of pulse durations that led to greater consistency between MR experiments.

Our RF power calibrations may have also been affected by arcing, also known as the bridging of electrical current between loops of wire in the transceiver coil. Arcing changes the impedance of the transceiver coil. In turn this changes the efficiency of power transmission to the sample. Because arcing is expected to be random, arcing should cause random changes in the detected MR signal. To address this potential pitfall, we decreased the power levels of the saturation pulses by 20 dB relative to the initial excitation pulse. The absence of random changes in MR signal detection validated that this low power did not cause arcing.

### **1.3. MR Relaxation**

The contrast in MR images is very sensitive to relaxation processes as excited net spin returns to equilibrium (14). As a collection of molecules tumbles, some of the molecules will tumble at the Rabi frequency for transferring energy between excited and relaxed spin states. This will drive protons near the tumbling molecule from an excited state towards

equilibrium, causing a process known as  $T_1$  relaxation. A characteristic relaxation time constant,  $T_1$ , describes the time for  $1-1/e$  (63.2%) of the excited net spin to return to equilibrium (Fig. 1.1). A second relaxation time constant,  $T_2$ , describes the time for  $1-1/e$  (63.2%) of the excited net spin to leave the plane perpendicular to the external magnetic field. Dipolar coupling between proximal magnetic spins can cause the  $T_2$  relaxation time constant to be shorter than the  $T_1$  time constant. However, our MR studies only depended on  $T_1$  relaxation processes, so that we considered the  $T_2$  time constant to be equal to the  $T_1$  time constant in our simulations and experimental analyses.

#### 1.4. Chemical Exchange Saturation Transfer

Chemical Exchange Saturation Transfer (CEST) provides an alternative mechanism for generating MR image contrast (7). A CEST MRI contrast agent functions by applying one or more low-power RF pulses at the specific chemical shift of a proton on the CEST agent. These pulses cause an equilibration of the magnetic spins that are aligned parallel and anti-parallel with the main magnetic field (i.e., Eq.[1.1E] becomes one), which eliminates the net magnetization that can be detected with MRI. These saturated protons on the agent exchange with unsaturated protons on water molecules, thereby transferring the saturation to the chemical shift of water. This process can be repeated tens to thousands of times before the net spin of the water is measured with MR methods, amplifying the effect of one CEST agent, which offsets the inherent insensitivity of MRI. An approximate formula describes the ratio of magnetization with and without the CEST agent (Eq.1.4).

$$\frac{M_s}{M_0} = \frac{1}{1+\chi T_1 k_{ex}} \quad (\text{valid when } \frac{M_s}{M_0} \approx 1) \quad [1.4]$$

where

$M_s$ ,  $M_0$ : Water MR signal amplitude with and without saturation, respectively

$\chi$ : the mole fraction of agent protons to water protons

$T_1$ : the lifetime of longitudinal magnetization in water

$k_{ex}$ : the chemical exchange rate from the agent to water

CEST agents are classified as non-metallic diamagnetic CEST (DIACEST) or metallic paramagnetic CEST (PARACEST) agents (8,9). The metal ion of a PARACEST agent can

create a hyperfine contact shift with an exchangeable proton on the agent, which can greatly increase the chemical shift of the proton. This allows faster exchanging protons to be resolved from water, and also facilitates the selective saturation of the chemical shift of the proton relative to water or other protons. However, some paramagnetic ions cause  $T_1$  relaxation, which decreases the CEST effect (15). In addition, some paramagnetic ions are potentially toxic, which negatively impacts clinical translation. Therefore, we elected to use a DIACEST agent for our studies, to investigate the ability to selectively detect specific protons, to improve the isolation of the CEST effect from  $T_1$  relaxation effects, and to improve the potential for clinical translation of our methodologies.

A variety of MRI acquisition and analysis methods that exploit the CEST effect have been developed during the last 15 years (16). All CEST MRI acquisition methods employ a CEST saturation period followed by a standard MRI acquisition period (10). The CEST saturation period is characterized by the saturation time, power and frequency, and bandwidth. Our NMR studies used a single continuous-wave saturation pulse for the entire saturation time period, which was set to a specific saturation power and frequency, and which had a bandwidth that was dependent on the saturation time period. Furthermore, our NMR studies used a simple pulse-acquire acquisition method because spatial

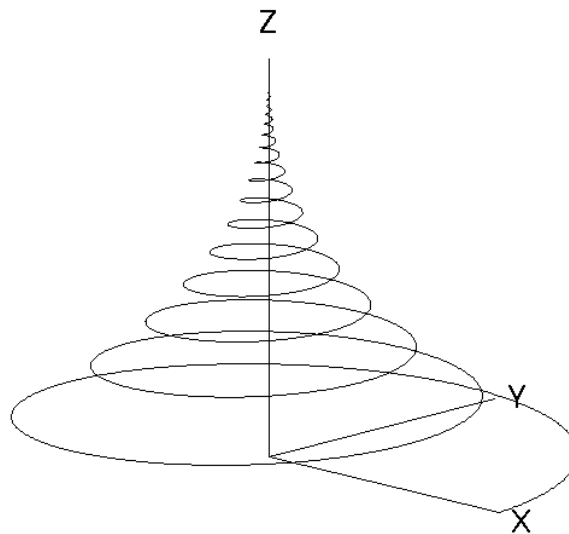


Figure 1.1: Free induction decay

The net spin in the Z direction aligned with the external magnetic field, and in the XY plan that is perpendicular to the external magnetic field. The net spin in the XY plane declines with a characteristic time constant,  $T_2$ , while the Z magnetization recovers with a characteristic time constant,  $T_1$ . This simulation used a rotating frame of reference that was 10 Hz off resonance from the Larmor frequency for water (600 MHz in our studies).

information was not required.

The traditional method of evaluating CEST consists of acquiring a series of MR spectra of water, where the selective saturation is iterated over a range of frequencies. A plot of the water amplitude vs. saturation frequency, known as a CEST spectrum, shows the CEST effect at the chemical shift of a CEST agent's labile proton, as well as the effect of direct saturation of water (11). The saturation frequency of the "CEST peak" in the CEST spectrum can be used to assign the CEST effect to a specific labile proton of the CEST agent. To eliminate effects of  $B_0$  magnetic field inhomogeneity (i.e., variations in the static magnetic field), the saturation frequency of the "direct saturation of water" peak is subtracted from the saturation frequency of the CEST peak. The amplitude of the CEST peak can be measured ( $M_s$  in eq. [1.4]) and compared with the water MR signal amplitude without saturation ( $M_0$  in eq. [1.4]) to analyze the chemical exchange rate ( $k_{ex}$  in Eq. [1.4]). The amplitude of the CEST peak can be estimated using Bloch fitting, Lorentzian line shape fitting, and other fitting methods as described below.

#### 1.4.1. Bloch Fitting of CEST Spectra

The Bloch-McConnell equations that describe the evolution of net magnetization during MRI protocols can be modified for chemical exchange (12). These equations are phenomenological differential equations that describe the dynamics of bar magnets in an external magnetic field (Eq. [1.5]).

$$\frac{d}{dt}M_x(t) = \gamma \cdot (M(t) \times B(t)) - \frac{M_x(t)}{T_2} \quad [1.5A]$$

$$\frac{d}{dt}M_y(t) = \gamma \cdot (M(t) \times B(t)) - \frac{M_y(t)}{T_2} \quad [1.5B]$$

$$\frac{d}{dt}M_z(t) = \gamma \cdot (M(t) \times B(t)) - \frac{M_z(t) - M_0}{T_1} \quad [1.5C]$$

These formulas can be written as a matrix of homogenous terms  $A$  (dependent on  $M(t)$ ) and inhomogeneous terms  $b$  (not dependent on  $M(t)$ ) as follows:

$$\frac{d}{dt}M(t) = A \cdot M(t) + b \quad [1.6A]$$

$$M(t) = \begin{bmatrix} M_x(t) \\ M_y(t) \\ M_z(t) \end{bmatrix} \quad [1.6B]$$

$$A = \begin{bmatrix} -\frac{1}{T_2} & -(\omega_{larmor} - \omega_{RF}) & -\omega_{mutation} \ y \\ (\omega_{larmor} - \omega_{RF}) & -\frac{1}{T_2} & -\omega_{mutation} \ x \\ \omega_{mutation} \ y & \omega_{mutation} \ x & -\frac{1}{T_1} \end{bmatrix} \quad [1.6C]$$

$$b = \begin{bmatrix} 0 \\ 0 \\ \frac{M_0}{T_1} \end{bmatrix} \quad [1.6D]$$

where

$$\omega_{mutation} \ x = \gamma \cdot B_x \quad [1.7A]$$

$$\omega_{mutation} \ y = \gamma \cdot B_y \quad [1.7B]$$

$M_0$  is the thermal equilibrium magnetization of the proton pool, and  $B_x$  and  $B_y$  are the magnetic field of the RF irradiation about the x and y axis in the rotating frame of reference.

The modifications for chemical exchange in a two state system are included by combining the Bloch equation matrices with the exchange rate matrix.

$$K = \begin{bmatrix} -k_{ab} & k_{ba} \\ k_{ab} & -k_{ba} \end{bmatrix} \quad [1.8]$$

Using the equilibrium approximation:

$$k_{ab} M_a = k_{ba} M_b \quad [1.9A]$$

$$k_{ab} = k_{ba} \frac{M_b}{M_a} \quad [1.9B]$$

where  $M_a$  is the solvent and  $M_b$  is a solute, then:

$$k_{ab} = k_{ba} \chi \quad [1.10]$$

Where  $\chi$  is the mole fraction of solute to solvent, and

$$K = \begin{bmatrix} -k_{ba} \chi & k_{ba} \\ k_{ba} \chi & -k_{ba} \end{bmatrix} \quad [1.11]$$

Combining Eqs. [1.6C] and [1.11],

$$A_{exchange} = \begin{bmatrix} A_{solvent} & 0 \\ 0 & A_{solute} \end{bmatrix} + K \otimes \begin{bmatrix} 1 & 0 & 0 \\ 0 & 1 & 0 \\ 0 & 0 & 1 \end{bmatrix} \quad [1.12]$$

Where  $A_{solvent}$  is the homogenous part of the Bloch equations of the solvent magnetization, and  $A_{solute}$  the homogenous part of the Bloch equations for the solute, and  $\otimes$  is the Kronecker product.

This gives:

$$A = \begin{bmatrix} -\frac{1}{T_2 solvent} - k_{ba}\chi & -(\omega_{larmor solvent} - \omega_{RF}) & -\omega_{nutatation y} & k_{ba} & 0 & 0 \\ (\omega_{larmor solvent} - \omega_{RF}) & -\frac{1}{T_2 solvent} - k_{ba}\chi & -\omega_{nutatation x} & 0 & k_{ba} & 0 \\ \omega_{nutatation y} & \omega_{nutatation x} & -\frac{1}{T_1 solvent} - k_{ba}\chi & 0 & 0 & k_{ba} \\ k_{ba}\chi & 0 & 0 & -\frac{1}{T_2 solute} - k_{ba} & -(\omega_{larmor solute} - \omega_{RF}) & -\omega_{nutatation y} \\ 0 & k_{ba}\chi & 0 & (\omega_{larmor solute} - \omega_{RF}) & -\frac{1}{T_2 solute} - k_{ba} & -\omega_{nutatation x} \\ 0 & 0 & k_{ba}\chi & \omega_{nutatation y} & \omega_{nutatation x} & -\frac{1}{T_1 solute} - k_{ba} \end{bmatrix} \quad [1.13]$$

with a non-homogenous part:

$$b = \begin{bmatrix} b_{solvent} \\ b_{solute} \end{bmatrix} \quad [1.14]$$

$$b = \begin{bmatrix} 0 \\ 0 \\ \frac{M_0 solvent}{T_1 solvent} \\ 0 \\ 0 \\ \frac{M_0 solute}{T_1 solute} \end{bmatrix} \quad [1.15]$$

Here,  $M_0$  is the magnetization of the pool at thermal equilibrium.

The differential equation for the chemically exchanging system in an external magnetic field is:

$$\frac{d}{dt}M(t) = A \cdot M(t) + b \quad [1.16]$$

with

$$M(t) = \begin{bmatrix} M_{solvent}(t) \\ M_{solute}(t) \end{bmatrix} \quad [1.17A]$$

$$M(t) = \begin{bmatrix} M_{x\ solvent}(t) \\ M_{y\ solvent}(t) \\ M_{z\ solvent}(t) \\ M_{x\ solute}(t) \\ M_{y\ solute}(t) \\ M_{z\ solute}(t) \end{bmatrix} \quad [1.17B]$$

These are coupled first order differential equations that can be solved via the usual methods. The integrating factor method was used to solve these equations in this manuscript. We build a propagator using the scaling and squaring method approximation for the matrix exponential. Also, we extended the matrices to 3 solutes using the above method of exchange plus Bloch equations in order to account for the multiple exchanging protons in the agents analyzed.

No care needs to be taken to ensure time invariant approaches to the solution are used since these formulas relax to equilibrium over time (all eigenvalues of the propagator matrix A are negative). Error introduced in the solution will disappear to zero as the system propagates.

The Bloch equations are fit via a non-linear least squares method, thus the least squares solution is not unique. This means that a substantial amount of data is needed to insure that a precise and accurate fit is obtained. Evidence that the global minimum is found and the model is complete is a residual with a Gaussian distribution about zero.

#### **1.4.2. Lorentzian Line Shape Fitting of CEST Spectra**

Lorentzian fitting is a method of fitting models of the form

$$u = e^{(i\omega + k)t} \quad [1.18]$$

For MRI and NMR,  $\omega$  is the Larmor frequency of a pool while k is a sum of all rates that result in a loss of magnetization from the xy plane of a particular pool, such as spin-spin relaxation, chemical exchange of protons and nutation rate. Lorentzian line shapes are fit in frequency space using the Fourier transform of [1.18]:

$$CEST = \sum_{i=1}^{\text{number of pools including water}} \frac{1}{\pi} \cdot \frac{\frac{1}{2}\Gamma_i}{(\omega - \omega_{0i}) + (\frac{1}{2}\Gamma_i)^2} \quad [1.19]$$

This fitting deconvolutes overlapping proton pools when fitting CEST spectra and accounts for B0 inhomogeneities in the sample. Because the Lorentzian model is not linear with respect to the fitted parameters, it suffers from the disadvantages of non-linear fitting, such as non-unique solutions to the least squares system of equations relating predictors and response and susceptibility to noise (17) (18).

### **1.4.3. Other Methods to Analyze CEST Spectra**

There are processing methods that can assist with fitting CEST spectra. Smoothed cubic splines (19), inverse FT (20) and variational Bayesian inference (21) have been used to accommodate noise during data analysis. An issue with fitting CEST spectra is outliers from noisy spectra can affect fitting of spectra. These methods all mitigate outliers.

Smoothed cubic splines minimize both the residual and the integral of the 2<sup>nd</sup> derivative of a function. This gives a spline that follows the data well without over fitting into noisy data, as fitting data that deviates greatly from the spline curve requires a large 2<sup>nd</sup> derivative. This has been shown to improve Lorentzian line fitting (19).

Inverse Fourier Transforming a CEST spectra and fitting the FID like signal via the Time domain Removal of Irrelevant Magnetization (TRIM) method has been shown to be effective in mitigate the effects of noise compared to Lorentzian fitting (20). By weighting the noise in the time domain instead of in the frequency domain, the consistency and repeatability of fitting even under was improved.

Variational Bayesian inference includes regularization based on the SNR of the data. As SNR declines, regularization adapts to prevent over fitting of noise.

### **1.4.4. CEST MR Acquisition Methods**

We chose to study CEST with the traditional CEST Z-spectrum to avoid complications with more sophisticated methods while investigating the accuracy and precision of measuring chemical exchange rates. The paradigm for a traditional CEST experiment is to prepare the system with a saturation pulse at the MR frequency of the labile proton pool, image the water pool to observe the amplitude of the water signal, and process the imaging results.

Imaging schemes that use this traditional approach include CEST-FLASH (22), CEST-RARE (22), CEST-FISP (23), or SWIFT-CEST (24), while processing can be performed via methods like the keyhole CEST (25). For each of these traditional methods, the physical response of the system is solely determined by the preparatory saturation method.

Among the traditional CEST MRI experiments, two acquisition methods provide additional advantages that warrant discussion. The SWIFT acquisition method measures the spin density along one direction in a sample, without loss of signal from  $T_1$ - or  $T_2$ -weighting. The spin densities along multiple directions can be used to reconstruct the original spin density of the material. Therefore, CEST-SWIFT can measure CEST in samples with short  $T_1$ - or  $T_2$ -relaxation times.

Keyhole imaging refers to a fast data collection at the center of K-space (the “keyhole”), which contains the majority of contrast information. The absence of information at the edges of K-space causes a loss of spectral resolution. However, the low resolution, high contrast image can be overlaid on a high resolution MR image to locate the contrast agent within the image. The high contrast image is well suited for the quantification of CEST, because CEST is itself a contrast of image signals with and without saturation.

Traditional CEST contrast is typically quantified as a ratio of signal with contrast agent present to signal without contrast agent present. However, water will be partly saturated even if the MR frequency of the saturation pulse is off resonance relative to the water frequency. One way to account for the direct saturation of water is by performing another experiment with selective saturation at the same MR frequency from water but in the opposite direction from the labile pool. This is called the mirror method, or the magnetization

transfer ratio  
asymmetry  
( $MTR_{asy,m}$ ) method  
(26). The  $MTR_{asy,m}$   
spectrum is  
obtained by  
measuring the  
ratio of the water  
signal after

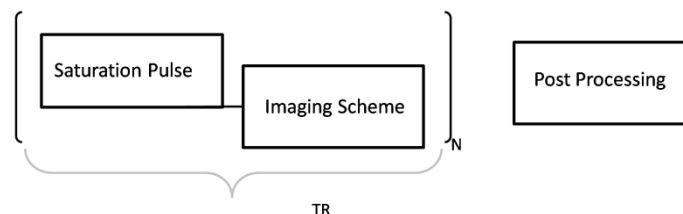


Figure 1.2: CEST experiment

Paradigm for a CEST MRI experiment. The preparatory saturation method, imaging scheme and post processing are typically modular and independent of each other.

saturation with frequencies mirrored on either side of the water resonance frequency. The MTR asymmetry is defined with the following formula:

$$MTR_{asym} = \frac{M_- - M_+}{M_-} \quad [1.19]$$

$M_+$  is the water signal after on resonance saturation of a pool, and  $M_-$  is the water signal after saturation at an offset on the opposite side of the frequency of the water pool. This value is used to measure the amplitude of the CEST effect, the chemical exchange rate, or other related parameters.

The  $MTR_{asym}$  image map will be incorrect if the water resonance frequency is different for every voxel in the MRI image, due to inhomogeneity in the static magnetic field ( $B_0$ ) throughout the tissues being imaged. The WASSR method can be used to measure  $B_0$  inhomogeneity throughout the image by acquiring a CEST spectrum with very high frequency resolution about the putative water resonance frequency (27). Alternatively, the full CEST spectrum can be analysed via Lorentzian line shape fitting or Bloch fitting, which can deconvolute each of the labile proton pools from themselves and from water, without dependence on the  $B_0$  magnetic field inhomogeneities. We elected to use Bloch fitting and Lorentzian line shape fitting in our methodology to avoid complications from  $B_0$  inhomogeneities.

The TRIM method is an alternative approach for analyzing CEST spectra (20). This method transforms a CEST spectrum from the frequency domain to the time domain. This enables one to easily remove the effects of off resonance saturation of water from the CEST spectrum. While there is a 1:1 mapping between the time domain and frequency domain, transforming to the time domain weights points differently when fitting data. The authors demonstrated that with additional simulated noise, the TRIM method was able to fit their data with more repeatability than when fitting via the Lorentzian lineshape fitting method. This method can be used to eliminate direct saturation of water, which can improve the measurement of the chemical exchange rate, yet we did not use this method for our studies because our model system, iopromide, has multiple broad overlapping peaks that cannot be fit well in the time domain.

Spin locking can also be used to generate CEST effects (28). A saturation pulse can be turned into a spin locking pulse by tipping the proton pool magnetization so that it lines up with the rotating frame  $B_1 + B_0$  magnetization of the CEST saturation pulse during

saturation, then tipping it back at the end of saturation. The water signal of this experiment can be compared to a second experiment that includes an inversion pulse, which points the magnetic vector opposite that of the  $B_1 + B_0$  magnetization of the CEST saturation pulse. This method effectively generates contrast based on the rate that the system approaches steady state. At long saturation times, this is equivalent to a traditional CEST preparation pulse. At extremely short saturation times, tipping and spin-locking the labile proton signal can potentially suppress artifacts from the sinc lineshape in frequency space. Our studies used relatively long saturation times, and therefore the potential advantages of spin-lock pulses were not required for our studies.

As an alternative method to traditional CEST MRI, the Chemical Exchange Rotation Transfer (CERT) MRI technique measures CEST contrast after a saturation flip angle of  $360^\circ$  and  $540^\circ$ , compared to CEST contrast with a flip angle of  $180^\circ$  as a control experiment. By taking a ratio of these experiments, all factors affecting image contrast are cancelled except for the chemical exchange rate of the CEST agent. Therefore, CERT can measure the chemical exchange rate by varying the power and time of saturation pulses while maintaining flip angles of  $180^\circ$ ,  $360^\circ$  and  $540^\circ$ . Relative to traditional CEST methods that iterate the saturation frequency, CERT has the advantage of using a single saturation frequency. This prevents asymmetry in the Z-Spectrum from affecting the detected contrast. However, imprecise flip angles cause a dependence on the concentration, which can complicate the measurement of the chemical exchange rate. For this reason, we elected to use traditional CEST MRI methods for our analyses (29) (30).

The Positive CEST MRI method (31) applies a hard  $180^\circ$  inversion pulse to the entire system, then applies a long saturation pulse as in a typical CEST experiment. Saturation of the labile proton pool tips the inverted magnetization of the labile pool so it is not anti-aligned with the static magnetic field. Chemical exchange allows these unaligned protons to exchange to water, which accelerates the rate of alignment of water with the static magnetic field, so there will be higher signal from water with saturation than without saturation when the pulse-acquire part of the CEST experiment is performed. This positive signal gives rise to the name Positive CEST MRI. As an advantage, the saturation time can be selected to coincide with the time at which the longitudinal magnetization of the water is nulled, so that water that is not involved in chemical exchange with the agent will produce no signal. If the  $T_1$  time is not consistent, or is otherwise different than the  $T_1$  time used to select the saturation time, then the signal from water will not be zero in voxels that

have  $T_1$  times different than the  $T_1$  time used to select the saturation time. Since the signal without agent is zero at the end of saturation, no control experiment needs to be performed to measure the magnetization of water without agent. This method can, in principle, be used to measure the chemical exchange rate by varying the saturation time. However, an analytical solution has not been developed that converts the results of Positive CEST to a chemical exchange rate. Also, the assumption that  $T_1$  of water will be the same with and without agent present is a poor assumption; the addition of solute is expected to affect the  $T_1$  of water. For these reasons we do not use Positive CEST when analysing exchange rates.

The OPARACHEE method (32, 33, 34) performs the traditional CEST experiment in reverse by applying RF pulses at the water resonance frequency. In an OPARACHEE experiment, an RF WALTZ pulse is applied on resonance with the water pool to cause a  $360^\circ$  rotation of the water magnetization. During this pulse, chemical exchange of a proton from a CEST agent to water will cause this proton to only experience the remainder of the pulse applied to the water resonance. Protons that experience the full  $360^\circ$  pulse can produce a full signal, while protons that experience only part of the  $360^\circ$  pulse can only produce part of a signal. Therefore, at the end of the WALTZ pulse, the resulting magnetization in the Z direction will be smaller if the chemical exchange rate is faster. The chemical shift difference between the CEST agent and water also influences the OPARACHEE contrast.

The effects of chemical exchange between water and all of the labile proton pools sum together to generate contrast in an OPARACHEE experiment. For this reason, only one saturation experiment with an on resonance saturation of water is needed to generate a contrast image. For comparison, a traditional CEST experiment requires multiple saturation experiments at different saturation offsets for proper analyses. However, this additive effect prevents OPARACHEE from deconvoluting the effects of multiple tissues and labile proton pools. Our research required the study of multiple labile proton pools, which obviated the use of OPARACHEE. Furthermore, no current method yet exists that has been developed to measure chemical exchange using OPARACHEE. For these reasons we did not use OPARACHEE and instead used traditional CEST.

The FLEX MRI method (35, 36, 37) is an inherently different approach for detecting CEST. The FLEX pulse sequence measures the Fourier transform of a CEST spectrum. This is

accomplished by applying two pulses  $180^\circ$  out of phase separated by a time  $T_{\text{evol}}$ . This tips magnetization that precesses  $180 + 360 \cdot n$  degrees around the  $B_0$  axis in time  $T_{\text{evol}}$ . This corresponds to inverting proton pools in a sinusoidal fashion, with peak inversion at chemical shifts of  $1/(2 \cdot T_{\text{evol}}) + 1/(T_{\text{evol}})$  Hz from the frequency at which the RF pulses are applied. By then allowing the protons to exchange for time  $T_{\text{exch}}$ , the inverted magnetization will exchange with water, suppressing the magnetization of water. By repeating this process for many different  $T_{\text{evol}}$  periods, the Fourier transform of the CEST spectrum is directly acquired. The original CEST spectrum can thus be obtained by Fourier transforming the FLEX spectrum and removing the zero frequency components corresponding to the baseline of the FLEX spectrum. The pools can then be fit via Lorentzian line shape fitting of the CEST spectrum or by fitting the FID curves for each peak of the FLEX spectrum.

The spectral window of proton pools excited via FLEX is determined by the time of the tipping pulses and RF pulse frequency, so that it is possible to selectively excite labile pools with minimal direct saturation of water. As an additional advantage, the FLEX method acquires signal from the labile pool with every FLEX labelling experiment. With the traditional CEST technique, only CEST experiments with a presaturation pulse near the resonant frequency of the labile pool generate contrast. Thus, FLEX MRI can generate good results in the presence of  $B_0$  inhomogeneity, while this inhomogeneity is more problematic for traditional CEST imaging methods.

A disadvantage of the FLEX method is the limited signal from labile pools for each FLEX experiment. This is balanced by the ability to generate many points with signal that will add together to generate contrast after FLEX analysis, if the FLEX FID does not decay rapidly. Thus, analysis of the FLEX FID should produce comparable results to a CEST spectrum. However if the CEST agent has multiple labile pools with vastly different exchange rates, and thus line widths of the two CEST effects of the agent are also vastly different, then the FLEX FID signal of the rapidly exchanging pool will disappear very rapidly, and suffer from the poor FLEX signal without the benefit of averaging many FID points. Because we studied systems with multiple labile pools with an order of magnitude difference between exchange rates, we chose not to use FLEX for analysis. Yet in principle, FLEX MRI this can be used to measure exchange rates by Fourier transforming the FLEX spectrum into the frequency domain.

The Length and Offset VARied Saturation (LOVARS) technique (38) performs an  $MTR_{asym}$  analysis at two saturation times, then evaluates a ratio of CEST signal generated with the two saturation times. The results are equivalent to a 2 point Quantifying Exchange through Saturation Transfer Ratiometric Approach (QUESTRA) (41) experiment in terms of accuracy, precision, and the MRI/NMR experiments performed. Since the technique is equivalent to a 2 point QUESTRA experiment, and exchange rate can be measured using QUESTRA, this method can be used to measure chemical exchange rates. While the LOVARS phase angle has a higher CNR than that found via  $MTR_{asym}$  method, it is not clear if the CNR of the two methods are directly comparable; with no agent present the phase angle found via LOVARS will be  $45^\circ$ . Thus there is always contrast included in the LOVARS phase angle that provides no information about the labile proton pool. Therefore, we focused on traditional CEST MRI methods for our analysis.

The Z-spectrum with Alternating Phase Irradiation (ZAPI) method (39) uses a series of square-shaped saturation pulses with alternating phase. This has the effect of splitting the irradiation frequency into multiple sidebands. ZAPI with a Sine waveform (ZAPIS) (39) splits the irradiation frequency into two bands. When the CEST spectra are acquired, the ZAPI experiment uses an alternating phase block pulse waveform, while a control experiment uses a block pulse with no phase cycling. The alternating phase has the effect of applying RF power at  $\pm (1/2+n)/t$ , where  $n$  is an integer and  $t$  is the period of the sine or block wave. This is similar to the FLEX method which applies RF power at  $\pm (1/2+n)/T_{evol}$ .

If the period is selected appropriately, the ZAPI method can improve  $MTR_{asym}$  measurements of CEST. (39,40) The multi-bandwidth pulse applies energy on both halves of the water pool at the same time, which removes broad asymmetric effects that result from MT.

We chose to analyse exchange rate methods without an asymmetric water pool. In this case there is no benefit to using the multi-bandwidth pulse approach of ZAPI, therefore we elected to use single bandwidth pulses to generate CEST spectra.

### **1.5. Estimating Chemical Exchange Rates from CEST Spectra**

A variety of methods have been developed to estimate chemical exchange rates from CEST spectra. The amplitude of the steady state CEST effect can be measured as a function of saturation power, which can be analyzed using the non-linear QUantifying

Exchange using Saturation Power (QUESP) method (42), or the linear Omega Plot method (43). Because the Omega Plot method is a linear fitting method, the least squares fit is instantaneous, unique, and less prone to error in parameter estimation due to over-fitting, in contrast to the multiple iterations needed to fit the non-linear QUESP model that is plagued with multiple local minima during the fitting process.

The CEST effect can also be measured as a function of saturation time, which can be evaluated using the non-linear QUantifying Exchange using Saturation Time (QUEST) method (42). This analysis method requires the use of moderate to high saturation power, because the fit is not sensitive to the degree of steady state saturation and instead it is instead sensitive to the rate at which steady state saturation is achieved. The QUESTRA method (41) is a variation of the QUEST experiment that uses only two saturation times. This variation removes off resonance saturation of water by obtaining a ratio of the magnetization transfer ratio at two different times.

The Bloch fitting method (44,45) examines the CEST response as a function of saturation frequency. The experimental CEST spectrum can be fit to a model curve generated via the Bloch equations modified for chemical exchange. These equations can be fit via non-linear least squares regression to extract parameters such as exchange rate from the chemical system. Since they are derived from Maxwell's equations, they are valid for any saturation preparation pulse sequence and can thus be used with any method as a means to measure exchange rate. However, the large number of parameters that need to be fit compared to other methods results in larger error. Also, the time needed to fit data will be much higher than with other methods because more data is needed to generate tight estimates of each parameter, and a much higher dimensional space must be searched for the best parameter fit. This is the "gold standard" because no approximations are made in the derivation of the equations. We used the Bloch equations as comparison for the efficacy of exchange rate fitting methods in this thesis.

#### **1.6. Using the Chemical Exchange Rate as a Quantitative Imaging Biomarker**

CEST MRI contrast agents have been designed that can detect enzyme activities. (46) The CEST agent serves as a substrate for an enzyme, and undergoes a covalent bond breaking or bond formation. (47,48) This change in covalent structure can convert an amide group to an amine, or vice-versa. Similarly, a nitric oxide metabolite has been

shown to cause changes in the covalent structure of a CEST agent, which causes a change in the amide and amine functional groups (49). This change in chemical functional group causes a change in chemical exchange rate from the agent. Therefore, measuring the chemical exchange rate of the CEST agent can be used to detect enzyme activities and metabolite biomarkers.

CEST MRI contrast agents have also been developed that detect ions (50). PARACEST agents have been particularly exploited for this application, because the chemistry of chelating a paramagnetic ion of the agent can be leveraged to also chelate an additional ion that is being targeted. The chelation of the targeted ion can cause an electronic redistribution within the structure of the PARACEST agent, which affects the chemical exchange rate of a labile proton on the agent. Therefore, measuring the chemical exchange rate of the PARACEST agent can be used to detect ion biomarkers.

The chemical exchange of a proton between water and the amide and amine groups is base-catalyzed. Therefore, a variety of PARACEST and DIACEST agents have been developed that have chemical exchange rates that are dependent on pH (51-53). A  $\log_{10}$  ratio of two pH-dependent CEST effects from a single agent has been shown to be linearly correlated with the  $\log_{10}$  ratio of hydroxide ion concentration (pOH), which is directly related to pH. However, the detection of two CEST effects from a single agent is inherently more difficult than the detection of a single CEST effect. The measurement of the chemical exchange rate of a pH-dependent CEST agent has great potential to improve the assessment of pH as a biomarker for many pathologies.

The chemical exchange rate of a proton between a CEST agent and water is inherently dependent on temperature as described by the Arrhenius Equation. Chemical exchange rates can also depend on redox state, and may also depend on other environmental conditions in tissues. Therefore, the measurement of a chemical exchange rate of a CEST agent may be exploited to measure these environmental biomarkers.

Knowing the chemical exchange rate of a CEST agent provides the ability to select the most appropriate CEST MRI acquisition and processing method for detecting and quantifying the agent. For example, CEST agents with protons undergoing fast chemical exchange have an effective  $T_2^*$  relaxation rate that precludes the typical pulse-acquire sequences as the signal will decay before signal can be acquired. These CEST agents require SWIFT-CEST MRI acquisition methods (24). Knowledge of the chemical exchange

rates can also facilitate the optimization of common CEST MRI acquisition methods. For example, the optimal saturation power of a common off-resonance CEST MRI protocol is directly related to the chemical exchange rate of the agent. (12) Knowledge of the CEST exchange rates also provides insight into the minimum magnetic field strength that is required for CEST MRI of the agent. In particular, the chemical exchange rate of the agent must be lower than the chemical shift of the agent in units of Hertz, which is linearly dependent on the magnetic field strength. (54) The consideration for magnetic field strength is especially important for clinical studies of CEST agents, because clinical MRI field strengths are currently limited to 3T.

### **1.7. Conclusions**

MRI is an outstanding biomedical imaging method for assessing pathologies and biological processes. CEST MRI provides a new methodology for generating MR image contrast. A variety of analysis methods and acquisition schemes have been developed for detecting and quantifying CEST. Some of these methods are appropriate for quantifying the chemical exchange rate of a CEST agent. The quantification of exchange rates can be used to directly assess a variety of biomarkers such as enzyme activities, metabolites, ions, pH and other environmental biomarkers.

Chapters 2 and 3 provide a detailed analysis of CEST acquisition and analysis method that can accurately and precisely quantify chemical exchange rates of CEST agents.

## CHAPTER 2

THE HANES-WOOLF LINEAR QUESTP METHOD  
IMPROVES THE MEASUREMENTS OF  
FAST CHEMICAL EXCHANGE RATES  
WITH CEST MRI

## PUBLICATIONS

Edward A. Randtke, Liu Qi Chen, L. Rene Corrales, Mark D. Pagel. The Hanes-Woolf linear QUESTP method improves the measurements of fast chemical exchange rates with CEST MRI. *Magn. Reson. Med.* 2013, *In press, Epub ahead of print.*  
DOI:10.1002/mrm.24792

## POSTER PRESENTATION

Edward A. Randtke, Liu Qi Chen, L. Rene Corrales, and Marty Pagel. The Hanes-Woolf Linear QUEST Method Provides the Most Accurate Determination of Fast Chemical

## 2.1. Abstract

Contrast agents for Chemical Exchange Saturation Transfer (CEST) MRI often require an accurate measurement of the chemical exchange rate. Many analysis methods have been reported that measure chemical exchange rates. Additional analysis methods were derived as part of this study. This report investigated the accuracy and precision of each analysis method. CEST spectra were simulated using the Bloch-McConnell equations modified for chemical exchange. CEST spectra of iopromide were obtained with a range of saturation times, saturation powers, and concentrations. These simulated and experimental results were used to estimate the chemical exchange rate using the QUESP, QUEST, Omega Plot (LB-QUESP), EH-QUESP, HW-QUESP, LB-Conc, EH-Conc, and HW-Conc methods. Bloch fitting produced the most precise estimates of chemical exchange rates, although substantial expertise and computation time are required to achieve these results. Of the more simplistic analysis methods, the HW-QUESP method produced the most accurate and precise estimates of fast exchange rates. The QUEST and LB-QUESP methods produced the most accurate estimates of slow exchange rates, especially with samples that have short  $T_{1w}$  relaxation times.

## 2.2. Introduction

Exogenous Chemical Exchange Saturation Transfer (CEST) MRI contrast agents have been developed that measure or detect a variety of molecular biomarkers (1). A typical CEST MRI study uses selective radio frequency saturation at the chemical shift of a labile proton of the agent (relative to the chemical shift of water that is defined to be 0 ppm), which eliminates the coherent MR signal from the proton. Subsequent chemical exchange of the proton from the agent to a water molecule transfers the saturation to the water resonance and decreases the net water signal. Most studies of CEST agents typically acquire CEST spectra, which records the relative water signal after selective saturation over a range of MR frequencies (Fig. 2.1) (2).

The development and characterization of exogenous CEST agents can require an accurate determination of the chemical exchange rate. For example, accurate measurements of chemical exchange rates can be used to quantify molecular biomarkers

such as pH (2,3). Chemical exchange rates can also facilitate the measurement of CEST agent concentration, which can be useful for evaluating other biomarkers (4). Measurements of chemical exchange rates can be used to select the best saturation power and the best CEST MRI acquisition method for detecting the CEST agent (5-7).

To meet this need, a variety of analysis methods have been developed that can determine chemical exchange rates from CEST MRI results. The Bloch-McConnell equations that are modified to include chemical exchange can be fit to a CEST spectrum to determine the exchange rate (a.k.a., the Bloch fitting method) (8). The QUEST and QUESP methods measure the CEST effect as a function of saturation time or saturation power, respectively, which can then be fit by nonlinear functions that determine the exchange rate (9). The Omega Plot method is a linear version of the QUESP method that can determine the exchange rate using a facile linear fitting method (10). CEST is also dependent on concentration, and a nonlinear function and linear variations of these functions can be used to determine exchange rates (11). Most of these methods make assumptions to simplify the analysis. Each method has different dependencies on experimental parameters and different weightings of the experimental results.

As presented in this report, we have developed three new analysis methods for determining chemical exchange rates. We have developed QUESPT that measures the CEST effect as a function of saturation time and saturation power, and analyzes this combination of all CEST measurements to estimate the chemical exchange rate. We have also developed two new linear analysis methods that are similar to the Omega Plot method. As with the other established analysis methods, these new methods make assumptions to simplify the analysis, and have different dependencies on experimental parameters and weightings of experimental results.

The effect of exchange rate on saturation transfer is often underappreciated when using CEST MRI methods (3,9,12,13). Slowly exchanging protons on the CEST agent experience the full effect of the saturation applied at the unique chemical shift of the proton on the agent. However, rapidly exchanging protons spend a fraction of time on the agent compared to slowly exchanging protons, and, therefore, experience a fraction of the effect of the saturation applied at the chemical shift of the agent. This incomplete saturation can become significant for protons that exchange as slow as 20% of the chemical shift of the agent's exchangeable proton (9). CEST MRI methods that rely on complete saturation

(e.g., QUEST) or an accurate determination of the level of saturation (e.g., QUESP, Omega Plot) may inaccurately measure fast chemical exchange rates. This effect is an important consideration for diamagnetic CEST agents that typically have MR chemical shifts less than 6 ppm (14). Paramagnetic CEST agents can have greater chemical shifts, so that chemical groups with faster exchange rates can generate CEST (15). Yet incomplete saturation may still be an important consideration for paramagnetic CEST agents that have small chemical shifts or very rapid exchange rates.

We sought to evaluate the accuracy and precision of methods that analyze CEST MRI results to measure chemical exchange rates. We simulated CEST spectra using the Bloch-McConnell equations modified for chemical exchange, and then evaluated the accuracy of estimating chemical exchange rates with each analysis method. We then experimentally measured the CEST spectra of iopromide (Ultravist™, Bayer Health Care, Inc., Tarrytown, NY) that has amide protons with slow and fast exchange rates, and estimated the chemical exchange rates of this agent using each analysis method. This report describes our evaluations and provides recommendations for selecting the best analysis methods for analyzing slow and fast chemical exchange rates.

### 2.3. Theory

Assuming that a CEST agent instantaneously reaches steady-state saturation (but does not necessarily reach complete saturation), a previous report has shown that CEST can be described as a function of saturation time ( $t_{sat}$ ) and saturation power ( $\omega_1$ ) (Eq. [2.1]) (9).

$$\frac{M_0 - M_S}{M_0} = \frac{\alpha k_{ex} \chi}{R_{1w} + k_{ex} \chi} [1 - e^{-(R_{1w} + k_{ex} \chi) t_{sat}}] \quad [2.1]$$

where:

$$\chi = \frac{n_{CA} [CA]}{n_{H_2O} [H_2O]} \quad [2.2]$$

$$\alpha = \frac{\omega_1^2}{\omega_1^2 + R_1 R_2} \quad [2.3]$$

$$R_{1,2} = R_{1A,2A} + k_{ex} - \frac{k_{ex}^2 \chi}{R_{1w,2w} + k_{ex} \chi} \quad [2.4]$$

$k_{ex}$ : chemical exchange rate

$M_S, M_0$ : water signal with saturation (S) and without saturation (0)

[CA], [H<sub>2</sub>O]: concentration of the contrast agent and water

$n_{CA}, n_{H_2O}$ : number of magnetically equivalent exchangeable protons on the agent and water

$R_{1A}, R_{2A}, R_{1w}, R_{2w}$ :  $R_1$  and  $R_2$  relaxation rates of the agent and water

The QUEST method fits the exponential term of Eq. [2.1] to CEST measurements determined with a range of saturation times, while the ratiometric term of Eq. [2.1] is a scalar term during the fitting. QUESP fits Eq. [2.3] to CEST measurements determined with a range of saturation powers, while the exponential term of Eq. [2.1] is a scalar term during the fitting. Alternatively, QUEPT fits the ratiometric term and the exponential term of Eq. [2.3] to CEST measurements determined with ranges of saturation times and powers.

If the relaxation rates of the agent are slow ( $R_{1A,2A} \ll k_{ex}$ ), and saturation has reached steady state ( $t_{sat}$  is very long), then Eq. [2.1] can be reduced to Eq. [2.5] (note that  $R_{1w,2w}k_{ex} \gg 0$  so that the second term in Eq. [2.4] is always much greater than the third term). As previously shown, CEST can be described as a function of relative concentration,  $R_{1w}$ , and chemical exchange rate under these same conditions (Eq. [2.6]) (15). If the concentration of the agent is not low ( $\chi \gg R_{1w}/k_{ex}$ ), then Eq. [2.6] may be approximated (Eq. [2.7]), combined with Eq. [2.5] (Eq. [8]), and rearranged to create a linear relationship (Eq. [2.9]) (10). The x-intercept of this equation is equal to  $-1/k_{ex}^2$ , which provides a relatively simplistic method for determining the chemical exchange rate relative to fitting the non-linear Eq. [2.1] to experimental results.

$$\frac{M_0 - M_S}{M_0} = \alpha = \frac{\omega_1^2}{\omega_1^2 + k_{ex}^2} \quad [2.5]$$

$$\frac{M_S}{M_0} = \frac{1}{1 + \frac{\chi k_{ex}}{R_1}} \quad [2.6]$$

$$\frac{M_S}{M_0} \approx \frac{R_1}{\chi k_{ex}} \quad [2.7]$$

$$\frac{M_0 - M_S}{M_0} = \frac{\omega_1^2}{\omega_1^2 + k_{ex}^2} \left[ \frac{M_S}{M_0} \frac{\chi k_{ex}}{R_1} \right] \quad [2.8]$$

$$\frac{M_S}{M_0-M_S} = \frac{R_1 k_{ex}}{\chi} \left( \frac{1}{k_{ex}^2} + \frac{1}{\omega_1^2} \right) \quad \left( \text{a linear equation if } x = \frac{1}{\omega_1^2} \text{ and } y = \frac{M_S}{M_0-M_S} \right) \quad [2.9]$$

Eq. [2.9] is known as the “Omega Plot” method, which is analogous to the linear Lineweaver-Burk plot that is used to assess Michaelis-Menten chemical kinetics (16). We refer to the Omega Plot method as the “LB-QUESP” method. Michaelis-Menten kinetics can also be analyzed using a linear Eadie-Hoffsee plot and a Hanes-Woolf plot that are rearrangements of the Lineweaver-Burk plot (17,18). Similarly, the LB-QUESP method can be rearranged to form the “EH-QUESP” and “HW-QUESP” plotting methods (Eqs. [2.10] and [2.11]). The chemical exchange rate can be determined from the slope of the EH-QUESP equation, and from the ratio of the y-intercept and slope of the HW-QUESP equation. This derivation shows that these linear variations of QUESP are only valid with intermediate concentrations of the CEST agent ( $R_{1w}/k_{ex} \ll \chi \ll 1$ ).

$$\frac{M_0-M_S}{M_S} = \frac{\chi k_{ex}}{R_1} - k_{ex}^2 \frac{M_0-M_S}{M_S \omega_1^2} \quad \left( \text{a linear equation if } x = \frac{M_0-M_S}{M_S \omega_1^2} \text{ and } y = \frac{M_0-M_S}{M_S} \right) \quad [2.10]$$

$$\frac{\omega_1^2 M_S}{M_0-M_S} = \frac{\omega_1^2 R_1}{\chi k_{ex}} + \frac{R_1 k_{ex}}{\chi} \quad \left( \text{a linear equation if } x = \omega_1^2 \text{ and } y = \frac{\omega_1^2 M_S}{M_0-M_S} \right) \quad [2.11]$$

The derivations of concentration-dependent analysis methods that estimate chemical exchange rates have been previously reported (Eqs. [2.12]-[2.14]) (11). We refer to these methods as LB-Conc, EH-Conc, and HW-Conc, because they are analogous to Lineweaver-Burk, Eadie-Hoffstee, and Hanes-Woolf plots. The chemical exchange rate can be determined from the ratio of the slope and intercept of the LB-Conc equation or the HW-Conc equation, or from the slope of the EH-Conc equation, if the  $r_1$ relaxivity of the agent is known.

$$\frac{1}{[CA]} = \left( \frac{1}{\frac{M_0}{M_S}-1} \right) \left( \frac{n_{CA} T_{1w} k_{ex}}{n_{H_2O} H_2O} \right) - r_1 T_{1W} \quad \left( \text{a linear equation if } x = \frac{1}{\frac{M_0}{M_S}-1} \text{ and } y = \frac{1}{[CA]} \right) \quad [2.12]$$

$$[CA] = \left( \frac{[CA]}{\frac{M_0}{M_S}-1} \right) \left( \frac{n_{CA} k_{ex}}{n_{H_2O} H_2O r_1} \right) - \frac{1}{r_1 T_{1W}} \quad \left( \text{a linear equation if } x = \frac{[CA]}{\frac{M_0}{M_S}-1} \text{ and } y = [CA] \right) \quad [2.13]$$

$$\frac{\frac{M_0}{M_S}-1}{[CA]} = \left( \frac{n_{CA} T_{1w} k_{ex}}{n_{H_2O} H_2O} \right) - r_1 T_{1W} \left( \frac{M_0}{M_S} - 1 \right) \quad \left( \text{a linear equation if } x = \frac{M_0}{M_S} - 1 \text{ and } y = \frac{\frac{M_0}{M_S}-1}{[CA]} \right) \quad [2.14]$$

## 2.4. Methods

### 2.4.1. Simulations

The Bloch equations were used to generate CEST spectra of iopromide. All simulations used chemical shifts of 5.6 ppm and 4.2 ppm for each amide resonance, 0.0 ppm for the water resonance, and 0.87 ppm for the hydroxyl group resonance that was set to an exchange rate of 400 Hz. Each simulation tested exchange rates from 0 to 1200 Hz and  $T_1$  relaxation times from 0.1 to 10 s. One set of simulations tested saturation times of 0.25-10 s with a saturation power of 4  $\mu$ T and a concentration of 200 mM. Another set of simulations tested saturation powers of 0.5 to 10  $\mu$ T with a saturation time of 6 s and a concentration of 200 mM. Yet another set of simulations were tested with concentrations of 10-2500 mM, a saturation time of 6 s and a saturation power of 5  $\mu$ T. A finite continuous-wave saturation pulse and an infinite series of pulses that represent steady-state conditions were each used for the simulations. The simulated results were identical for both types of saturation pulse periods, which agreed with results from previous reports (19,20). Therefore, the results from the finite saturation pulse were used for subsequent analyses, because the experimental study used this type of saturation pulse. Lorentzian line shape fitting was used to measure the CEST effect ( $M_s$ ) for each amide from each simulated spectrum as previously described, using spectra normalized from 0% to 100% water signal (which set  $M_0$  equal to 100%) (21). The fittings were performed with MATLAB v2011a (Mathworks, Inc., Natick, MA) using the “trust-region-reflective” algorithm to reach a convergence criterion of  $10^{-16}$ .

The QUEST, QUESP, and QUESPT methods were fit to simulated results to estimate the chemical exchange rate of the amide at 5.6 ppm. Fittings were either performed by setting  $R_{1w}$  to the inverse of the  $T_{1w}$  value used to simulate the spectrum, or were performed by allowing  $R_{1w}$  to be a fitted parameter.  $R_{2w}$  was set to  $R_{1w}$  for all of these fittings. The LB-QUESP, EH-QUESP, HW-QUESP, LB-Conc, EH-Conc, and HW-Conc methods were also used to estimate chemical exchange rates from the simulated CEST results. LB-QUESP was fit to results simulated with saturation times less than or equal to 7  $\mu$ T, and the other methods were fit to results simulated with all saturation times. All non-linear and linear fittings were performed with Matlab v2011a using the “trust-region-reflective” algorithm to reach a convergence criterion of  $10^{-16}$ . All linear fittings were performed with MATLAB v2011a using an “ordinary least squares” algorithm.

### 2.4.2. Experimental Studies

Iopromide was diluted with phosphate-buffered saline to concentrations of 270, 178, 135, 90, 45, and 22.5 mM, and were adjusted to 6.47 pH units with concentrated sodium hydroxide. All CEST experiments were performed using a 600 MHz Varian Inova NMR spectrometer with an inverse cryoprobe. Samples were analyzed at 37.3°C. The temperature was calibrated by measuring the separation of resonances of neat methanol and ethylene glycol samples between 25°C and 40°C (20). The probe was manually tuned to each sample, and the 90° pulse time was measured to initially estimate the saturation power. The exact saturation power was obtained from the Bloch fitting. CEST spectra were acquired with a continuous-wave saturation pulse and saturation frequencies set at 10 to -10 ppm in 0.2 ppm increments, and each scan was averaged four times. For the first set of studies, saturation times ranging between 0.5 and 6 s were tested with a relaxation delay from 5.5 to 0 s to maintain a total time of 6 s for the pre-acquisition period. These studies were conducted with a saturation power of 5.2 and 13.14  $\mu\text{T}$  and a sample with a concentration of 178 mM. For the second set of studies, saturation powers ranging between 0.325 and 7.618  $\mu\text{T}$  were tested with a saturation time of 6s and with no additional relaxation delay, with a sample with a concentration of 178 mM. For the third set of studies, samples with a series of concentrations were tested with saturation time of 6 s and saturation power of approximately 3.2  $\mu\text{T}$ .

The Bloch-McConnell equations modified for chemical exchange were fit to each experimental CEST spectrum (Eq. [2.12]) (8,23). The integrating factor method was used to solve the Bloch equations. The “lsqcurvefit” routine with the trust-region-reflective algorithm was used to initially fit the CEST spectra, which resulted in rough parameter estimates. The “nlinfit” routine with the “Levenburg-Marquardt” algorithm was then used to fit the CEST spectra to obtain the final parameter estimates. The Jacobian from the nlinfit routine was used to determine confidence intervals for fitted parameters.

Other CEST studies with MRI scanners have accounted for  $B_0$  and  $B_1$  inhomogeneities (23,24). To account for  $B_0$  and  $B_1$  inhomogeneities in our studies, each point of an experimental CEST spectrum was assumed to represent a gaussian-shaped point spread function, which was modeled during the fitting process. However, the fitting results with and without the point spread function were identical, indicating that accounting for  $B_0$  and  $B_1$  inhomogeneities was unnecessary with data generated from our NMR spectrometer. Subsequent analyses were conducted without incorporating the point spread function. The

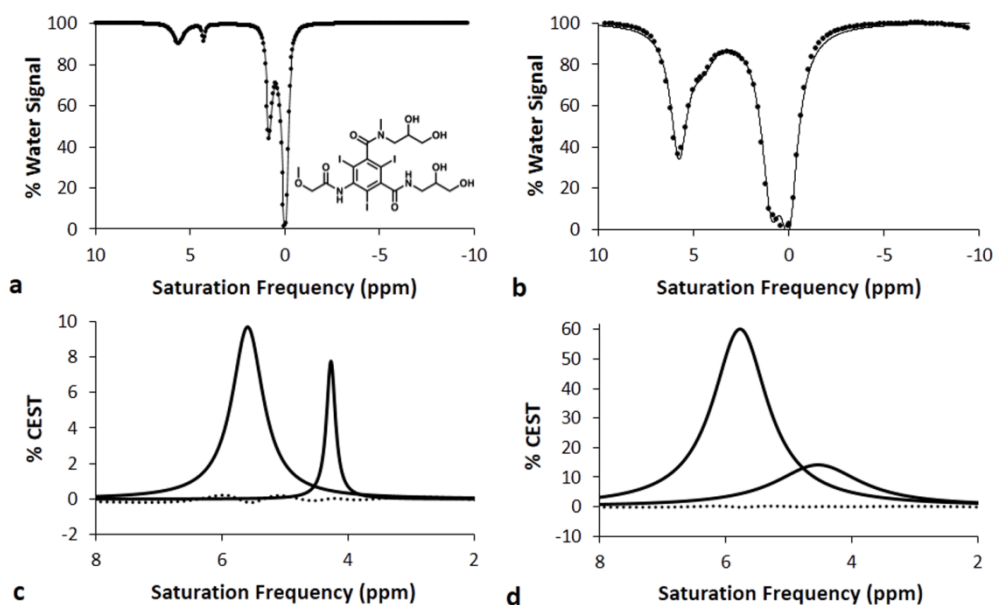


Figure 2.1: Lorentzian fitting

Representative Lorentzian line shapes fitted to simulated CEST spectra of iopromide at a) 1  $\mu\text{T}$  saturation power and b) 5  $\mu\text{T}$  saturation power, with a 1 s saturation time and 1000 Hz chemical exchange rate, 200 mM concentration, and a 3 s  $T_{1w}$  relaxation time. The chemical structure of iopromide is shown in the inset. The CEST effect at 5.6 ppm arises from the amide proton between the ring and carbonyl group, while the CEST effect at 4.2 ppm arises from the amide proton between the diol group and the carbonyl group. The CEST effect at 0.8 ppm arises from the diol groups, and the direct saturation of water is shown as a line shape at 0 ppm. Lorentzian line shape spectra generated from the fitting process show the CEST effects from the amides at c) 1  $\mu\text{T}$  saturation power and d) 5  $\mu\text{T}$  saturation power. The residuals of the fitting processes are shown as a dotted line.

fitting process estimated values for the  $T_{1w}$ ,  $T_{2w}$ ,  $T_{1A}$ , and  $T_{2A}$  relaxation times of the amide protons of the agent. As previously reported, these fitted estimates of the CEST agent's relaxation times are inconsequential to the fitting process (8). Furthermore, to validate the fitting method, fitted parameters were estimated using all but one experimental CEST spectrum, then the remaining experimental spectrum was compared to a simulated spectrum using the fitted parameters. In all cases, the remaining experimental spectrum and simulated spectrum showed an outstanding match.

Lorentzian line shape fitting was used to measure the CEST effect ( $M_S$ ) for each amide from each experimental spectrum as previously described, using spectra normalized from 0% to 100% water signal (which set  $M_0$  equal to 100%) (19). The fittings were performed with Matlab v2011a using the trust-region-reflective algorithm to reach a convergence criterion of  $10^{-16}$ . The QUEST, QUESP, QUESPT, LB-QUESP, EH-QUESP, HW-QUESP,

LB-Conc, EH-Conc, and HW-Conc methods were used to estimate  $k_{ex}$  rates from these CEST measurements determined from the Lorentzian line shape fittings.

## 2.5. Results

### 2.5.1. Simulations

The Bloch equations were used to generate CEST spectra of iopromide using a range of chemical exchange rates, saturation times, saturation powers, and concentrations (Fig.

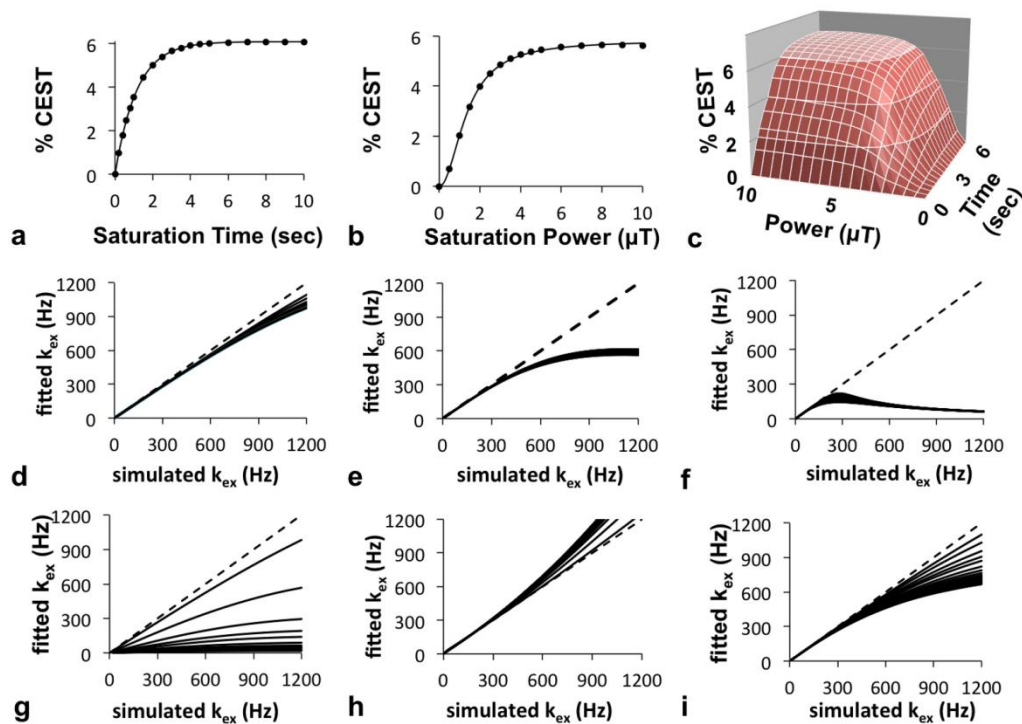


Figure 2.2: QUEST, QUESP and QUESPT simulation

QUEST, QUESP, and QUESPT analyses of simulated CEST MRI results. a) A representative QUEST fitting of simulated results generated with 10  $\mu\text{T}$  saturation power, 25 Hz chemical exchange rate, and 1.5 s  $T_{1w}$  relaxation time. b) A representative QUESP fitting with simulated results generated with 10 s saturation time, 350 Hz chemical exchange rate, and 0.1 s  $T_{1w}$  relaxation time. c) A representative QUESPT fitting with simulated results generated with a 25 Hz chemical exchange rate and 1.5 s  $T_{1w}$  relaxation time. The exchange rates estimated with QUEST at d) 10  $\mu\text{T}$ , e) 4  $\mu\text{T}$ , and f) 1  $\mu\text{T}$  saturation power at short (\*) and long (●)  $T_{1w}$  relaxation times showed that QUEST accurately estimated slow  $k_{ex}$  rates, but required high saturation power to accurately estimate fast  $k_{ex}$ , with a minor dependence on  $T_{1w}$  relaxation times. The exchange rates estimated with QUESP g) with fixed  $T_{1w}$  and  $T_{2w}$  relaxation times ranging from short (\*) to long (●) estimated fast  $k_{ex}$  with poor accuracy, h) while allowing  $T_{1w}$  and  $T_{2w}$  to be fitted improved the accuracy of estimating fast  $k_{ex}$ . i) The estimations of exchange rates with QUESPT showed a result that was intermediate between the results from QUEST and QUESP methods. For graphs d-i, a dashed line with slope=1 is shown to aid visualization of the results.

2.1A, 2.1B). Each CEST spectrum was fit with a function of four Lorentzian line shapes to measure the CEST effects of both amide protons (Fig. 2.1C, 2.1D). The Lorentzian line shapes did not exactly match the CEST spectra as shown by non-zero fitting residuals. However, the residuals at the maximum CEST effect simulated with low and high saturation powers were 2.0% and 0.33% of the CEST measurement, respectively, which demonstrated that the Lorentzian line fitting could measure CEST with high accuracy. Additional fitting iterations to meet tighter convergence criteria did not improve the accuracy of this result, which demonstrated that this small inaccuracy is an inherent difference between Lorentzian line shapes and CEST spectra. The CEST effect at 4.2 ppm was more difficult to fit with a Lorentzian line shape than the CEST effect at 5.6 ppm, presumably because the peak at 4.2 ppm was a “shoulder peak” on the larger peak at 5.6 ppm.

The CEST measurements were used to estimate exchange rates using QUEST, QUESP and QUESPT (Fig. 2.2A-C). The QUEST method fit the simulated results throughout the entire range of saturation times. The QUESP method showed an excellent fitting to the simulated results obtained with low and moderate saturation powers, but showed a small deviation when fitting to simulated results obtained with high saturation power. The QUESPT method showed similar results, with exact fitting to simulated results along the entire time dimension, and a small deviation relative to simulated results with high saturation power. This result demonstrated that QUESPT is a mixture of QUEST and QUESP, and does not necessarily improve analytical accuracy relative to QUEST.

The QUEST method estimated  $k_{\text{ex}}$  rates with excellent accuracy, although the accuracy decreased at higher  $k_{\text{ex}}$  rates (Fig. 2.2D), which agreed with a previous report (9). This decreased accuracy at faster  $k_{\text{ex}}$  was amplified as the saturation power was decreased (Fig. 2.2D-F). The accuracy of estimating  $k_{\text{ex}}$  with QUEST increased with shorter simulated  $T_{1w}$  relaxation times, although this dependence was minor throughout the range of exchange rates that were tested. Therefore, these results demonstrated that QUEST could measure slow exchange rates with excellent accuracy as long as the saturation power is high.

The QUESP method also estimated  $k_{\text{ex}}$  with decreasing accuracy at faster  $k_{\text{ex}}$  rates, which also agreed with a previous report (Fig. 2.2G) (9). QUESP was more severely dependent on this effect of  $T_{1w}$  time, showing extreme inaccuracies when  $T_{1w}$  times were greater than

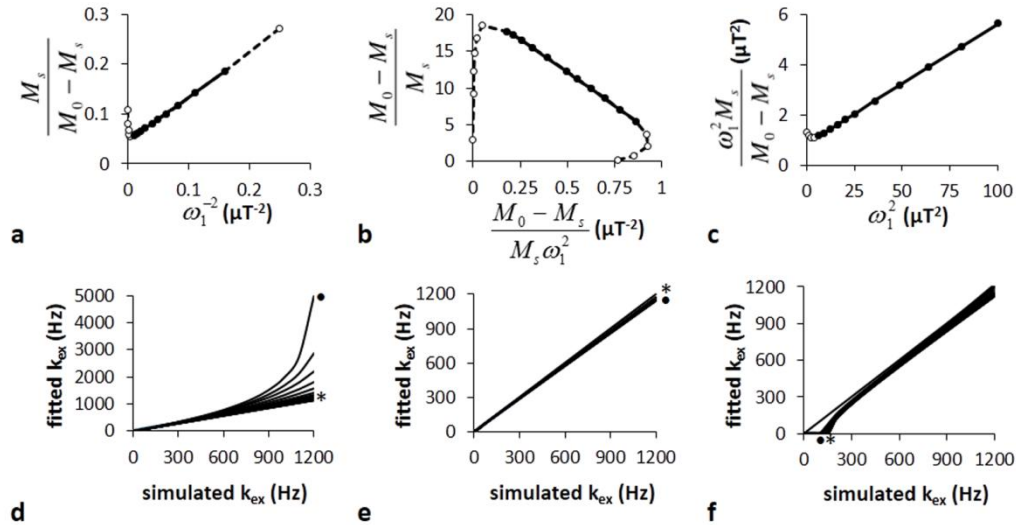


Figure 2.3: Linear QUESP simulation

LB-QUESP, EH-QUESP and HW-QUESP analyses of simulated CEST MRI results generated with a 10 s saturation time, 1200 Hz chemical exchange rate, and 10 s  $T_{1w}$  relaxation time. A representative a) LB-QUESP, b) EH-QUESP, and c) HW-QUESP fitting of simulated CEST results were used to estimate  $k_{ex}$ . d) The exchange rates estimated with LB-QUESP at short (\*) and long (•)  $T_{1w}$  relaxation times accurately estimated slow exchange rates, but failed to accurately estimate fast exchange rates. e) EH-QUESP accurately estimated slow and fast exchange rates, and f) HW-QUESP accurately estimated fast exchange rates, with little dependence on  $T_{1w}$  relaxation times.

0.1 sec. To investigate this dependence on  $T_{1w}$  time, the QUESP method was modified to fit the  $T_{1w}$  time in addition to fitting  $k_{ex}$  (Fig. 2.2H). The  $T_{2w}$  time was set to the variable  $T_{1w}$  time during this fitting process. These results showed that this approach overestimated the  $k_{ex}$  rate, yet produced a more accurate estimate than when  $T_{1w}$  and  $T_{2w}$  were fixed. The estimated  $T_{1w}$  and  $T_{2w}$  times were fit to values that were 1/3 to 1/2 of the values used to create the simulated CEST spectra. This result demonstrated that fitting QUESP to CEST results is more sensitive to the value of  $k_{ex}$  than values of  $T_{1w}$  and  $T_{2w}$  times. For comparison, the QUEST method was modified in the same way to fit  $T_{1w}$  and  $T_{2w}$  times in addition to fitting the  $k_{ex}$  rate. The results were the same as fittings with fixed  $T_{1w}$  and  $T_{2w}$  times (data not shown), and the estimated  $T_{1w}$  and  $T_{2w}$  times were not significantly different from the values used to create the simulated CEST spectra.

The QUESPT method estimated  $k_{ex}$  with decreasing accuracy at faster  $k_{ex}$  (Fig. 2.2I). The dependence on  $T_{1w}$  and  $T_{2w}$  times was intermediate between the dependencies shown with QUEST and QUESP. This result confirmed that QUESPT is a mixture of QUEST and QUESP that does not improve the accuracy of estimating  $k_{ex}$  relative to QUEST.

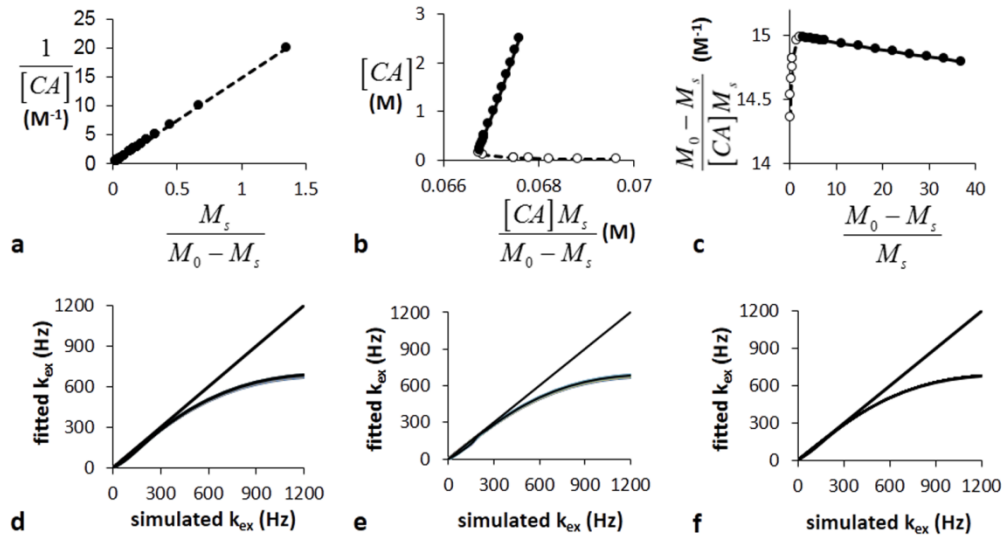


Figure 2.4: Linear concentration simulation

LB-Conc, EH-Conc, and HW-Conc analyses of simulated CEST MRI results generated with a 3.5  $\mu\text{T}$  saturation power, 10 s saturation time, 1200 Hz chemical exchange rate, and 10 s  $T_{1w}$  relaxation time. A representative a) LB-Conc, b) EH-Conc, and c) HW-Conc fitting of simulated CEST results were used to estimate  $k_{ex}$ . d) LB-QUESP, e) EH-QUESP, and f) HW-QUESP accurately estimated slow  $k_{ex}$ , but failed to accurately estimate fast  $k_{ex}$ . The  $T_{1w}$  relaxation time did not affect the accuracies of these estimates.

The CEST measurements were also used to estimate exchange rates using the LB-QUESP, EH-QUESP, and HW-QUESP methods (Fig. 2.3A-C). LB-QUESP and EH-QUESP showed a deviation from linearity at high saturation powers, because the derivation of these equations assumes that the chemical shift difference between the agent and water is much larger than the saturation power (10). HW-QUESP did not suffer from non-linearity at high saturation powers. Each method showed a deviation from linearity at low saturation powers, presumably because very low powers cannot generate instantaneous saturation as assumed in the derivation of the equations. These deviations at high and low saturation powers were more pronounced for simulations performed with long  $T_{1w}$  times (data not shown). Yet each method had a range of saturation powers that produces a linear relationship that can be used to estimate  $k_{ex}$  rates with high accuracy.

The LB-QUESP method estimated  $k_{ex}$  with excellent accuracy, although the accuracy decreased at faster  $k_{ex}$  rates (Fig. 2.3D). As with QUESP, longer  $T_{1w}$  times decreased the accuracy of estimating  $k_{ex}$  with this method. For comparison, EH-QUESP estimated  $k_{ex}$  with excellent accuracy and with little dependence on  $T_{1w}$  times (Fig. 2.3E). HW-QUESP also estimated  $k_{ex}$  rates with excellent accuracy with negligible dependence on  $T_{1w}$  times,

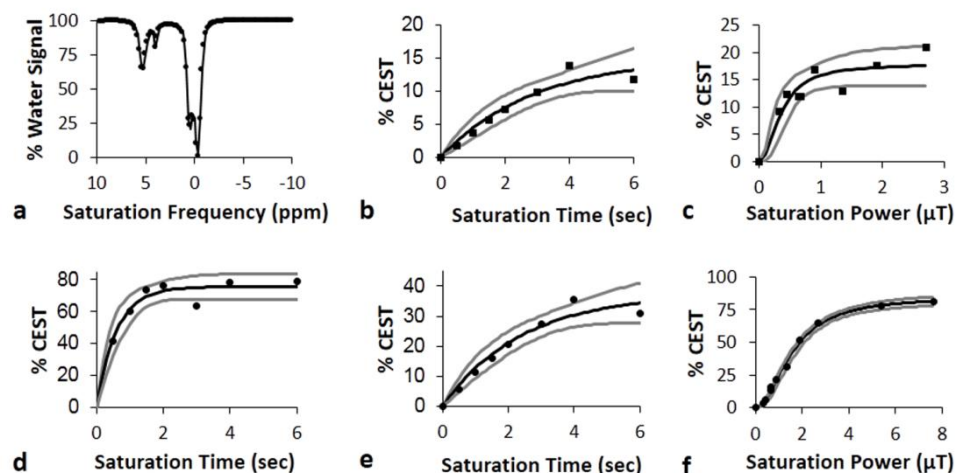


Figure 2.5: Nonlinear fitting of experimental data

Bloch fitting, QUEST, and QUESP analyses of 178 mM of iopromide. a) Bloch fitting of a representative CEST spectrum of iopromide acquired with 1.26  $\mu\text{T}$  saturation power was used to estimate  $k_{\text{ex}}$ . b) QUEST with saturation power of 5.2  $\mu\text{T}$  and c) QUESP with saturation time of 6 s were used to analyze CEST at 4.2 ppm to estimate the exchange rate for the slowly exchanging amide proton. d) QUEST with saturation power of 13.14  $\mu\text{T}$ , e) QUEST with saturation power of 5.2  $\mu\text{T}$ , and f) QUESP with saturation time of 6 s were used to analyze CEST at 5.6 ppm to estimate the exchange rate for the rapidly exchanging amide proton. The boundary estimates are shown as gray lines.

although the accuracy decreased for lower  $k_{\text{ex}}$  (Fig. 2.3F). Therefore, these results indicated that EH-QUESP and HW-QUESP are the most accurate methods for estimating fast exchange rates.

The CEST measurements were also used to estimate  $k_{\text{ex}}$  using the LB-Conc, EH-Conc, and HW-Conc methods (Fig. 2.4A-C). EH-Conc showed deviation from linearity at low concentrations, while HW-Conc showed deviation from linearity at high concentrations. LW-Conc showed linearity throughout the concentration range tested during this study. The linear range of each method was used to estimate  $k_{\text{ex}}$  (Fig. 2.4D-F). Each of these methods estimated  $k_{\text{ex}}$  with excellent accuracy for slow  $k_{\text{ex}}$  rates, and with decreasing accuracies for faster  $k_{\text{ex}}$  rates. These accuracies were independent of  $T_{1w}$  times (Fig. 2.4D-F) and saturation powers (data not shown). These results showed that concentration-based analysis methods fail to accurately measure fast exchange rates.

## 2.5.2. Experimental Results

Experimental CEST spectra of iopromide were obtained using a range of saturation times, saturation powers, and concentrations (Fig. 2.5A). The Bloch equations were

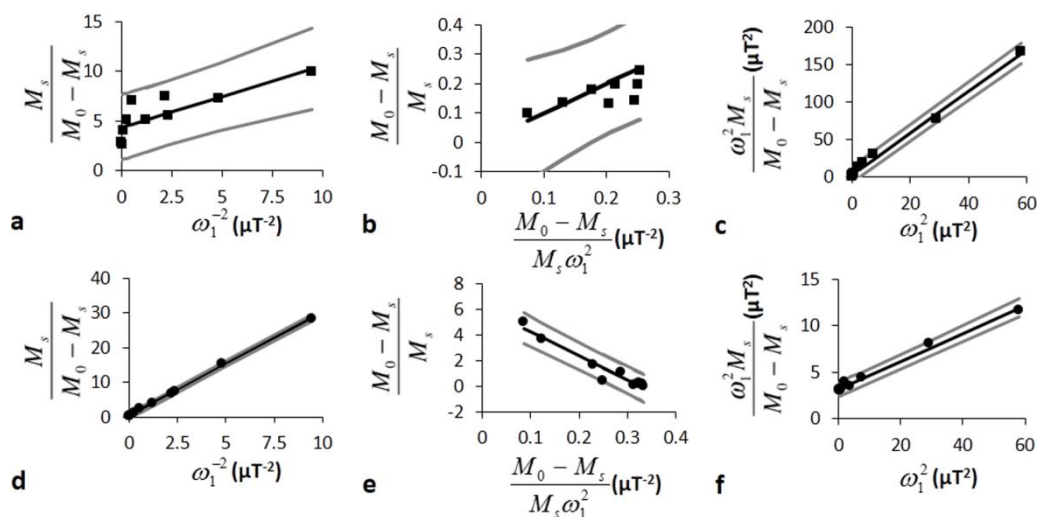


Figure 2.6: Linear QUESP fitting of experimental data

LB-QUESP, EH-QUESP, and HW-QUESP analyses of 178 mM of iopromide with a saturation time of 6 s. a) LB-QUESP, b) EH-QUESP, and c) HW-QUESP analyses of CEST at 4.2 ppm estimated the  $k_{\text{ex}}$  for the slowly exchanging amide proton. d) LB-QUESP, e) EH-QUESP, and f) HW-QUESP analyses of CEST at 5.6 ppm estimated  $k_{\text{ex}}$  for the rapidly exchanging amide proton. The boundary estimates are shown as gray lines.

simultaneously fit to 12 CEST spectra with different saturation times and powers to estimate the chemical exchange rates for both amide protons of iopromide (Table 2.1). The CIs of fitting the twelve CEST spectra were 1.7%, while fitting to a CEST spectrum with 6 s of 1  $\mu\text{T}$  saturation generated CIs of 3.1%, which demonstrated that simultaneously fitting multiple CEST spectra generated greater precision. The  $T_{1w}$  and  $T_{2w}$  times and the saturation powers were also fitted with this method, rather than fixing these parameters during the fitting. The estimated  $T_{1w}$  and  $T_{2w}$  times from the fitting were 3.64 s and 1.54 s, respectively. The saturation powers were determined to be 34.5% greater than the experimental values estimated from the  $90^\circ$  pulse time. This result indicated that radiation damping or amplifier non-linearity affected the estimation of saturation powers from the measured  $90^\circ$  pulse time. The saturation powers that were accurately estimated from Bloch fittings were used for the subsequent analyses. Overall, these results showed that the saturation power and  $T_{1w}$  and  $T_{2w}$  relaxation times do not have to be experimentally determined to estimate chemical exchange rates with the Bloch fitting method.

Each CEST spectrum was also fit with a function of four Lorentzian line shapes to measure the CEST effects of both amide protons. The maximum residuals for the CEST effects at 5.6 and 4.2 ppm were 0.07% CEST and 0.15% CEST respectively when a 4  $\mu\text{T}$  saturation

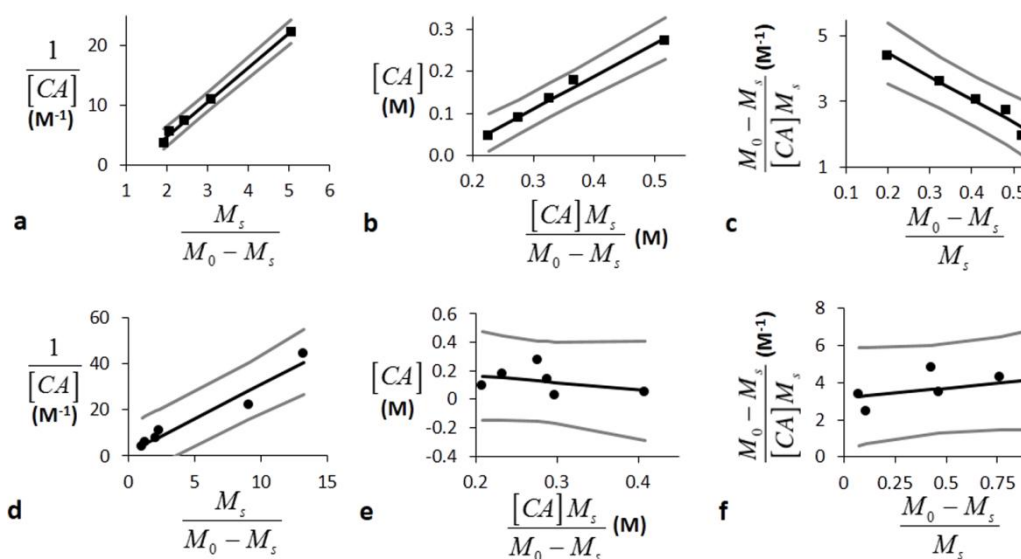


Figure 2.7: Linear concentration fitting of experimental data

LB-Conc, EH-Conc, and HW-Conc analyses of iopromide with 3.2  $\mu T$  saturation power and 6 s saturation time. a) LB-Conc, b) EH-Conc, and c) HW-Conc analyses of CEST at 4.2 ppm estimated  $k_{ex}$  for the slowly exchanging amide proton. d) LB-Conc, e) EH-Conc, and f) HW-Conc analyses of CEST at 5.6 ppm estimated  $k_{ex}$  for the rapidly exchanging amide proton. The boundary estimates are shown as gray lines.

power was used, which demonstrated that the Lorentzian line fitting can measure CEST with high accuracy. A Lorentzian line shape could not be reliably fit to the amide resonance at 4.2 ppm when 10  $\mu T$  saturation power was used due to peak broadening throughout the CEST spectrum.

The QUEST and QUESP methods were used to estimate  $k_{ex}$  of the slowly exchanging amide proton at 4.2 ppm (Fig. 2.5B, 2.5C; Table 2.1). Although both methods estimated  $k_{ex}$  rates that were close to the rates estimated from Bloch fitting, QUEST underestimated this rate and QUESP overestimated this rate, which was consistent with the results from simulations. The estimate of  $k_{ex}$  with QUEST had CIs that were narrower than the CIs for QUESP, which indicated that QUEST could more precisely estimate  $k_{ex}$ .

The  $k_{ex}$  of the rapidly exchanging amide proton estimated with QUEST and QUESP showed substantial differences from the rate determined with Bloch fitting, which was consistent with the results of simulations (Fig. 2.5D, 2.5E; Table 2.1). QUESP overestimated this rate and QUEST underestimated this rate, and lower saturation powers caused a greater underestimation by QUEST, which was also consistent with simulations.

The Estimated Chemical Exchange Rates of iopromide		
Method	4.2 ppm	5.6 ppm
Bloch Fitting	55.9 (53.7 - 58.3)	1117.1 (1100.5 - 1134.0)
QUEST (4 $\mu$ T)	28.9 (17.5 - 47.8)	87.8 (57.6 - 133.9)
QUEST (10 $\mu$ T)	---	694.7 (453.8 - 1063.7)
QUESP	118.0 (65.2 - 213.6)	2826.3 (2059.7 - 3878.2)
LB-QUESP	101.2 (80.2 - 111.3)	922.3 (648.8 - )
EH-QUESP	-118.3 (41.7 - 162.0)	1160.5 (1040.3-1269.3)
HW-QUESP	300.0 (0 - 416.1)	1225.2 (1224.6 - 1226.0)
LB-Conc	595.4 (537.2 - 653.5)	308.3 (210.1 – 406.4)
EH-Conc	655.6 (516.3 - 794.8)	198.5 (0-841.6)
HW-Conc	607.3 (494.4 - 720.2)	327.1 (162.2 - 492.0)

Table 2.1: The estimated chemical exchange rates of iopromide (Hz).  
The 95% CIs are shown in parentheses.

Both methods produced wide CIs, which further emphasized the difficulty in estimating rapid exchange rates with these methods.

The LB-QUESP method estimated the  $k_{ex}$  rate for the slowly exchanging amide proton at 4.2 ppm to be similar to the rate determined from Bloch fitting, and this estimate had narrow CIs (Fig. 2.6A; Table 2.1). The HW-QUESP method estimated  $k_{ex}$  with less accuracy and with wide CIs that indicated less precision relative to LB-QUESP, which was consistent with the simulations for slow  $k_{ex}$  rates. The EH-QUESP method showed an incorrect slope with this experimental data (Fig. 2.3B vs. 2.6B). This method had a very small dynamic range relative to experimental noise over the experimental conditions used in this study, which presumably led to this incorrect slope. These results demonstrated that LB-QUESP produced the most accurate and most precise estimates of  $k_{ex}$  for slow  $k_{ex}$  rates, relative to HW-QUESP and EH-QUESP.

Conversely, HW-QUESP produced an accurate estimate for the  $k_{ex}$  rate for the rapidly exchanging proton that resonated at 5.6 ppm, and this estimate had narrow CIs that demonstrated outstanding precision (Fig. 2.6F). The EH-QUESP method also estimated  $k_{ex}$  with excellent accuracy and precision (Fig. 2.6E). LB-QUESP produced an inaccurate estimate with CIs that had no upper bound, which demonstrated poor precision for this

method (Fig. 2.6D). These results demonstrated that HW-QUEST and EH-QUEST produced accurate and precise estimates of fast  $k_{ex}$  rates relative to LB-QUEST.

The LB-Conc, EH-Conc, and HW-Conc methods each underestimated  $k_{ex}$  for the rapidly exchanging proton at 5.6 ppm, which was consistent with the results from the simulations (Fig. 2.7; Table 2.1). Each concentration-based analysis method estimated  $k_{ex}$  with wide CIs for the slowly exchanging proton at 4.2 ppm, which indicated that the precisions of these analysis methods are very sensitive to experimental noise. Based on these results, the concentration-based analysis methods produce inaccurate and imprecise estimates of exchange rates relative to the other methods.

## 2.6. Discussion

The Bloch fitting method produced the most precise results, especially when fitting was simultaneously applied to multiple CEST spectra. However, Bloch fitting requires substantial computation time, and some expertise is required to ensure that the fitting achieves the best result. Therefore, Bloch fitting should be used only when the highest accuracy and precision are required, and when expertise and time are available.

The simulations and experimental results both demonstrated that QUEST and QUESTP could produce accurate estimates of slow exchange rates. Increasing the saturation power can increase the accuracy of exchange rate estimates made with QUEST. QUESTP produced results with accuracies that were intermediate between QUEST and QUESTP, so that QUEST is also preferable to QUESTP for this study. Yet QUESTP fits more data than QUEST and QUESTP, which has potential to mitigate random noise, and therefore QUESTP may have advantages when fitting noisy CEST results. Most importantly, QUEST, QUESTP, and QUESTP fail to produce accurate estimates of fast chemical exchange rates.

HW-QUEST and EH-QUEST can produce accurate estimates of fast exchange rates. Fast exchanging protons experience less saturation than expected, which leads to a systematic overestimation of the saturation power experienced by these protons. HW-QUEST includes the saturation power in the x- and y-values of the plot (Eq. [2.11]), so that a systematic error in the saturation power is cancelled. Similarly, fast exchanging protons generate less CEST than expected for the saturation power that is applied. EH-QUEST includes the CEST measurement in the x- and y-values of the plot (Eq. [2.10]), so that a

systematic error in generating a CEST measurement is cancelled. Conversely, LB-QUESP has separate x- and y-values, and, therefore, cannot cancel this systematic error. HW-QUESP plots have a greater range of saturation powers that produce a linear plot, relative to EH-QUESP (Fig.2.3C vs. 2.3B). Therefore, HW-QUESP is the best overall method for estimating fast chemical exchange rates.

The QUEST, QUESP, QUESPT, and LB-QUESP methods produced more accurate estimates of fast exchange rates with shorter  $T_{1w}$  relaxation times. When saturation is initially applied, the saturation pulse equally affects protons undergoing slow and fast exchange. As the saturation period continues over time, the fast exchanging protons leave the agent more quickly and experience less saturation than expected. Fast  $T_{1w}$  relaxation truncates the saturation process, which reduces this effect of less-than-expected saturation of fast exchanging protons.

The concentration plot methods failed to produce accurate estimates. Furthermore, this method requires multiple samples that must have identical conditions such as  $T_{1w}$  and  $T_{2w}$  times, pH, and temperature. Therefore, this method has technical limitations in addition to systematic analytical errors, and is not recommended for estimating  $k_{ex}$  rates. For comparison, another method has been reported that estimates  $k_{ex}$  rates relative to changes in  $T_{1w}$  time of a series of samples with the same concentration (25). Linear " $T_{1w}$  plot" methods can be derived that are similar to the linear concentration plot methods shown in this report. This previous report of the  $T_{1w}$  method also demonstrated inaccuracies in determining  $k_{ex}$  rates, primarily due to the limited dynamic range of  $T_{1w}$  times that can be tested relative to experimental noise. This method also requires multiple samples that must have identical conditions other than  $T_{1w}$ , which is technically challenging. For these reasons, the  $T_{1w}$  plot methods are considered to be inferior to the methods tested in this report, so that we did not include the  $T_{1w}$  plot methods in our studies.

Other methods that estimate chemical exchange rates from CEST results have been developed that directly account for incomplete saturation and direct saturation of water (3,4). These methods are especially designed for diamagnetic CEST agents that have slow chemical exchange rates, and have not been used to estimate fast exchange rates. As with Bloch fitting, these methods are based on impressive attention to analytical details that avoid assumptions made with more simplistic linear analysis methods, and therefore can be used for a robust range of CEST experiments. Yet these detailed algorithms

require expertise to develop the computer algorithms, and can require substantial computation time. The HW-QUEST method provides a more simplistic alternative for estimating chemical exchange rates, especially fast exchange rates, provided that the conditions of the CEST experiments meet the assumptions of this method.

## **2.7. Conclusions**

These simulations and experimental results demonstrate that the HW-QUEST method produces the best estimates of fast chemical exchange rates from CEST MRI results. QUEST and LB-QUEST produce the best estimates of slow exchange rates especially for samples with short  $T_{1w}$  relaxation times. Bloch fitting produces the most precise methods especially when simultaneously fit to a series of CEST spectra, although expertise and computation time are required to achieve precise results with Bloch fitting relative to the relatively simplistic linear analysis methods.

## CHAPTER 3

THE RECIPROCAL LINEAR QUEST ANALYSIS METHOD  
FACILITATES THE MEASUREMENTS OF  
CHEMICAL EXCHANGE RATES  
WITH CEST MRI

## PUBLICATION:

Edward A. Randtke, Liu Qi Chen, L. Rene Corrales, Mark D. Pagel. The Reciprocal Linear QUEST Analysis Method Facilitates the Measurements of Chemical Exchange Rates with CEST MRI. *Contrast Media Molec. Imaging* 2013, *In Press*.

## POSTER PRESENTATION:

Edward A. Randtke, Liu Qi Chen, Mark D. Pagel. New Analysis Methods for Measuring Chemical Exchange Rates Using CEST MRI. World Molecular Imaging Congress Meeting, 2013.

### **3.1 Abstract**

MRI contrast media that are detected via Chemical Exchange Saturation Transfer (CEST) often require an accurate estimation of their chemical exchange rate,  $k_{ex}$ . A variety of analysis methods have been proposed to estimate  $k_{ex}$ , including the non-linear QUEST analysis method that evaluates the CEST amplitude as a function of saturation time. We have derived a linear version of QUEST, termed the Reciprocal Linear QUEST (RL-QUEST) method. Our simulations and experimental results show that RL-QUEST performs as well as QUEST, while providing a more simplistic fitting procedure. Although CEST results should be acquired with saturation power that has a nutation rate that is faster than  $k_{ex}$  of the CEST agent, an exact determination of the saturation power is not required to accurately estimate  $k_{ex}$  with RL-QUEST. This new analysis method requires a determination of the CEST agent's concentration, which is straightforward for the analyses of CEST agents in chemical solutions, but may be a limitation during in vivo CEST MRI studies. Based on the results of this study and previous studies, we provide recommendations for the linear analysis method that should be employed for each type of CEST MRI study.

### **3.2 Introduction**

A variety of MRI contrast media have been developed that can be detected via Chemical Exchange Saturation Transfer (CEST) (1). During a CEST MRI experiment, radio frequency saturation is applied at the chemical shift of a labile proton on the CEST agent, eliminating the coherent net magnetic moment of this proton. Chemical exchange of the labile proton from the CEST agent to water results in transferring the effect of saturation to the water MR resonance. The resulting detection of the partially suppressed water signal using standard MRI protocols can be iterated over a range of saturation frequencies, which can be used to construct a CEST spectrum that is used to measure CEST (Fig. 3.1) (2).

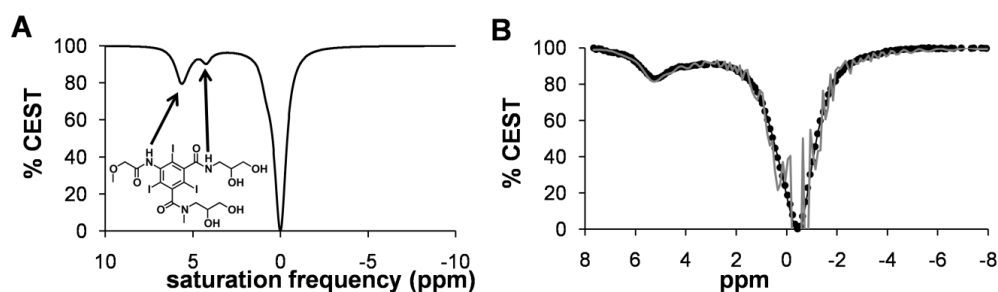


Figure 3.1: CEST spectra of iopromide

A) A simulated CEST spectrum of iopromide at 4  $\mu\text{T}$  saturation power and 0.5s saturation time. The chemical structure of iopromide is shown in the inset. B) A simulated CEST spectrum of iopromide at 9  $\mu\text{T}$  saturation power and 0.25 s saturation time (dots). Bloch fitting without a Gaussian point spread function showed a poor fit to the simulated spectrum (gray line), while Bloch fitting with a Gaussian point spread function using a sigma of 56Hz showed a good fit to the simulated spectrum (black line).

The development of a CEST agent often includes a measurement of the chemical exchange rate,  $k_{\text{ex}}$ , to ensure that the agent has acceptable chemical exchange properties for a specific biomedical application and/or for selecting the best CEST MRI detection protocol for the agent (3-8). A variety of methods have been created to estimate  $k_{\text{ex}}$  from CEST MRI results, including fitting CEST spectra with Bloch-McConnell equations modified for chemical exchange (also known as Bloch fitting), and the QUEST and QUESP methods that are dependent on saturation time and saturation power, respectively (9,10). Bloch fitting is a very accurate and precise method, but requires expertise and time to ensure that the fitting is properly performed. Although QUEST and QUESP are non-linear fitting methods, both of these methods offer a more simplistic fitting process relative to Bloch fitting. We and others have developed linear versions of QUESP that further simplify the fitting procedure (11,12).

We hypothesized that a linear QUEST analysis method may offer the same practical advantages for estimating  $k_{\text{ex}}$  from CEST results as shown from the linear versions of QUESP analysis. We investigated several linear versions of QUEST using simulated results that had known chemical exchange rates. We then measured CEST from iopromide (Ultravist<sup>TM</sup>, Bayer Health Care, Inc.), and compared the estimates of  $k_{\text{ex}}$  with non-linear QUEST and a linear QUEST method. These results have led us to propose recommendations for the use of various analysis methods for estimating  $k_{\text{ex}}$  using CEST MR studies.

### 3.3 Theory

Assuming that a CEST agent instantaneously reaches steady-state saturation (but does not necessarily reach complete saturation), a previous report has shown that CEST can be described as a function of saturation time ( $t_{sat}$ ) (Eq. [3.1]) (10).

$$\frac{M_0 - M_S}{M_0} = \frac{\alpha k_{ex} \chi}{R_{1w} + k_{ex} \chi} [1 - e^{-(R_{1w} + k_{ex} \chi) t_{sat}}] \quad [3.1]$$

where:

$$\chi = \frac{n_{CA} [CA]}{n_{H_2O} [H_2O]} \quad [3.2]$$

$$\alpha = \frac{\omega_1^2}{\omega_1^2 + R_1 R_2} \quad [3.3]$$

$$R_{1,2} = R_{1A,2A} + k_{ex} - \frac{k_{ex}^2 \chi}{R_{1w,2w} + k_{ex} \chi} \quad [3.4]$$

$M_S$ ,  $M_0$ : water signal with saturation (S) and without saturation (0)

[CA], [H<sub>2</sub>O]: concentration of the contrast agent and water

$n_{CA}$ ,  $n_{H_2O}$ : number of magnetically equivalent exchangeable protons on the agent and water

$R_{1A}$ ,  $R_{2A}$ ,  $R_{1w}$ ,  $R_{2w}$ : Inherent  $R_1$  and  $R_2$  relaxation rates of the agent (A) and water (w) without chemical exchange.

The QUEST method fits the exponential term of Eq. [3.1] to CEST measurements determined with a range of saturation times. Eq. [3.1] can be simplified for CEST measured with a very long saturation time (Eq. [3.5]). The ratio of CEST measurements at short saturation times relative to a very long saturation time is only dependent on an exponential term (Eq. [3.6]). This non-linear relationship can be rearranged to create linear relationships (Eq. [3.7]).

$$\left( \frac{M_0 - M_S}{M_0} \right)_{t=\infty} = \frac{\alpha k_{ex} \chi}{R_{1w} + k_{ex} \chi} \quad [3.5]$$

$$\frac{\left( \frac{M_0 - M_S}{M_0} \right)_{t < \infty}}{\left( \frac{M_0 - M_S}{M_0} \right)_{t = \infty}} = 1 - e^{-(R_{1w} + k_{ex} \chi) t_{sat}} \quad [3.6]$$

$$-\ln \left[ 1 - \frac{\left( \frac{M_0 - M_S}{M_0} \right)_{t < \infty}}{\left( \frac{M_0 - M_S}{M_0} \right)_{t = \infty}} \right] = (R_{1w} + k_{ex} \chi) t \quad [3.7a]$$

$$\frac{1}{-\ln \left[ 1 - \frac{\left( \frac{M_0 - M_S}{M_0} \right)_{t < \infty}}{\left( \frac{M_0 - M_S}{M_0} \right)_{t = \infty}} \right]} = \frac{1}{(R_{1w} + k_{ex} \chi) t} \quad [3.7b]$$

$$1 = \frac{-\ln \left[ 1 - \frac{\left( \frac{M_0 - M_S}{M_0} \right)_{t < \infty}}{\left( \frac{M_0 - M_S}{M_0} \right)_{t = \infty}} \right]}{(R_{1w} + k_{ex} \chi) t} \quad [3.7c]$$

Equation 3.7a is known as the Linear QUEST (L-QUEST) method and places greater weight on CEST measured with longer saturation times, as these data points affect the slope the most. Equation 3.7b is known as the Reciprocal Linear QUEST (RL-QUEST) method and places greater weight on CEST measured with shorter saturation times, since these data points affect the slope of the fit line the most. The chemical exchange rate,  $k_{ex}$ , can then be determined from the slope of these linear equations, assuming that the concentration of the agent is known and is sufficiently high that  $k_{ex} \chi \gg R_{1w}$ . Equation [3.7c] is known as the Unitary Linear QUEST (UL-QUEST) method and places equal weight on CEST measured at all saturation times, as each point affects the y intercept equally. A value of  $k_{ex}$  can be determined at each time point, and the average value of  $k_{ex}$  can be used as the estimate of the chemical exchange rate.

### 3.4 Methods

#### 3.4.1 Simulations

The Bloch-McConnell equations modified for chemical exchange were used to generate CEST spectra of iopromide (9). All simulations used chemical shifts of 5.6 ppm and 4.2 ppm for each amide resonance, 0.0 ppm for the water resonance, and 0.87 ppm for the hydroxyl group resonance that was set to an exchange rate of 400 Hz. Each simulation tested saturation times of 0.25 to 10 s, chemical exchange rates from 10 to 1200 Hz, and  $T_1$  relaxation times from 0.1 to 10 s. The saturation power was set to 4  $\mu$ T, and the concentration was set to 200 mM. Lorentzian line shape fitting was used to measure the CEST effect ( $M_S$ ) for each amide from each simulated spectrum, using spectra normalized from 0% to 100% water signal (which set  $M_0$  equal to 100%) (13). The Lorentzian

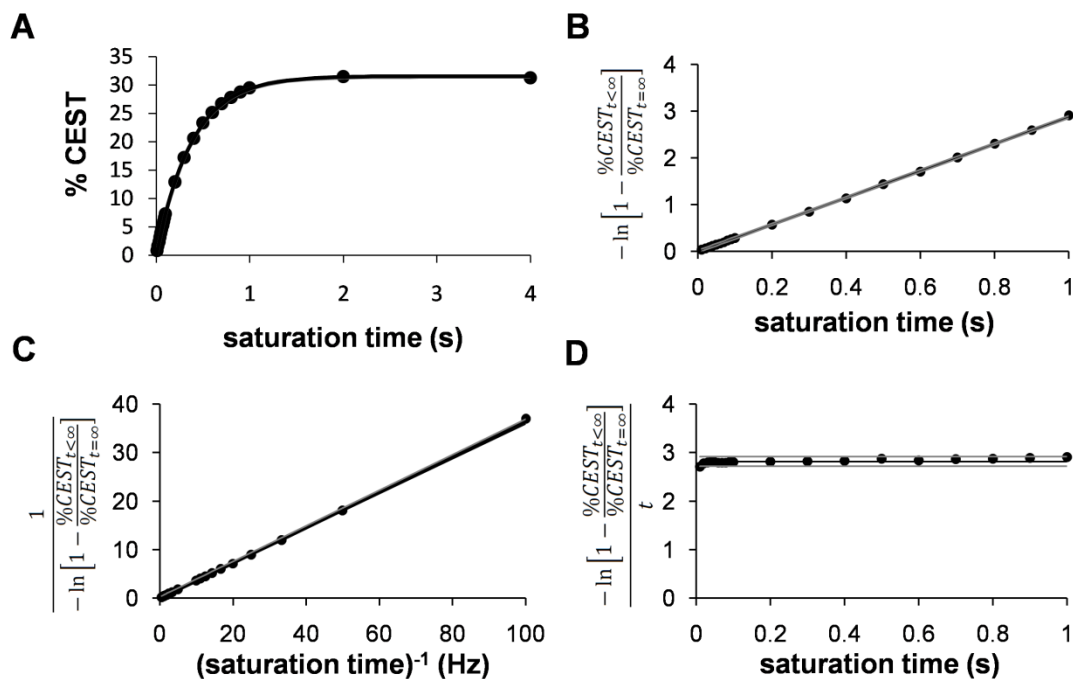


Figure 3.2: Linear QUEST simulation

Analyses of chemical exchange rates using A) the QUEST method, B) the L-QUEST method, C) the RL-QUEST method, and D) the UL-QUEST method. The slope of the L-QUEST plot or the RL-QUEST plot can be used to measure the chemical exchange rate,  $k_{ex}$ . Each data point of the UL-QUEST plot can be used to determine  $k_{ex}$ , and the average of these determinations of  $k_{ex}$  can be used as the estimate of the chemical exchange rate.

lineshape fittings were performed with MATLAB v2011a (Mathworks, Inc. Natick MA) using the *trust-region-reflective* algorithm to reach a convergence criterion of  $10^{-16}$ .

The QUEST method was performed by fitting Eq. [3.1] to the measured CEST effects of the simulated results to estimate the chemical exchange rate of the amide at 5.6 ppm (10). Fittings were performed by allowing  $R_{1w}$  to be a fitted parameter, which has been shown to produce accurate estimates of  $k_{ex}$ .  $R_{2w}$  was set to  $R_{1w}$  for all of these fittings. The three versions of the linear QUEST method were also used to estimate chemical exchange rates from the simulated CEST results. All non-linear fittings (QUEST) were performed with Matlab v2011a using the *trust-region-reflective* algorithm to reach a convergence criterion of  $10^{-16}$ , while linear fittings (the three linearizations of QUEST) were performed using the *linear least squares* algorithm.

### 3.4.2 Experimental Studies

Iopromide (Ultravist™, Bayer Health Care, Inc.) was provided by the Department of Medical Imaging of the University of Arizona. Iopromide was diluted to 100 mM and adjusted to pH 6.8 using 0.1 M HCl. After preparation, 10% D<sub>2</sub>O was added to each solution to maintain a lock signal during NMR studies. The addition of D<sub>2</sub>O caused deuteration of 10% of the labile protons of iopromide, which effectively reduced the concentration of protonated iopromide relative to protonated water. This dilution was taken into consideration when determining the value of  $\chi$ .

All CEST experiments were performed using a 600 MHz Varian Inova NMR spectrometer with an inverse cryoprobe. Samples were analyzed at 37.3°C. The temperature was calibrated by measuring the separation of resonances of neat methanol and ethylene glycol samples between 25°C and 40°C (14). The probe was manually tuned to each sample, and the 360° pulse time was measured before acquiring each CEST spectrum to estimate the saturation power. The 360° pulse time was also measured after acquiring each CEST spectrum to ensure that the saturation power was constant when acquiring the CEST spectrum. The CEST spectra were acquired with a continuous-wave saturation pulse and saturation frequencies set at +8 to -8 ppm in 0.1 ppm increments. Each scan was averaged four times. Saturation times of 0.25, 0.5, 1.0, 2.0, 4.0, and 8.0 s were tested with a relaxation delay from 7.75 to 0 s to maintain a total time of 8 s for the pre-acquisition period. These studies were conducted with a saturation power of 1.0, 1.5, 2, 3, 4, 6, and 8  $\mu$ T.

Bloch fitting was used to simultaneously fit all experimental CEST spectra to obtain accurate estimates of the chemical exchange rate of the protons resonating at 5.6 and 4.2 ppm (15). Short pulse times of a continuous-wave saturation pulse can create a sinc-shaped saturation frequency profile, which can broaden the bandwidth of the saturation. To compensate for this broadening, each point of the experimental CEST spectrum was modeled as a Gaussian-shaped point spread function, which improved the fitting of the CEST spectrum acquired with a short 0.25 s saturation time. The integrating factor method was used during the Bloch fitting. The *lsqcurvefit* routine with the *trust-region-reflective* algorithm was used to initially fit the CEST spectra, which resulted in rough parameter estimates. The *nlinfit* routine with the *Levenburg-Marquardt* algorithm was then used to fit the CEST spectra to obtain the final parameter estimates. The Jacobian from the *nlinfit* routine was used to determine confidence intervals for fitted parameters.

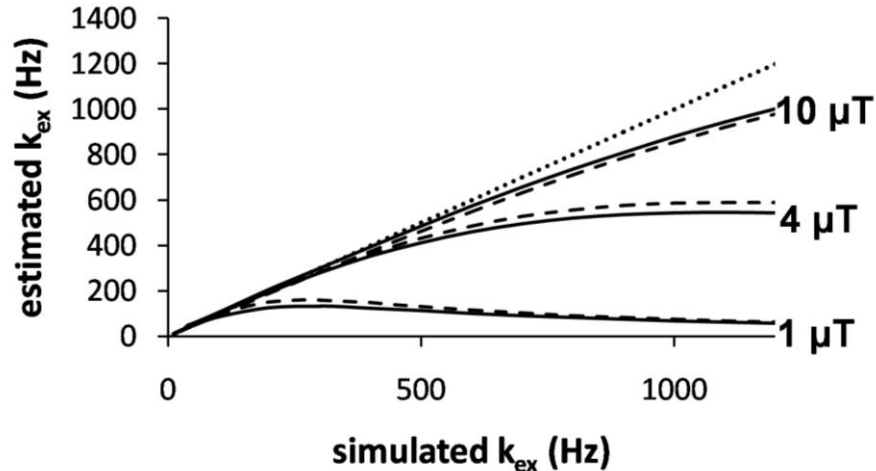


Figure 3.3: Comparison of QUEST and RL-QUEST

The dependence of QUEST and RL-QUEST on saturation power. The chemical exchange rate,  $k_{ex}$ , estimated with QUEST (dashed lines) and RL-QUEST (solid lines) from simulated CEST spectra showed accurate estimations of slow exchange rates at all saturation powers, but underestimated fast exchange rates especially at low saturation powers. The underestimations were comparable for QUEST and RL-QUEST. A dotted line with slope=1 is shown to aid visualization of the results.

Lorentzian line shape fitting was used to measure the CEST effect ( $M_S$ ) for each amide from each experimental spectrum as previously described, using spectra normalized from 0% to 100% water signal (which set  $M_0$  equal to 100%) (13). The fittings were performed with Matlab v2011a using the *trust-region-reflective* algorithm to reach a convergence criterion of  $10^{-16}$ .

The QUEST and RL-QUEST methods were used to estimate  $k_{ex}$  rates from the experimental CEST measurements determined from the Lorentzian line shape fittings (10). For the QUEST method, Eq. [3.1] was fit to the experimental results by varying  $k_{ex}$  and  $R_{1w}$ , while  $R_{2w}$ ,  $R_{1A}$ , and  $R_{2A}$  were set to the value of  $R_{1w}$ , which has been previously shown to produce accurate estimates of  $k_{ex}$ . All non-linear fittings (QUEST) were performed with Matlab v2011a using the *trust-region-reflective* algorithm to reach a convergence criterion of  $10^{-16}$ , while linear fittings (RL-QUEST) were performed using the *linear least squares* algorithm.

### 3.5 Results

#### 3.5.1 Simulations

The Bloch-McConnell equations were used to generate CEST spectra of iopromide using a range of chemical exchange rates and saturation times (Fig. 3.1). Each CEST spectrum was fit with a function of Lorentzian line shapes to measure the CEST effects of both amide protons, to simulate our protocol used to analyze experimental CEST spectra. Previous reports have shown that the Lorentzian line shape fitting can measure CEST with excellent accuracy and can account for the effects of direct saturation of water (13).

The CEST measurements were used to estimate exchange rates using the QUEST method and the three linear QUEST methods (Fig. 3.2). The QUEST method showed an outstanding fit to the simulated results

throughout the entire range of saturation times. Of the three linear QUEST methods, RL-QUEST places greater weight on CEST measured with shorter saturation times, which results in a relationship that has the largest dynamic range. Based on these results, only QUEST and RL-QUEST were compared for the remainder of this study.

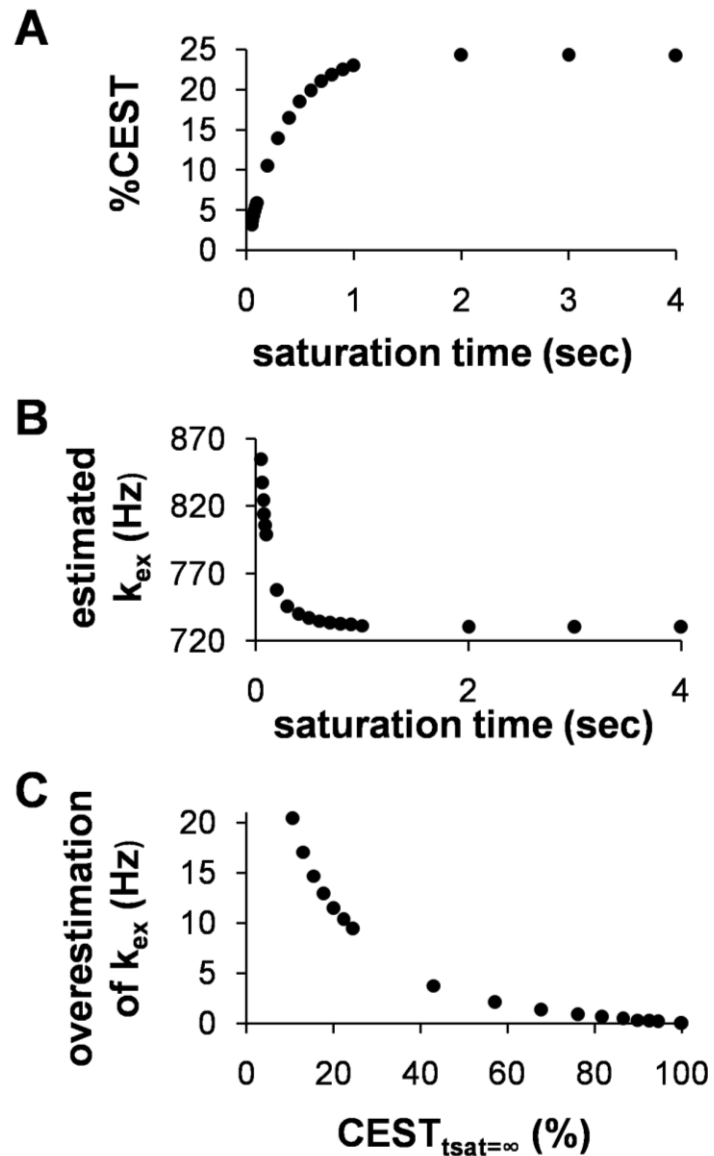


Figure 3.4: Saturation Dependence of RL-QUEST  
The dependence of estimated  $k_{ex}$  on CEST<sub>tsat=∞</sub> when using RL-QUEST. A) Short saturation times for CEST<sub>tsat=∞</sub> caused lower CEST. B) An underdetermined CEST<sub>tsat=∞</sub> caused  $k_{ex}$  to be overestimated. C)  $k_{ex}$  was only overestimated by 4% when CEST<sub>tsat=∞</sub> was underdetermined by 50%, demonstrating that estimates of  $k_{ex}$  are insensitive to underdetermined CEST<sub>tsat=∞</sub> values when using RL-QUEST.

We compared chemical exchange rates estimated with QUEST and RL-QUEST using different saturation powers (Fig. 3.3). The nearly identical estimates from both methods showed that the simplistic fitting with LR-QUEST can substitute for the more complicated non-linear fitting with QUEST. This result also shows that both methods can accurately estimate slow chemical exchange rates, but faster chemical exchange rates are underestimated. This underestimation can be mitigated by using high saturation powers, as shown previously for QUEST analyses (10). These results support the guideline that the nutation rate of the saturation pulse must be greater than the chemical exchange rate to accurately measure exchange rates with CEST MR methods (9).

Because obtaining a CEST effect with an infinite saturation time is impractical, we analyzed the effect of truncating the  $\text{CEST}_{t=\infty}$  saturation time on the estimate of the chemical exchange rate (Fig. 3.4). These results showed that chemical exchange rate was overestimated with a truncated saturation time used for  $\text{CEST}_{t=\infty}$ . However, this overestimation was negligible for long saturation times of 1 to 4 s that are practical to implement. Furthermore, a 50% reduction in  $\text{CEST}_{t=\infty}$  with a saturation time of 0.25 s (Fig. 3.4B) only produced a 5% overestimation in the chemical exchange rate (Fig. 3.4C), which further demonstrated the insensitivity of estimating chemical exchange rates with finite saturation times used to measure  $\text{CEST}_{t=\infty}$ .

### 3.5.2 Experimental Results

CEST spectra were acquired at various saturation times and saturation powers. The saturation powers were calibrated using a  $360^\circ$  excitation pulse to mitigate the effects of radiation damping. Bloch fitting was used to simultaneously fit to a series of 36 CEST spectra of iopromide that were acquired with different saturation times and saturation

Method	4.2 ppm	5.6 ppm
<b>Bloch Fitting</b>	133.1 (117.5, 150.7) [-11.7%, +13.2%]	1130.8 (1074.3, 1190.2) [-5.00%, +5.25%]
<b>QUEST</b>	80.0 (74.4, 86.1) [-7.0%, +7.6%]	815.0 (726.3, 914.4) [-10.9%, +12.2%]
<b>RL-QUEST</b>	112.8 (99.6, 130.0) [-11.7%, +15.2%]	824.6 (792.3, 859.6) [-3.9%, +4.2%]

Table 3.1: Estimates of chemical exchange rates (Hz)

The 95% confidence intervals expressed in Hz are shown in parenthesis.

The 95% confidence intervals expressed as a percentage of the estimated exchange rates are shown in brackets.

powers (Fig. 3.5) (15). Our past results have shown that simultaneously fitting a series of CEST spectra produces more precise estimates of  $k_{\text{ex}}$  relative to fitting a single spectrum (16). The chemical exchange rates of the amide proton resonating at 4.2 ppm and 5.6 ppm were estimated to be 133.1 and 1130.8 Hz, respectively (Table 3.1).

Lorentzian line shapes were fit to each experimental CEST spectrum to measure CEST (Fig. 3.5A). These results were then used to estimate the chemical exchange rates. The amide proton resonating at 4.2 ppm was estimated to have a  $k_{\text{ex}}$  value of 80.0 and 112.8 Hz using QUEST and RL-QUEST, respectively (Fig. 3.5B,C; Table 1). This result indicated that RL-QUEST provided a more accurate estimate than QUEST, using results from Bloch fitting as the “gold standard”. These estimates used experimental results acquired with 2.25  $\mu\text{T}$  saturation power. Lower saturation powers caused estimates of  $k_{\text{ex}}$  to be underestimated, because low saturation powers and short saturation times caused weak CEST effects relative to CEST spectral noise, which reduced the accuracy of Lorentzian line fitting (Fig. 3.6A). Higher saturation powers caused estimates of  $k_{\text{ex}}$  to be overestimated, because higher saturation powers caused wider, overlapping CEST peaks at 4.2 and 5.6 ppm, which also reduced the accuracy of Lorentzian line fittings.

The amide proton resonating at 5.6 ppm was estimated to have a  $k_{\text{ex}}$  value of 815.0 and 824.6 Hz using QUEST and RL-QUEST, respectively (Fig. 3.5D,E; Table 1). Again, this result indicated that RL-QUEST provided a more accurate estimate than QUEST, using results from Bloch fitting as the “gold standard”. These estimates were obtained with a saturation power of 8  $\mu\text{T}$ , which has the highest nutation rate of the saturation powers used in this study. The nutation rate of the saturation at this power level was below the proton’s rapid chemical exchange rate, causing QUEST and RL-QUEST to underestimate the rapid chemical exchange rate. Lower saturation powers caused greater underestimations of  $k_{\text{ex}}$  for this rapidly exchanging amide proton (Fig. 3.6B). This experimental underestimation matched the results from the simulations (Fig. 3.3).

### **3.6 Discussion**

Our simulations and experimental results demonstrated that RL-QUEST performs as well as QUEST when estimating chemical exchange rates. RL-QUEST has practical advantages relative to QUEST, because linear fitting methods are faster than non-linear fitting methods. Furthermore, RL-QUEST has a y-intercept value that is zero, so that RL-

QUEST analysis may be performed with only two CEST measurements (at  $t < \infty$  and  $t > \infty$ ), which further accelerates the analysis relative to non-linear QUEST.

Both QUEST and RL-QUEST determine a more accurate  $k_{ex}$  when a high saturation power

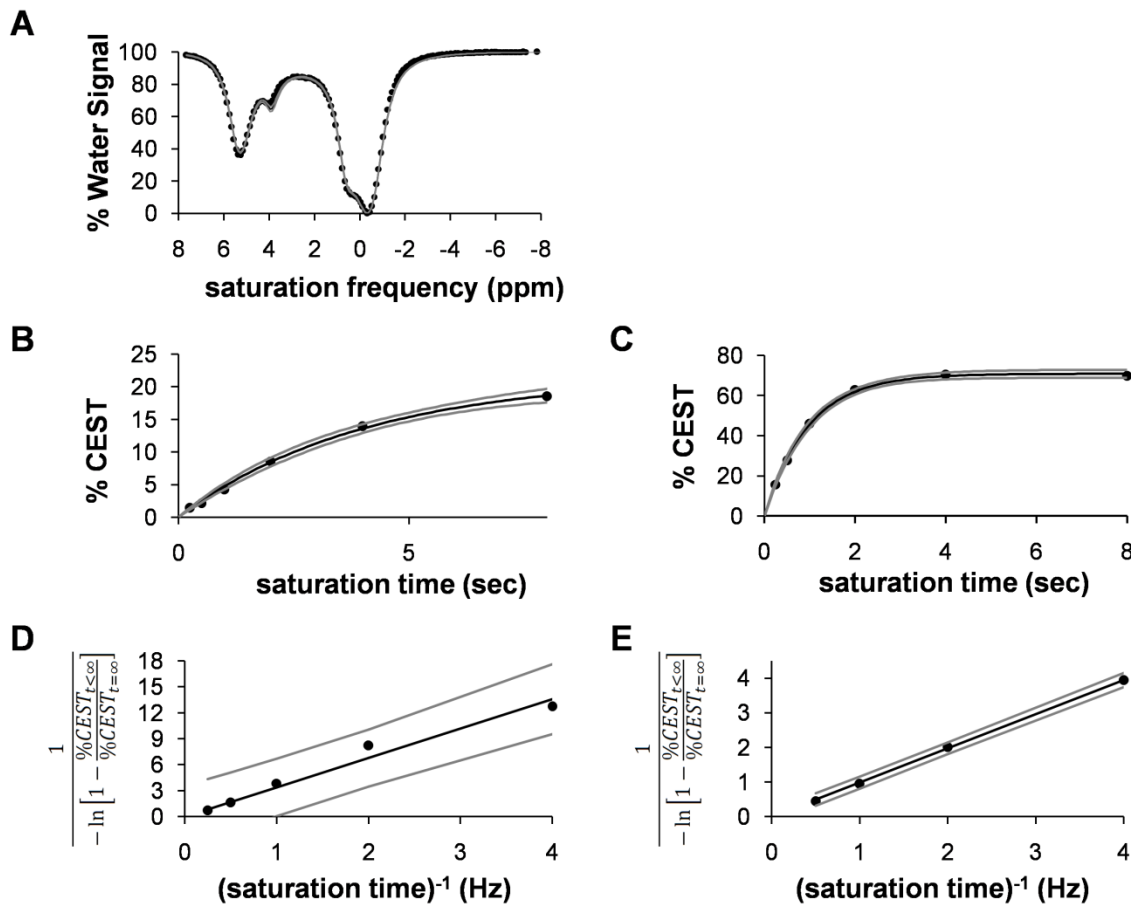


Figure 3.5: Estimation of  $k_{ex}$  with RL-QUEST

A) A CEST spectrum of iopromide was acquired with 4.45  $\mu\text{T}$  saturation power and 4 s saturation time. B, C) The QUEST method and D, E) the RL-QUEST method were used to estimate  $k_{ex}$  for the protons resonating at 4.2 ppm (B, D) using CEST measurements determined from 1.5  $\mu\text{T}$  saturation power, and at 5.6 ppm (C, E) using CEST measurements determined from 8  $\mu\text{T}$  saturation power. Experimental data points are shown as circles, the fitted result is shown as a black line, and the 95% confidence intervals are shown as gray lines.

is used or when  $k_{ex}$  is slow. In addition, these methods require that the concentration of the agent must be known to determine  $k_{ex}$ . For comparison, spin-lock MRI experiments can determine  $k_{ex}$  by measuring the  $R_{1\rho}$  relaxation rate in the rotating frame (17,18).  $R_{1\rho}$  can be converted to  $k_{ex}$  under strong saturation conditions, slow  $R_1$  and  $R_2$  relaxation rates, slow  $k_{ex}$  rates, and when the concentration of the agent is known. These similarities between QUEST, RL-QUEST and spin-lock experiments have been noted previously (17,18).

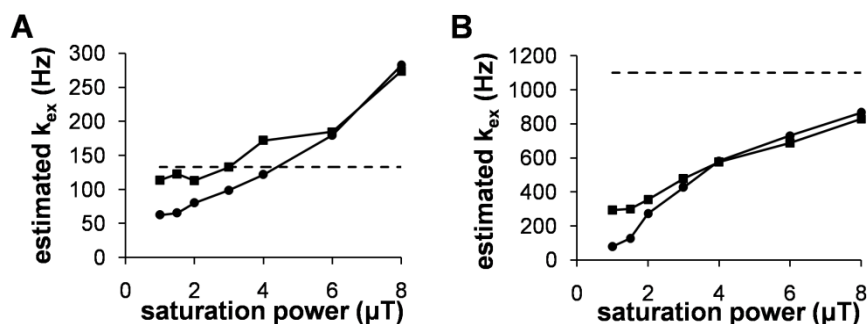


Figure 3.6: Estimated exchange rate vs. saturation power

A) The estimated  $k_{ex}$  of the slowly-exchanging proton resonating at 4.2 ppm showed similar estimates with RL-QUEST (squares) and QUEST (circles). Low saturation powers improved the Lorentzian line shape fitting of experimental CEST spectra, which led to accurate estimations of  $k_{ex}$  relative to the  $k_{ex}$  estimated with Bloch fitting (dashed line). However, very low saturation powers led to inaccurate estimations of  $k_{ex}$  due to low CEST effects. B) The estimated  $k_{ex}$  of the rapidly-exchanging proton resonating at 5.6 ppm showed similar estimates with RL-QUEST (circles) and QUEST (squares), but these estimates were underestimated relative to the  $k_{ex}$  estimated with Bloch fitting (dashed line), especially with low saturation powers.

We have recently completed a similar evaluation of the non-linear QUESP analysis method and linear versions of QUESP, which evaluate the change in CEST as a function of power (16; Chapter 2). Similar to this study, our evaluation of linear QUESP methods showed the advantages of using a linear version known as LB-QUESP when estimating slow  $k_{ex}$  values, and another linear version known as HW-QUESP when estimating fast  $k_{ex}$  values. However, these linear versions of QUESP depend on accurately determining the values of saturation powers (for QUESP and LB-QUESP) or accurately determining the increments of saturation powers (for HW-QUESP). The calibration of saturation power can be challenging during NMR studies due to radiation damping. More importantly, saturation power may be variable during in vivo MRI studies due to  $B_1$  inhomogeneity. For comparison, the accuracy of estimating  $k_{ex}$  with RL-QUEST does not depend on the accuracy of determining the saturation power. RL-QUEST only requires a sufficient saturation power so that the nutation rate exceeds the chemical exchange rate.

RL-QUEST is complimentary to QUESTRA, which is another linear version of QUEST analysis (20). QUESTRA evaluates the ratio of water signals in a CEST spectrum at opposite chemical shift values about the direct saturation of water at 0 ppm (which is a version of asymmetry analysis of a CEST spectrum). The simulations of QUESTRA showed that  $k_{ex}$  could be accurately estimated as long as the nutation rate of the saturation power exceeds  $k_{ex}$ . Only one CEST spectrum is required for QUESTRA analysis, while two

CEST spectra are required for RL-QUEST analysis (at  $t < \infty$  and  $t > \infty$ ), so that QUESTRA may be faster than RL-QUEST. However, a linear analysis based on one experimental data point and a zero y-intercept is highly dependent on the variability of the single data point, so that CEST spectra with multiple saturation times are recommended for both methods to improve the quality of the fitting process.

QUESTRA automatically accounts for overlap between the peaks in a CEST spectrum that represent CEST from an amide proton and the direct saturation of water. However, QUESTRA does not account for overlapping CEST effects such as the effects observed with iopromide. In addition, QUESTRA does not account for asymmetric effects in CEST spectra such as the endogenous MT effect observed during CEST studies with tissues (21). QUESTRA is also dependent on  $B_0$  homogeneity. As shown in our previous studies and in our current study with RL-QUEST, Lorentzian line fittings of CEST spectra avoids complications caused by the direct saturation of water, overlapping CEST effects, other asymmetric features of CEST spectra including the MT effect, and  $B_0$  inhomogeneities. Therefore, we recommend that QUESTRA analyses should also employ Lorentzian line fitting analyses, which should provide similar benefits shown in our RL-QUEST analyses.

To estimate  $k_{ex}$ , RL-QUEST and QUESTRA inherently require an understanding of the concentration of the CEST agent relative to the concentration of water. Measuring the concentration of a CEST agent is straightforward for NMR studies of chemical solutions, but can be challenging during in vivo MRI studies (22). Conversely, LB-QUEST and HW-QUEST can estimate  $k_{ex}$  without also requiring a measurement of concentration, which provides advantages for in vivo studies. Therefore, we offer the following recommendations:

- ◆ If the concentration is known, and the saturation power is allowed to be sufficiently high so that the nutation rate of the saturation exceeds  $k_{ex}$ , then use RL-QUEST or QUESTRA to determine  $k_{ex}$ .
- ◆ If the concentration is unknown, and saturation powers are allowed to be sufficiently high so that the nutation rate of the saturation exceeds  $k_{ex}$ , and the saturation powers can be accurately determined, then use LB-QUEST to determine  $k_{ex}$ .
- ◆ If the concentration is unknown, and if saturation powers are not allowed to be sufficiently high so that the nutation rate of the saturation exceeds  $k_{ex}$ , and the

increments between saturation powers can be accurately determined, then use HW-QUEST to determine  $k_{ex}$ .

- ◆ If the concentration is unknown, and the increments between the saturation powers cannot be accurately determined, then use Bloch fitting to determine  $k_{ex}$ . Simultaneous Bloch fitting of a series of CEST spectra is recommended to improve the accuracy of estimating  $k_{ex}$ .

### **3.7 Conclusions**

Simulations and experimental results demonstrate that RL-QUEST performs as well as QUEST when estimating chemical exchange rates. RL-QUEST is a linear fitting method with a zero y-intercept, which has practical advantages relative to the non-linear QUEST fitting method. RL-QUEST requires a sufficient saturation power, but does not depend on measurements of saturation powers, and therefore has advantages relative to other analysis methods that estimate chemical exchange rates from CEST measurements based on saturation powers. Yet RL-QUEST requires an understanding of the CEST agent's concentration, which may limit the utility of this method.

## CHAPTER 4

EXCITON SELF TRAPPING IN  
COVALENTLY BONDED DYE-SILICA SYSTEMS

## PUBLICATIONS

Edward A. Randtke, L. Rene Corrales, Exciton Self-Trapping in Covalently Bonded Dye-Silica Systems. *Publication pending*

#### 4.1. Abstract

Dynamics of self trapped excitons are relevant to the fundamental understanding of energy transfer in amorphous systems. As a model system, we examined exciton dynamics in a system consisting of an organic dye tethered to an amorphous silica network. The self trapping of excitons was modeled via quantum chemical methods. The potential energy surface of the surrounding ion lattice in amorphous  $\text{SiO}_2$  was simulated to study the dynamics of exciton energy transfer through space. We found that this system lies in a moderate coupling regime. We combined the methods of Eyring and Landau-Zener to analyze energy exchange in the moderate coupling regime relevant to self trapped exciton transport. Our results indicate that excitons can transport through space into an acceptor dye with high quantum yield even after self trapping within the silica network.

#### 4.2. Introduction

Modern organic light emitting materials are comprised of organic components covalently tethered to inorganic components, such as silica (1, 2). An organic – inorganic bridge between the dye and the silica is critical for “solvating” organic complexes into close proximity to the inorganic material and to introduce luminescent centers into the organic-inorganic hybrid. Inclusion of the organic-inorganic bridge into a silica network is done through sol-gel chemistry where organosilicates are introduced along with tetraethoxysilane (TEOS) in a compatible solvent, which drives the aggregation of the organic phase into a microstructure that includes oily domains within a porous network of silica (3). These oily domains may contain luminescent molecular compounds or organic coated nanoparticles. Such systems can be cast as thin films and play an important technological role in many devices such as Organic Light Emitting Diodes (OLEDs) (4). Further developing and harnessing the potential of these hybrid systems can benefit from better characterization of exciton exchange rates and exciton transition energies. In this work, we theoretically examine how electronically excited states, in the form of triplet excitons, behave when introduced to the organic-inorganic system.

Previous studies demonstrated the validity of using DFT to examine amorphous silica (5, 6). It has also been shown that near the surface of quartz a triplet excitation introduced near a hydroxylated quartz surface will migrate to the surface and break the hydroxyl bond (7). These studies used Density Functional Theory (DFT) (8) to show how self trapping of excitons can be modeled theoretically in a way that produces results that qualitatively

agree with experimental results demonstrating self trapping and damage, and quantitatively agree with experimental measurement of emission energies.

We sought to extend this work to the study of a prototypical organosilica system with dye and amorphous SiO<sub>2</sub>. We sought to investigate the effects of excitation self trapping on bond distortion and breaking in the organosilica system, and whether self trapping can occur in both the organic dye and the amorphous silica. We further modeled the dynamics of energy transfer from the self-trapped state in the silica to the organic dye.

Established methods for modeling chemical reaction and exchange rates are the transition state theory of Eyring (9) and Landau-Zener (LZ) diabatic transition rates for systems with weak coupling (10, 11). A diabatic energy surface is the energy of the system if the system is perturbed quickly, so that the electronic energy does not transfer between atoms or through space. In contrast, adiabatic states represent the energy of the system if the system is perturbed very slowly, so that the exciton is free to move between atoms as the atoms are distorted through space (12). Refer to Figure A.2 in appendix A to see an explanation and schematic of adiabatic and diabatic states. Eyring theory is appropriate in systems that remain on the lower adiabatic surface as the chemical system progresses along its reaction coordinates towards products. An example is an inner sphere charge transfer reaction, or a dissociation reaction. LZ transition rates are appropriate when coupling is weak. Examples of weak coupling are the columbic interaction of Förster Resonance Energy Transfer (FRET) (13), wave function overlap of Dexter energy transfer (14), or outer sphere charge transfer (15).

However, in cases where the coupling is moderate, it is not clear which approach is appropriate. Furthermore, the assumption that sweep velocity is constant is not always valid, despite being necessary for the derivation of LZ transition rates. In our organosilica system, the coupling is moderate and the sweep velocity through the region of coupling is not constant because the region of coupling does not coincide with the saddle point. Therefore there is a need for better understanding of the appropriate approach in order to model our organosilicate system.

To meet this need, we integrated the theories of Eyring and LZ into one model in order to accurately describe transition rates when coupling is moderate and when the LZ sweep rate is not constant. We used Time Dependant Density Functional Theory as implemented in NWChem to model the multiple adiabatic potential energy surfaces in each of several

relevant inorganic-organic systems. The systems consist of a glass cluster with a chemisorbed organic group. The kinetic energy barrier and coupling values derived from this numerical approach were then used to calculate the LZ, Eyring and hybrid Eyring-LZ chemical transfer rates from exciton localization in the silica to exciton localization in the chemisorbed dye.

### 4.3. Theory

A general overview can be useful for understanding the theory of exciton kinetics. As an exciton self traps, the network of the nearby ions distorts to stabilize the localized exciton (16). This results in the ions resting within a basin in the 3N dimensional potential energy surface when the exciton localizes within either the silica or organic portion of a silica based organic-inorganic hybrid. The transfer of energy through the system is linked to the transfer of the ions from one basin to another. The transfer kinetics of the ions is determined using the method of Eyring (9). The transfer kinetics of the electronic energy is captured via a LZ transition from a lower energy adiabatic surface to a higher energy adiabatic surface as the ions sweep through the minimum energy pathway from one basin to another (10) (11). This ensures local conservation of energy as the ions push from one basin to another.

A detailed description is warranted for implementing this theory. For a collection of independent systems in a given state, the rate of transfer from one state to another state is a first-order kinetic process. The rate of transition of this collection from a particular state is proportional amount of systems currently in the state in question. These kinetic rates can be collected to form a system of linear coupled first order differential equations. The methods for solving this type of system are well known (17). The specific method used to analyze organosilicates is outlined below.

The system can be written in matrix form as the following:

$$x'(t) = Ax(t) + b(t) \quad [4.1]$$

After the system is irradiated long enough under constant irradiation ( $b(t)=b(0)$ ), a steady state will be realized and  $x'(t)$  will be zero. At this point  $x$  can be solved easily,

$$x(t = \infty) = -\frac{b}{A} \quad [4.2]$$

If a time between zero and infinity is desired, the system can be solved using the scaling and squaring method via the `expm` function in MATLAB as follows:

$$x(t) = -\frac{b}{A} + \exp(A \cdot t) \cdot C_0 \quad [4.3]$$

where the initial condition is:

$$C_0 = \frac{b}{A} + x_0 \quad [4.4]$$

The matrix elements of  $A$  are found via transition state theory and LZ coupling for motion of a localized exciton and by spontaneous emission for electronic relaxation of an exciton. A model of electronic transfer must be included to capture the experimental result that extremely long range energy transfer does not occur. LZ rates are used because ions involved in this reaction are heavy enough to be treated classically, the implementation of LZ theory is simple, and LZ theory is robust. All coupling from interactions included in the Hamiltonian are captured.

The method of Eyring (9) can be used to find the probability of the system being at the transition point:

$$P(Q_i^{saddle}) = \frac{g_{transition} \prod 2\pi \frac{kT/h}{\sqrt{(\lambda_j/\bar{m}_j)}} \sqrt{(2\pi m_{reduced} kT/h^2)}}{g_{basin} \prod \left( 2\pi \frac{kT/h}{\sqrt{(\lambda_k/\bar{m}_k)}} \right)} \times \exp\left(\frac{-(E_{transition} - E_{basin})}{kT}\right) \quad [4.5]$$

Here  $g_{transition}$  is the electronic degeneracy at the transition state;  $g_{basin}$  is the electronic degeneracy in a basin;  $\lambda/m$  are the eigenvalues for each eigenvector of the mass weighted Hessians at the transition point (numerator) and at the bottom of the basin (denominator); and  $m_{reduced}$  is a mass associated with the configurational change along the minimum energy pathway through the transition point. Our model, being a cluster excised from a bulk system, is constrained rotationally and translationally and has no rotational or translational phase space available. It is assumed that the rotational and translational phase space available to a bulk system are the same at a transition state and in a basin and would thus cancel resulting in the above expression. A result of calculation is that the electronic degeneracy,  $g$ , is 1 at the basin and at the saddle point.

The average velocity is found via the formula given by Eyring. (9) However, when normalizing we integrate from 0 to infinity instead of negative infinity to infinity, because we

are finding the average forward velocity through the saddle point, not the average velocity. Also, we weight the velocity by the LZ chance of diabatic transition as the system passes through an avoided crossing, because we expect the coupling to be weak enough and the ionic motion to be fast enough that the system will not behave adiabatically through the region of coupling.

The chance of diabatic transition is the following (11):

$$P_{diabatic\ transition} \left( H_{12}, \frac{dE}{dt} \right) = 1 - \exp \left( \frac{-2\pi |H_{12}|^2}{\hbar \frac{dE_{12}}{dq} \frac{dq}{dt}} \right) \quad [4.6]$$

The term  $dE/dt$  is expanded via the chain rule to find the average velocity of successful crossing:

$$\bar{p}/m = \frac{\int dp \frac{p}{m} \left[ \exp \left( \frac{-p^2}{2mkT} \right) \left( 1 - \exp \left( \frac{-2\pi |H_{12}|^2}{\hbar \frac{dE_{12}}{dq} \frac{dq}{dt}} \right) \right) \right]}{\int dp \left[ \exp \left( \frac{-p^2}{2mkT} \right) \right]} \quad [4.7A]$$

$$\bar{p}/m = \frac{\int dp \frac{p}{m} \left[ \exp \left( \frac{-p^2}{2mkT} \right) \left( 1 - \exp \left( \frac{-2\pi |H_{12}|^2}{\hbar \nabla E_{12} \cdot \xi \frac{p}{m}} \right) \right) \right]}{\int dp \left[ \exp \left( \frac{-p^2}{2mkT} \right) \right]} \quad [4.7B]$$

$$\bar{p}/m = \frac{\int dp \frac{p}{m} \left[ \exp \left( \frac{-p^2}{2mkT} \right) \left( 1 - \exp \left( \frac{-2\pi |H_{12}|^2 \frac{2m}{p}}{\hbar \nabla E_{12} \cdot \xi} \right) \right) \right]}{\int dp \left[ \exp \left( \frac{-p^2}{2mkT} \right) \right]} \quad [4.7C]$$

At this point we check that our model corresponds with LZ theory. At low coupling, the exponential term in the LZ transition weighting included above can be expanded resulting in the following:

$$\bar{p}/m = \frac{\int dp \frac{p}{m} \left[ \exp \left( \frac{-p^2}{2mkT} \right) \left( 1 - \exp \left( \frac{-2\pi |H_{12}|^2 \frac{2m}{p}}{\hbar \nabla E_{12} \cdot \xi} \right) \right) \right]}{\int dp \left[ \exp \left( \frac{-p^2}{2mkT} \right) \right]} \quad [4.8A]$$

$$\bar{p}/m = \frac{\int dp \frac{p}{m} \left[ \exp \left( \frac{-p^2}{2mkT} \right) \left( 1 - 1 + \frac{2\pi |H_{12}|^2 \frac{2m}{p}}{\hbar \nabla E_{12} \cdot \xi} \right) \right]}{\int dp \left[ \exp \left( \frac{-p^2}{2mkT} \right) \right]} \quad [4.8B]$$

$$\bar{p}/m = \frac{\int dp \left[ \exp\left(\frac{-p^2}{2mkT}\right) \right] 2\pi |H_{12}| \frac{2p}{m}}{\int dp \left[ \exp\left(\frac{-p^2}{2mkT}\right) \right] \hbar \nabla E_{12} \cdot \hat{\xi}} \quad [4.8C]$$

$$\bar{p}/m = \frac{2\pi |H_{12}|^2}{\hbar \nabla E_{12} \cdot \hat{\xi}} \quad [4.8D]$$

This is the same as the result for the rate of energy transfer between weakly coupled systems (11). This suggests the above method is the correct way to incorporate spatial electronic transfer into transition state theory.

The reaction rate can be found by multiplying this weighted average velocity by the normalized probability of finding the system at the saddle point:

$$P(Q_i^{saddle}) \frac{p_{diabatictransfer}}{m} = \left(\frac{dP}{dt}\right)_{ij} = \text{diabaticrate} = A_{ij} =$$

$$\frac{\prod 2\pi \frac{kT/h}{\sqrt{(\lambda_j/m_j)}} \sqrt{(2\pi m_{weighted} kT/h^2)}}{\prod 2\pi \frac{kT/h}{\sqrt{(\lambda_k/m_k)}}} \exp\left(\frac{-(E_{saddle} - E_{basin})}{kT}\right) \quad [4.9]$$

$$\times \frac{\int dp \frac{p}{m} \left[ \exp\left(\frac{-p^2}{2mkT}\right) \left( 1 - \exp\left(\frac{-2\pi |H_{12}| \frac{2m}{p}}{\hbar \nabla E_{12} \cdot \hat{\xi}}\right) \right) \right]}{\int dp \left[ \exp\left(\frac{-p^2}{2mkT}\right) \right]}$$

All kinetic rates are found by solving equation [4.9] for forward and reverse reactions with every combination of basins. With these rates the matrix **A** in equations [4.1] and [4.3] is found.

Because we have included the energetic barrier to reaction, we can check for correspondence between our model and that of Marcus. We apply our theory to the self exchange electron transfer reaction ( $A \cdot + A \rightarrow A + A \cdot$ ) assuming electron transfer occurs in the region where the potential is harmonic:

$$P(Q_i^{saddle}) \frac{p_{diabatictransfer}}{m} = \frac{dP}{dt} = \text{diabaticrate} =$$

$$\frac{\sqrt{(2\pi mkT/h^2)}}{\frac{kT}{\hbar \omega_0}} \exp\left(\frac{-(\lambda + \Delta E)^2}{4\lambda} \frac{1}{kT}\right) \quad [4.10]$$

$$\times \frac{\int dp \frac{p}{m} \left[ \exp\left(\frac{-p^2}{2mkT}\right) \left( 1 - \exp\left(\frac{-2\pi |H_{12}| \frac{2m}{p}}{\hbar \nabla E_{12} \cdot \hat{\xi}}\right) \right) \right]}{\int dp \left[ \exp\left(\frac{-p^2}{2mkT}\right) \right]}$$

Where  $\lambda$  depends on the distance between basins in  $\mathbb{R}^{3N}$  space and the energy difference between the bottoms of the two basins. This can be found by solving for the intersection of two displaced parabolas with the same curvature:

$$\lambda = \frac{w_0^2}{m} (d_{basinA} - d_{basinB})^2 \quad [4.11]$$

We now assume low coupling, follow the manipulations shown in equation [4.8], and substitute the energy sweep gradient along the minimum energy pathway  $\nabla E_{12} \cdot \vec{\xi}$  with the energy sweep gradient of two displaced parabolas with the same curvature:

$$P(Q_i^{saddle}) \frac{p_{diabatictransfer}}{m} = \frac{dP}{dt} = \text{diabatic rate} = \frac{\sqrt{(2\pi mkT/\hbar^2)}}{\frac{kT}{\hbar w_0}} \exp\left(\frac{-(\lambda + \Delta E)^2}{4\lambda} \frac{1}{kT}\right) \times \frac{2\pi |H_{12}|^2}{\hbar \left(2\lambda \frac{w_0^2}{m}\right)^{1/2}} \quad [4.12A]$$

$$P(Q_i^{saddle}) \frac{p_{diabatictransfer}}{m} = \frac{dP}{dt} = \text{diabatic rate} = \sqrt{\left(\frac{\pi}{\lambda kT}\right)} \frac{1}{\hbar} \exp\left(\frac{-(\lambda + \Delta E)^2}{4\lambda} \frac{1}{kT}\right) \times |H_{12}|^2 \quad [4.12B]$$

Because the model system is a cluster that is uncoupled from a surrounding medium there is no work or heat transfer into or out of the cluster system. Any change in energy is a result of internal degrees of freedom. Thus  $\Delta E$  equals  $\Delta G$  and correspondence with the result of Marcus at high temperature and low coupling is shown (18). This also suggests that our method incorporates electronic transition correctly.

If the region of coupling is located before the saddle point, then the sweep rate of the diabatic surfaces will be higher. This is accounted for as follows:

$$\bar{p}/m = \frac{\int dp \frac{p}{m} \left[ \exp\left(\frac{-p^2}{2mkT}\right) \left( 1 - \exp\left(\frac{-2\pi |H_{12}|^2 \frac{m_{coupling}}{p_{coupling}(p)}}{\hbar \nabla E_{12} \cdot \vec{\xi}_{mep}}\right) \right) \right]}{\int dp \left[ \exp\left(\frac{-p^2}{2mkT}\right) \right]} \quad [4.13]$$

Where  $p_{coupling}$  is the momentum the system has when passing through the region of coupling and  $m_{coupling}$  is the reduced mass of the system passing through the region of coupling. The value of  $p_{coupling}$  is related to the energy of the saddle point and point of coupling:

$$E_{trans} = E_{coupling} \quad [4.14A]$$

$$\frac{p_{trans}^2}{2 \cdot m_{trans}} + U_{trans} = \frac{p_{coupling}^2}{2 \cdot m_{coupling}} + U_{coupling} \quad [4.14B]$$

$$p_{trans}^2 \cdot \frac{2 \cdot m_{coupling}}{2 \cdot m_{trans}} + U_{trans} \cdot 2 \cdot m_{coupling} = p_{coupling}^2 + U_{coupling} \cdot 2 \cdot m_{coupling} \quad [4.14C]$$

$$p_{trans}^2 \cdot \frac{2 \cdot m_{coupling}}{2 \cdot m_{trans}} + (U_{trans} - U_{coupling}) \cdot 2 \cdot m_{coupling} = p_{coupling}^2 \quad [4.14D]$$

$$\sqrt{p_{trans}^2 \cdot \frac{2 \cdot m_{coupling}}{2 \cdot m_{trans}} + (U_{trans} - U_{coupling}) \cdot 2 \cdot m_{coupling}} = p_{coupling} \quad [4.14E]$$

This is integrated numerically and then incorporated into equation [4.9] for the rate constant.

When coupling is extremely low the term

$$\left( 1 - \exp \left( \frac{-2\pi |H_{12}|^2 \frac{m_{coupling}}{p_{coupling}(p)}}{\hbar \nabla E_{12} \cdot \vec{\xi}_{mep}} \right) \right) \quad [4.15]$$

when evaluated numerically will result in a very small number compared to the value of 1 and the exponential (both approximately equal to 1). These were evaluated using 64 bit floating point precision with 53 binary data bits. When converted to base 10, this produces approximately 16 digits of precision. If the result of the exponential is close to 1 within  $10^{-16}$ , then the numerical value found using equation [4.15] will no longer be reliable. A value of  $10^{-14}$  gives a precision error of 1% which was chosen by us to be acceptable. Thus we chose a low limit of coupling to evaluate numerically (Eq. [4.16]):

$$10^{-14} = \left( 1 - \exp \left( \frac{-2\pi |H_{12}|^2 \frac{m_{coupling}}{p_{coupling}(p)}}{\hbar \nabla E_{12} \cdot \vec{\xi}_{mep}} \right) \right) \quad [4.16A]$$

$$10^{-14} = \frac{-2\pi |H_{12}|^2 \frac{m_{coupling}}{p_{coupling}(p=(\sqrt{2mKT}))}}{\hbar \nabla E_{12} \cdot \vec{\xi}_{mep}} \quad [4.16B]$$

$$10^{-7} \cdot \sqrt{\frac{\hbar \nabla E_{12} \cdot \vec{\xi}_{mep} p_{coupling}(p=(\sqrt{2mKT}))}{2\pi m_{coupling}}} = |H_{12}| \quad [4.16C]$$

If the coupling is below this number, then numerical integrations will no longer be reliable. In this case the weak coupling approximation is used for the velocity through the transition state (Eq [4.17]).

$$\bar{p}/m = \frac{\int dp \frac{p}{m} \left[ \exp\left(\frac{-p^2}{2mkT}\right) \left( \frac{2\pi |H_{12}|^2 \frac{m \text{ coupling}}{p \text{ coupling}(p)}}{\hbar V E_{12} \xi_{mep}} \right) \right]}{\int dp \left[ \exp\left(\frac{-p^2}{2mkT}\right) \right]} \quad [4.17]$$

This is analogous to equation [4.8B].

The rates calculated without approximation([4.9] with the integral shown in [4.13]), the low coupling approximation with coupling before the saddle point [4.17], the LZ rate [4.8D], and the original result of Eyring are all presented below as a function of coupling. This demonstrates the correct limiting behavior of our calculations for high and low coupling.

#### 4.4. Methods

Calculations employed the NWChem 6.0 code using density functional theory (DFT) with Pople basis sets 6-31+g\*, 6-311+g\*, 6-31++g\*, 6-311++g\*, Dunning sets aug-cc-pVDZ and aug-cc-pVTZ. All NWChem defaults were used with the exception that the Dunning sets included the “spherical” basis set option. We used the “spherical” option when using correlation consistent basis sets because these basis sets were designed using spherical harmonics. (30) The B3LYP hybrid exchange-correlation approximation was used to capture effects of exchange and correlation. The convergence criteria finding electronic structure was  $10^{-6}$  Hartree,  $10^{-5}$  RMS for the density matrix and  $10^{-4}$  DIIS error vector. Structural optimization was performed using the NWChem Driver module with default options using Cartesian coordinates. The Quasi Newton-Raphson algorithm was used to find the minimum geometries. Convergence criteria for the potential surface minimization is a gradient of less than  $4.5 \cdot 10^{-4}$  Hartree/Angstrom for each coordinate and  $3 \cdot 10^{-4}$  RMS in all coordinates and a step of less than  $1.8 \cdot 10^{-3}$  Angstroms in each coordinate and  $1.2 \cdot 10^{-3}$  RMS in all coordinates. For NEB analysis, we examined the molecular orbitals to ensure that they did not converge to an excited state. We performed Mulliken analysis to determine where the exciton was localized in order to determine diabatic energy levels and self trapping (19).

The glass cluster calculations followed the procedure of previous studies of excitons in silica clusters extracted from bulk configurations. The initial ring structure was extracted from an extended simulated glass we generated by minimizing the geometry of a large cluster. This simplified system was comprised of four silicon atoms bridged by four oxygen atoms and where each silicon atom has two additional bonds to hydroxyl groups (Figure 4.1 E). The hydroxyl groups were fixed in position with extended hydroxyl bond lengths that served the purpose of mimicking the SiO bond in terms of electronic structure so as not to lead to self-trapping or breaking of the bond that would otherwise occur in the presence of a triplet excitation (5).

The ring ground state structure was then optimized while holding all but one of the hydroxyl groups' bond lengths and positions fixed in order to simulate the charge distribution of the SiO bond in bulk silica (7). Excitonic states were modeled by minimizing the geometry with a triplet electronic configuration. Based on chemical intuition, we selected substituents to model a bare silica surface (hydroxyl), a reduced silica surface (hydride),  $\pi$  conjugated dyes (vinyl, allyl, and phenyl groups) and organo groups without  $\pi$  conjugation (methyl and methoxyl groups). For the calculations with the dyes, the unconstrained hydroxyl group was replaced with the aforementioned substituents, then optimized in the ground state holding only the hydroxyl groups fixed. These substituted systems were then optimized again with a triplet electronic state to model exciton self trapping.

The structure of a self-trapped exciton within the silica structure was found using the methyl substituted system. The energy of the system was first minimized in the ground singlet state. The resulting lowest energy geometry was then used as a starting point to find the minimum triplet state geometry. The structure that was determined, described below, was similar to previous work (5) and was used to confirm self-trapping of the exciton in the silica side of the substituted systems. For each of these substituted systems, the triplet state was introduced by solving for the triplet electronic structure instead of the singlet structure, and allowed to relax by repeating the geometry minimization on the triplet energy surface.

For sesquioxane, the initial geometry was found by minimizing the ground state geometry with eight hydroxyl substituents. An excitonic state was then modeled by calculating the triplet multiplicity electronic state at the singlet minimum geometry. The geometry on the

triplet energy surface was then relaxed to simulate self trapping. Once the minimum triplet geometry was found, the singlet state was calculated to find the vertical relaxation from the minimum energy geometry triplet state to the singlet state.

Additionally, vertical excitations from the singlet to triplet states were found via TDDFT. The singlet electronic density was found as described above using the 6-31+g\* basis set. This density was used to find the energy of the lowest six electronic singlet and triplet states at the singlet minimum geometry. The difference between the lowest singlet and lowest triplet state found via TDDFT, which was found using default TDDFT settings in NWChem, was determined to be the TDDFT vertical excitation.

To model the propagation of probability measure as a function of time when verifying the LZ equation, we used the Crank-Nicholson method to evaluate the Hamiltonian propagator. (20) The initial state of the system had unity probability for the state being in the initial diabatic surface. We used an energy sweep rate of 3 Joules per meter (taken from a converged trajectory), a velocity of 1000 meters per second, and Brownian motion corresponding to an RMS velocity of 1000 meters per second to generate our results.

When evaluating equation [4.9] for our exchange rate calculations, we assumed all vibrational modes in the transition state are also present in the basin. Thus these cancel out in the prefactor. So equation [4.9] can be modified:

$$P(Q_i^{saddle}) \frac{p^{diabatictransfer}}{m} = \left(\frac{dp}{dt}\right)_{ij} = \text{diabaticrate} = A_{ij} =$$

$$\frac{\sqrt{(2\pi m_{weighted} kT/h^2)}}{2\pi \frac{kT/h}{\sqrt{(\lambda_k/m_k)}}} \exp\left(\frac{-(E_{saddle} - E_{basin})}{kT}\right)$$

$$\times \frac{\int dp \frac{p}{m} \left[ \exp\left(\frac{-p^2}{2mkT}\right) \left( 1 - \exp\left(\frac{-2\pi |H_{12}|^2 m}{\hbar \nabla E_{12} \cdot \xi p}\right) \right) \right]}{\int dp \left[ \exp\left(\frac{-p^2}{2mkT}\right) \right]} \quad [4.18]$$

The prefactor becomes a product of the vibrational mode that is lost at the saddle point by the translational phase space. To evaluate  $2\pi \frac{kT/h}{\sqrt{(\lambda_k/m_k)}}$ , we used the inner product of the reaction coordinate vector in the vicinity of the initial basin with the hessian eigenvectors to generate a weighted average of the hessian eigenvalues in the reaction coordinate direction. This generated a weighted average of vibrational frequencies, with those in the direction of the MEP weighted higher than those perpendicular to the MEP. This avoided

excessive error that would result from multiplying many vibrational frequencies together for the basin and saddle point.

We found values of coupling by taking the difference in energies of the adiabatic surfaces at their closest approach. The sweep rate was found by assuming that the diabatic surfaces are very close to the adiabatic surfaces in energy in the neighboring data points, and that the sweep rate through the intersection of diabatic surfaces is equal to the average sweep rate found from neighboring data:

$$P(Q_i^{saddle}) \frac{p_{diabatic\ transfer}}{m} = \left(\frac{dP}{dt}\right)_{ij} = \text{diabaticrate} = A_{ij} =$$

$$\nu \sqrt{\left(\frac{2\pi m_{weighted}}{kT}\right)} \exp\left(\frac{-(E_{saddle} - E_{basin})}{kT}\right)$$

$$\times \frac{\int dp \frac{p}{m} \left[ \exp\left(\frac{-p^2}{2mkT}\right) \left( 1 - \exp\left( \frac{-2\pi |Adiabatic_{upper} - Adiabatic_{lower}| \frac{2m}{p}}{\hbar \left( \frac{Adiabatic_{upper} - Adiabatic_{lower}}{\Delta q} - \frac{Adiabatic_{lower} - Adiabatic_{upper}}{\Delta q} \right)} \right) \right] \right]}{\int dp \left[ \exp\left(\frac{-p^2}{2mkT}\right) \right]} \quad [4.19]$$

Here  $\nu$  is the weighted vibrational frequency in the direction of the MEP,  $m_{weighted}$  is the weighted mass of the system through the saddle point, the minus and plus superscript represent data taken from beads before and after the bead where coupling occurs, respectively, and  $q$  is the distance between the beads before and after the bead where coupling occurs.

Because the region of coupling does not fall at the saddle point for our organosilica system, the velocity through the region of coupling will not be constant. To verify the validity of the LZ approximation which assumes constant velocity through the region of coupling, the time dependant Schrodinger equation was solved using parameters from a converged trajectory of our system. Sweep profiles used corresponded to constant velocity, a parabolically time dependent velocity consistent with the loss of momentum as the system passes through the region of coupling, and a constant velocity with added Brownian noise consistent with an RMS velocity equal to the sweep rate.

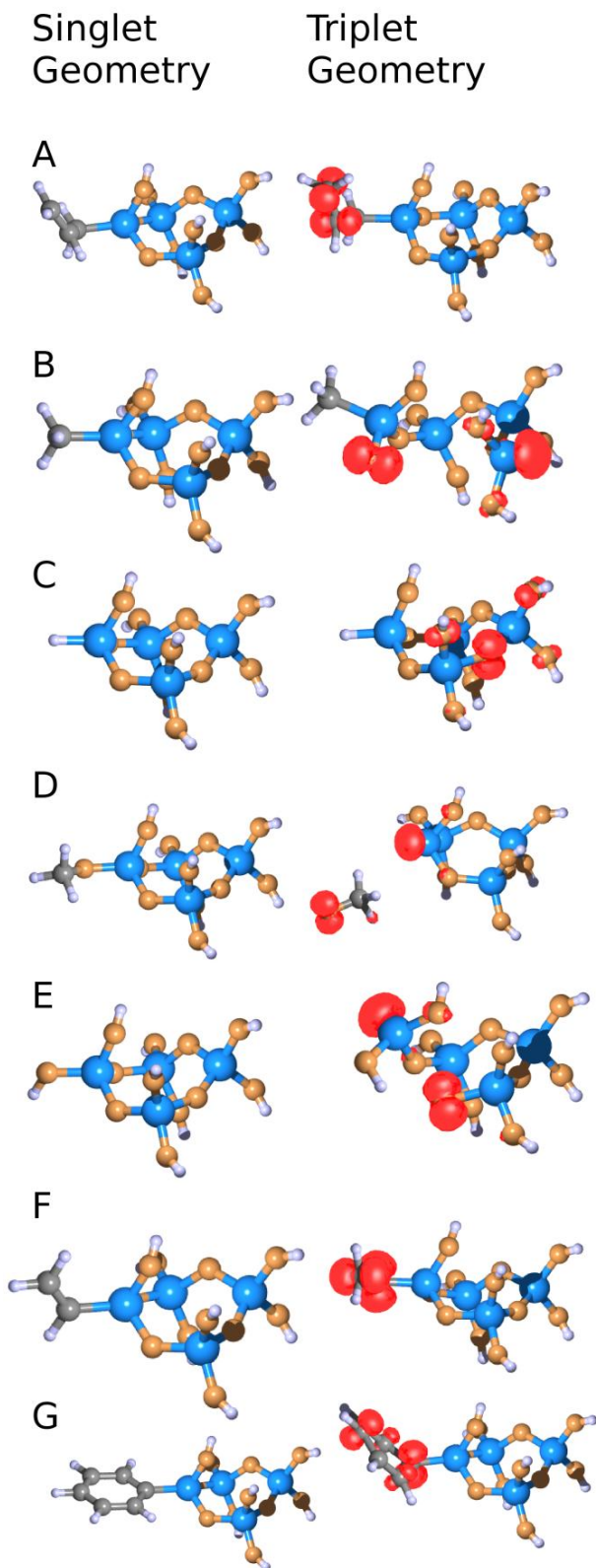


Figure 4.1: Model of excess spin density  
Blue spheres are silicon, orange spheres are oxygen, grey spheres are carbon and white spheres are hydrogen. The red mesh is an isosurface showing regions of excess alpha spin density. The left side shows the minimum energy singlet geometry while the right side shows the minimum energy triplet geometry and excess spin density after the system is allowed to relax. From the top the substituents are as follows: allyl, methyl, hydride, methoxyl, hydroxide, vinyl and phenyl.

To compare our ELZ method to the Eyring and LZ methods, we used parameters from the converged NEB trajectory of our allylic substituted organosilica system. The coupling was set to 0.0232 eV, the sweep rate was 0.347 eV per Angstrom, the vibrational frequency along the direction of reaction was  $1.34 \cdot 10^{14}$  Hz, the reduced mass of the ions moving along the reaction coordinate was  $6.83 \cdot 10^{-27}$  kg, the energy of the exciton localized in glass was 2.77 eV, the energy of the exciton localized in the allyl group was 0 eV, and the saddle point energy was 3.52 eV. Velocity was integrated from the minimum possible based on equation [4.14 E] to infinity. Other parameters that were used are indicated on the graphs.

The localization of energy for assigning diabatic surfaces in Figure 4.6 was found via Mulliken analysis (19). The simulation of emission spectra as a function of time and quantum yield simulations using equations 4.2 and 4.3 were performed via MATLAB v2011a (Mathworks, Inc., Natick, MA). Equation 4.2

was solved implicitly using the backslash operator in MATLAB. The matrix exponential in equation 4.3 was calculated via the scaling and squaring method as implemented in MATLAB's `expm` function.

#### 4.5. Results

The results of exciton localization are summarized in Table 4.2, while visualization of localization is shown in Figure 4.1. The excitation energy is lower in systems where the exciton localizes in the dye (Figure 4.1 A, F, G, Table 4.2 rows 1, 6, 7), while it is higher in systems where the exciton localizes in the glass or is delocalized (Figure 4.1 B, C, D, E, Table 4.2 rows 2, 3, 4, 5). Also, the relaxation energy to the minimum energy geometry is lower when the exciton is delocalized throughout the cluster (Figure 4.1 C), and higher for systems where it localizes (Figure 4.1 A, B, D, E, F, G). The simulated excitons were found to distort bonds and self trap all systems except for the hydride system. Self-trapping of the exciton within the silica structure occurred directly for the case where a methyl group was substituted and the OH groups were structurally constrained to prevent the excitation from moving onto those constituents (Figure 4.1 B). This self-trapped exciton (STE) lead to a stretched Si-O bond with the hole centered on the oxygen atom and the excess electron on the silicon.

To understand if self-trapping can occur on the silica when exciton supporting dyes (allyl, vinyl, phenyl substituents) are present, the minimum energy triplet nuclear geometry of the unsubstituted structure (Figure 4.1 C) was used as the starting configuration for our model of self trapping in these systems. In these cases, the exciton remained in the silica network despite having higher energy than that of an exciton trapping within the dyes. This is indicative of a metastable state where there is an energetic barrier to exciton transfer from the glass to the exciton supporting dye.

We chose to study the stability of this state by using the allyl-silica system as a model, because this system was the most tractable exciton supporting system that we modeled. The path for the migration of the ions perturbed by the exciton was determined using the nudge-elastic band (NEB) method (Figures 4.6 & 4.7). The NEB potential energy surface analysis demonstrates that there exists an energy barrier for exciton transfer from a state localized in the glass to a state localized in the exciton supporting dye. Its existence is important because it shows that excitations do not necessarily fall directly into bonded

System	Singlet to triplet vertical excitation energy (eV)	Triplet to singlet vertical excitation (eV)	Total relaxation energy (excited and ground state)	Localization
Allyl substitution	4.28	1.02	3.26	Localized on allyl group
Methyl substitution	7.26	5.11	2.15	Localized on cluster
Hydride substitution	7.34	6.98	0.36	Delocalized
Methoxide substitution	7.22	3.92	3.30	Localized on methoxide group
Hydroxide substitution	7.20	4.44	2.76	Localized on glass cluster
Vinyl substitution	4.26	1.25	3.01	Localized on vinyl group
Phenyl substitution	4.68	0.65	4.04	Localized on phenyl group

Table 4. 1: Transition energies and localization for various surface groups

organic systems. We expect the same behavior for the vinyl and phenyl substituted systems based on our simulation of exciton self trapping within the glass based on the minimum triplet geometry of the unsubstituted system used as the initial geometry of the glass portion of our organosilica model.

To verify basis set completeness, we examined the excitation and relaxation energies of these systems with various basis sets. There is reasonable agreement between double and triple zeta basis sets (Tables 4.4, 4.5, 4.6, 4.7, 4.8). Our results obtained with additional diffuse and polarization functions on hydrogen are consistent with results found without these additional basis functions (Table 4.3).

Vertical excitations via TDDFT and DFT	TDDFT singlet excitation (eV)	TDDFT first triplet excitation (eV)	DFT ground state triplet – DFT ground state singlet (eV)
vinyl	6.43	3.93	4.25
allyl	5.54	3.99	4.29
butadienyl	5.37	2.72	3.11
phenyl	5.25	3.71	4.19
8 allyl groups	6.35	3.92	4.25
8 vinyl groups	5.86	3.98	4.28

Table 4.2: Vertical excitations found via TDDFT and DFT, 6-31+g\* basis sets.

Based on our result that excitons can localize in the silica portion of an organosilica system, we examined excitation energies, nuclear relaxation energy (phonon coupling) and relaxation energies of exciton supporting dyes (Table 4.2). We chose systems that had varying levels of  $\pi$  conjugation to observe the effect of  $\pi$  conjugation on exciton dynamics.

To validate our method for analyzing low lying excitonic states, we compared the difference between the ground state triplet and ground state singlet states found via DFT with the first triplet and first singlet excitation found via TDDFT (Table 4.2). The singlet excitation found via TDDFT is much higher than the triplet excitation found via TDDFT. This is evidence that our method of using the triplet ground state to model low energy excitons is indeed valid. Also, the TDDFT energy for triplet excitations is lower than the triplet ground state found via DFT due to the more accurate modeling of exchange with TDDFT. The reasonable agreement between TDDFT triplet excitation with the difference between the DFT ground state triplet and DFT ground state singlet validates our approach of using the DFT triplet can be used to model low energy excitons.

The calculated lower excitation energy with multiple exciton acceptors (Table 4.2 row 5 & 6) suggests that coupling between excitonic states extends through the silica network. Each of the systems with exciton supporting dyes (allyl, vinyl, phenyl, butadienyl) has roughly comparable excitation energies (Table 4.3). The transition energies are

significantly smaller than what would be expected for isolated dyes given the level of conjugation of the  $\pi$  bond network. (31)

The nuclear relaxation energies of the vinyl, allyl, butadienyl and phenyl systems were determined by minimizing the nuclear geometry from the initial excited state geometry to the lowest energy excited state geometry. The energy lost is diffused as phonons into the surrounding material, so this relaxation energy gave a measure for phonon coupling during exciton trapping into the dye. As the dye becomes larger, nuclear motion is less constrained, so the relaxation energy became larger. Because the Pople basis set does not give reasonable results for all dyes, we used Dunning basis set for our exchange rate calculations.

We calculated the DFT vertical excitation energy between the ground state triplet and ground state singlet at the ground state triplet minimum geometry (Table 4.5). The vertical excitation is smaller with greater  $\pi$  conjugation, which is consistent with UV spectroscopy. This serves as verification that we are correctly modeling low-lying excitons.

To test the validity of constraining the

DFT vertical excitation (eV)	6-31+g*	6-311+g*	aug-cc-pVDZ	aug-cc-pVTZ
vinyl	4.25	4.30	4.25	4.33
allyl	4.29	4.34	4.27	4.35
butadienyl	3.11	3.16	3.11	3.18
phenyl	4.19	4.21	4.17	4.23

Table 4.3: DFT vertical excitation energies at singlet minimum geometry.

DFT relaxation energy (eV)	6-31+g*	6-311+g*	aug-cc-pVDZ	aug-cc-pVTZ
Vinyl	0.02	0.02	0.02	n/a
Allyl	-1.12	-1.11	0.05	n/a
Butadyenyl	1.79	1.79	1.79	1.81
Phenyl	3.16	3.08	3.15	3.17

Table 4.4: DFT relaxation energies to minimum triplet geometry

DFT vertical excitation (eV)	6-31+g*	6-311+g*	aug-cc-pVDZ	aug-cc-pVTZ
vinyl	1.63	1.66	1.63	1.69
allyl	1.57	1.60	1.56	1.59
butadienyl	0.67	0.69	0.68	0.68
phenyl	0.51	0.57	0.51	0.51

Table 4.5: DFT vertical excitation energies at triplet minimum geometry

surrounding hydroxyl groups of the silica cluster, we simulated vertical excitation energies with eight unconstrained substituents (Table 4.6). The agreement between the vertical excitation energy for eight hydroxide, eight methyl and eight methoxide substituents suggested the exciton localizes within the silicon oxide if there are no exciton supporting dyes chemisorbed to the SSOS system.

These excitation energies for systems without exciton supporting dyes (hydriyl, hydroxyl, methyl, methoxyl, Table 4.6) agreed with the excitation energy found for a silica cluster with constrained surface hydroxyl groups and an unconstrained substituent that does not support exciton self trapping (hydriyl, hydroxyl, methyl, methoxyl, Table 4.1). All of our simulations showed the vertical singlet to triplet excitation of the silica is less than the 11.8 eV band gap for bulk silica. This is consistent with excitation to a low lying state within the band gap of silica.

DFT vertical excitation	6-31+g*	6-311+g*
hydride	7.56	7.56
hydroxide	6.90	6.92
methyl	6.96	7.00
methoxide	6.95	6.96
vinyl	4.25	4.30
allyl	4.28	4.33

Table 4.6: DFT vertical excitation with eight substituents.

Since all  $\pi$  conjugated systems are found to support excitons, we examined allyl and butadienyl groups to determine exciton transfer rates. These models for a  $\pi$  conjugated energy acceptor were tractably modeled with a practical amount of time and computational resources. By studying dyes with different levels of  $\pi$  conjugation, we extrapolated to highly  $\pi$  bond conjugated systems typical of exciton acceptors.

It is not clear which method should be used to model the kinetics of exciton transfer between the glass excitonic states (Figure 4.1 B,C, E) and the dye localized states (Figure 4.1 A, F, G) found in our initial studies. Eyring theory does not capture energy transfer rates, while LZ theory does not capture the energy barrier we have observed. Furthermore, it is not clear if LZ theory is valid for our system because the region of coupling does not coincide with the saddle point (see Figure 4.6). We proceeded by verifying that our hybrid ELZ theory is consistent with Eyring and LZ theories, and that it can be applied to exciton transfer between localized states in organosilica systems with exciton supporting dyes.

To explore the level of error introduced by assuming that coupling occurs at the saddle point, we simulated the exchange rates when the region coupling occurs at various places before the saddle point with moderate coupling (Figure 4.2 B) and weak coupling (Figure

LZ transition probability	Landau Zener Approximation	Linear sweep	Parabolic sweep	Linear sweep + Brownian noise
Moderate coupling	0.3791	0.3790	0.3789	0.2524
Weak coupling	$4.7663 \cdot 10^{-3}$	$4.7447 \cdot 10^{-3}$	$4.7668 \cdot 10^{-3}$	$4.6762 \cdot 10^{-3}$

Table 4.7: LZ transition probabilities with various sweep profiles.

4.2 C). The results showed that the assumption that coupling occurs at the saddle point quickly introduced an order of magnitude error in exchange rates (Figure 4.2 B,C). As coupling decreased, this error was exacerbated (Figure 4.2 D,E). Figure 4.2 D shows the simulated exchange rate with the region of coupling before the saddle point for various values of coupling. At the limit of high coupling, this energy deficit becomes less relevant. This result is intuitive as the system will remain on the lower adiabatic surface throughout the course of reaction in the limit of high coupling. The error introduced by assuming the region of coupling falls on the saddle point leveled off at approximately an order of magnitude at the low coupling limit as shown by the ratio of exchange rate at moderate coupling and low coupling (Figure 4.2 E). This error will increase as the energy difference between the region of coupling and the saddle point increases. This indicates that assuming the transition occurs at the saddle point is not correct and will not give accurate results.

Because the region of coupling falls before the saddle point, the nucleons will slow down as they pass through the region of coupling. Thus, the sweep rate is not constant, which is an assumption underlying the derivation of LZ theory. Also, our simulations do not sweep from the negative and positive time limits; our adiabatic levels were constrained to the region within the reaction coordinate limits which also violates an assumption of LZ theory. Thus we tested the accuracy of LZ theory when the assumptions that sweep rate is constant and that indefinite energy sweeps are not valid.

Based on the results of our simulations with the value obtained using the LZ approximation, the linear sweep, parabolic sweep and Brownian motion sweep are all in reasonable agreement with the known LZ approximation (Figure 4.7).

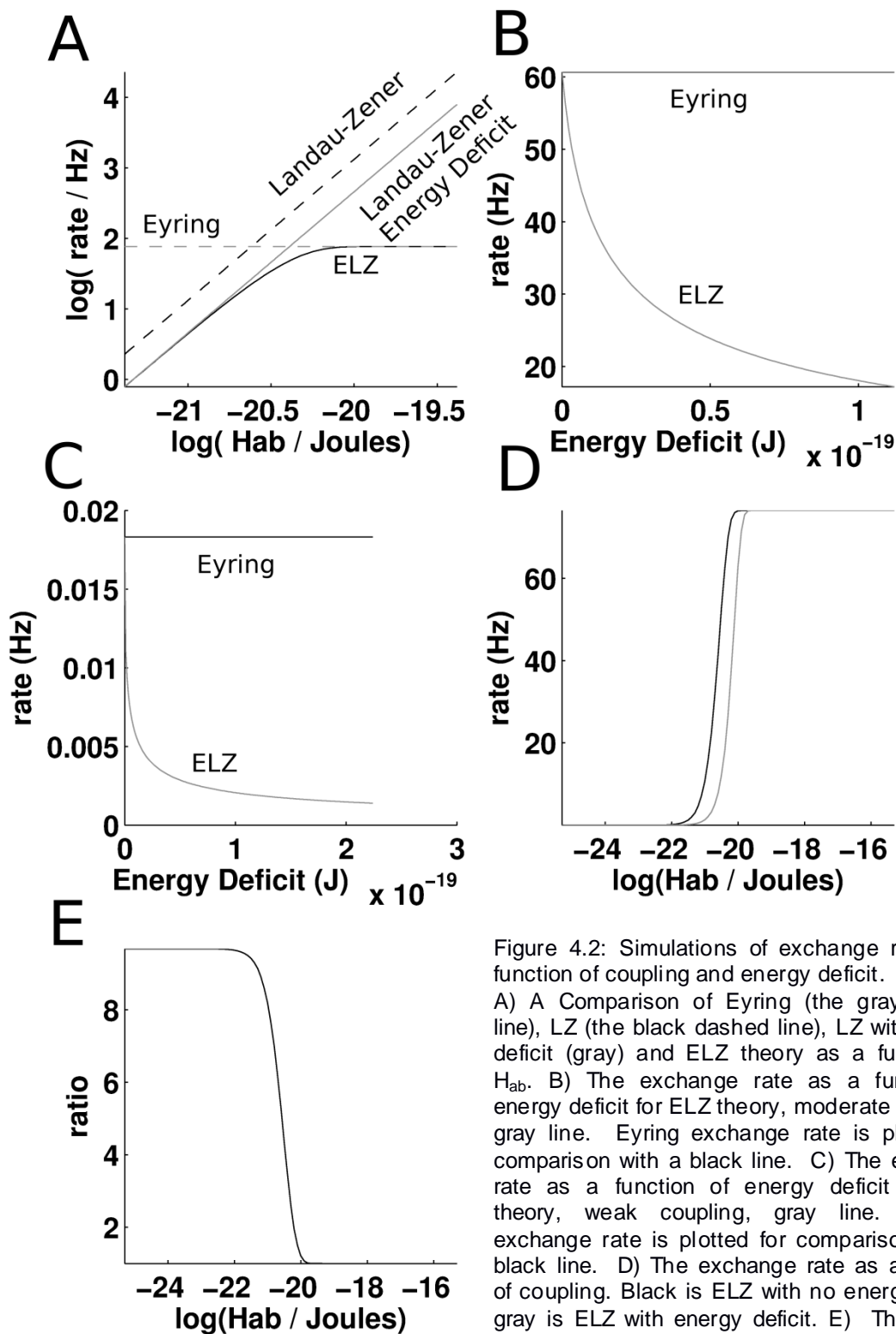


Figure 4.2: Simulations of exchange rate as a function of coupling and energy deficit.

A) A Comparison of Eyring (the gray dashed line), LZ (the black dashed line), LZ with energy deficit (gray) and ELZ theory as a function of  $H_{\text{ab}}$ . B) The exchange rate as a function of energy deficit for ELZ theory, moderate coupling, gray line. Eyring exchange rate is plotted for comparison with a black line. C) The exchange rate as a function of energy deficit for ELZ theory, weak coupling, gray line. Eyring exchange rate is plotted for comparison with a black line. D) The exchange rate as a function of coupling. Black is ELZ with no energy deficit, gray is ELZ with energy deficit. E) The ratio of ELZ with and without energy deficit with an energy deficit from a converged NEB trajectory.

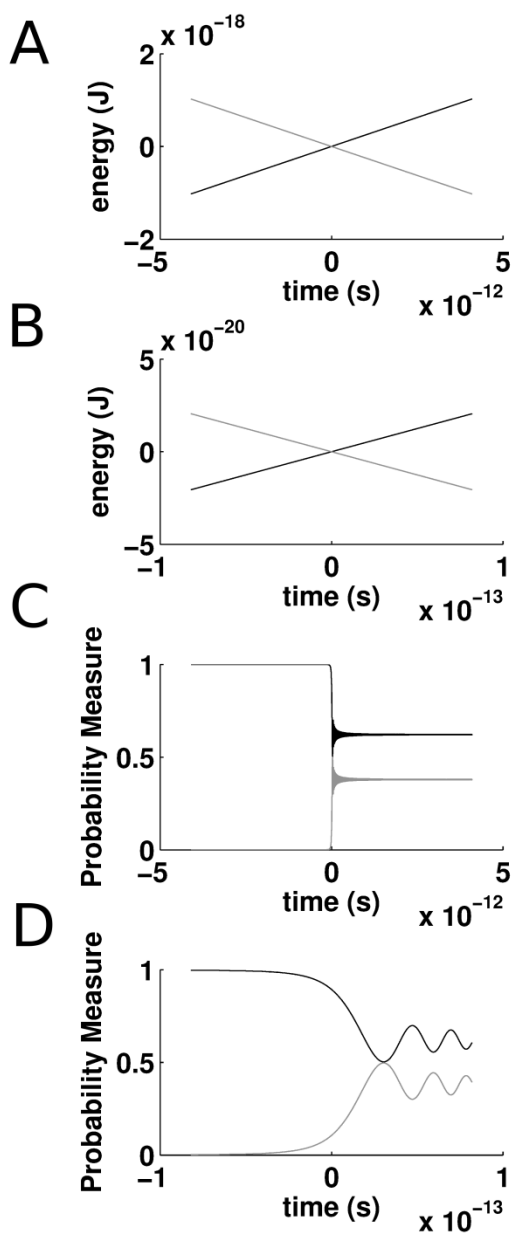


Figure 4.3: Probability measure as a function of time with linear sweep rate. A) Diabatic energy levels vs. time, with state A as black and state B as grey. B) Detail of top. C) Transition probability vs. time. D) detail of 2<sup>nd</sup> from bottom.

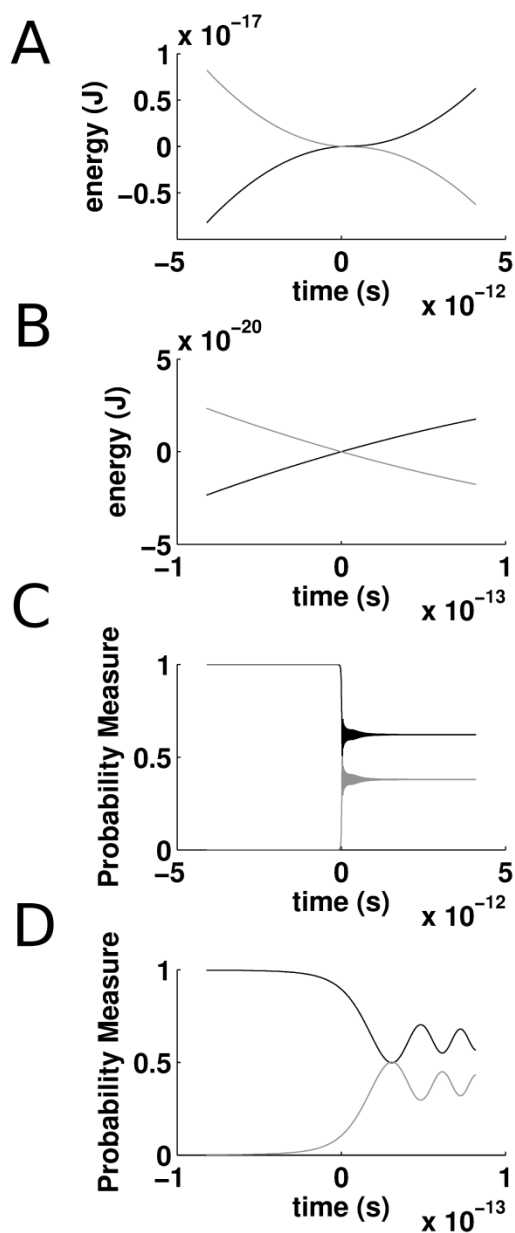


Figure 4.4: Probability measure as a function of time with parabolic sweep rate. A) Diabatic energy levels vs. time, with state A as black and state B as grey. B) Detail of top. C) Transition probability vs. time. D) detail of 2<sup>nd</sup> from bottom.

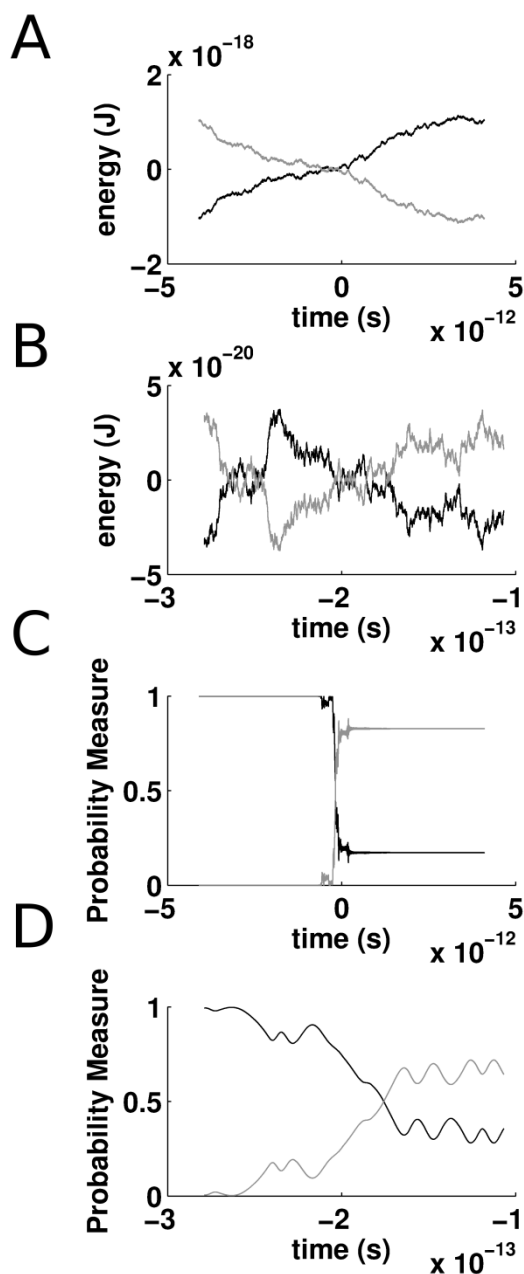


Figure 4.5: Probability measure as a function of time with linear sweep rate with added Brownian noise.

A) Diabatic energy levels vs. time, with state A as black and state B as grey. B) Detail of top. C) Transition probability vs. time. D) detail of  $2^{\text{nd}}$  from bottom.

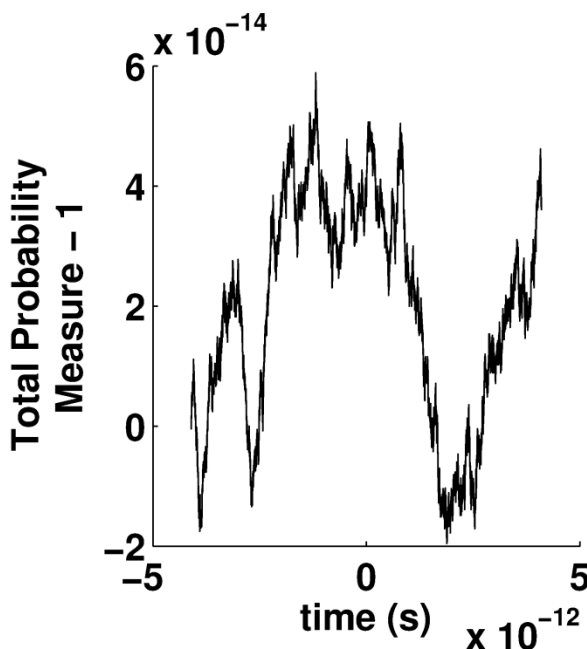


Figure 4.6: Total deviation of probability measure from unity.

Using the Crank-Nicholson method ensures probability measure is well conserved to within 60 parts per quadrillion.

At a reasonable velocity (near the RMS velocity of the system along the MEP at  $T=300$ ) and energy gradient for our system, the parabolic sweep is very similar to the linear sweep in the region of coupling (Figure 4.3, 4.4). The sweep of the diabatic surfaces from initial to final energy (Figure 4.3 middle and Figure 4.4 middle) show that even at finite limits for energy sweep the probability measure matches well with that found via the LZ formula. The detail of the region of coupling (Figure 4.3 bottom and Figure 4.4 bottom) shows that the transition occurs in a region small enough that the

LZ transition probability	Landau Zener Approximation	Linear sweep	Parabolic sweep	Linear sweep + Brownian noise
Moderate coupling	0.3791	0.3790	0.3789	0.2524
Weak coupling	$4.7663 \cdot 10^{-9}$	$4.7447 \cdot 10^{-9}$	$4.7668 \cdot 10^{-9}$	$4.6762 \cdot 10^{-9}$

Table 4.8: LZ transition probabilities with various sweep profiles.

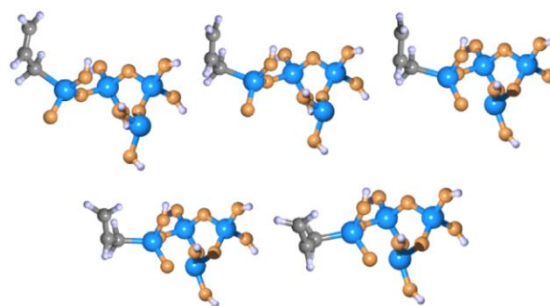
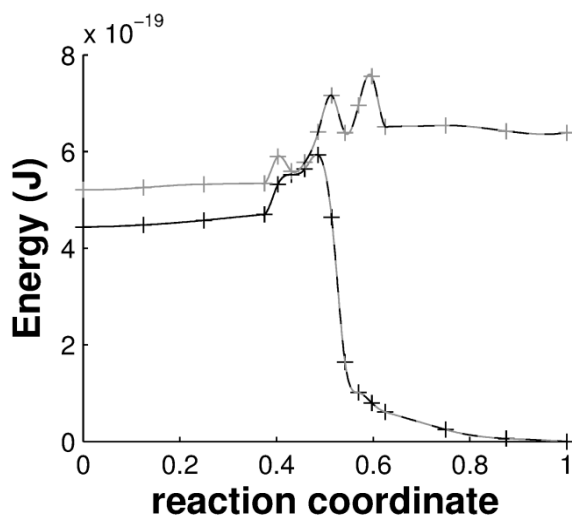


Figure 4.7: Snapshots from the minimum energy pathway for a silica-allyl system. The energy transfers from the defect in the silica cluster to the exciton supporting allylic group.

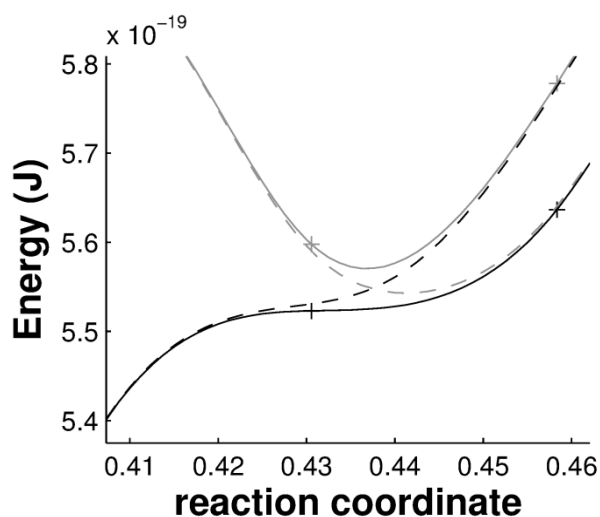


Figure 4.8: Diabatic and adiabatic energy levels for the silica-allyl dye system.

The solid black line is the lower adiabatic surface, the solid gray line is the upper adiabatic surface, the dashed black line is the diabatic surface for an exciton localized in the glass, dotted gray line is the diabatic surface for an exciton localized in the dye. Figure B) is a detail of the region of coupling.

parabolic sweep is very close to a linear sweep.

For our system, it is not clear that the system will pass through the region of coupling with a given velocity at a single time. To test the effects of the system drifting through the region of coupling, we added additional Brownian motion to the linearly sweeping diabatic surfaces (Figure 4.5). This resulted in a deviation from the LZ approximation (Table 4.7). The added velocity from Brownian motion increased the sweep rate. This was balanced by the multiple intersections of diabatic surfaces as a result of the added Brownian motion (Figure 4.5).

Butadiene dye (Hz)	Butadiene pucker	Butadiene far	Dye loc
Butadiene pucker	n/a	$2.8165 \cdot 10^{-35}$	$3.9924 \cdot 10^{11}$
Butadiene far	$4.6114 \cdot 10^{-35}$	n/a	$5.2690 \cdot 10^7$
Dye loc	$3.8325 \cdot 10^{-37}$	$4.9344 \cdot 10^{-42}$	n/a

Table 4.10: Exchange rate constants for butadienyl-silica system. Exchange rates are between basins for excitons localized on the butadienyl group, near the butadienyl group, and far from the organic group.

Allyl dye (Hz)	allyl pucker	allyl far	Dye loc
allyl pucker	n/a	$4.1463 \cdot 10^{-162}$	$1.01 \cdot 10^{-2}$
allyl far	$3.3678 \cdot 10^{-166}$	n/a	$4.19238 \cdot 10^1$
Dye loc	$2.433 \cdot 10^{-49}$	$2.7150 \cdot 10^{-43}$	n/a

Table 4.9: Exchange rate constants for allyl-butadienyl system. Exchange rates are between basins for excitons localized on the butadienyl group, near the butadienyl group, and far from the organic group.

bond of the allyl group, while the intermediate snapshots show the configuration of nucleons as they move through the minimum energy pathway linking the two. The critical features governing the kinetic rate of exciton exchange include the activation energy (Figure 4.7 A), the coupling (half the difference between adiabatic surfaces at closest approach), sweeping of diabatic surfaces, (Figure 4.7B) and the energy deficit between these two regions. The relevant data from these adiabatic surfaces was used to calculate the exchange rate from initial to final state. We repeated this analysis between each basin for an exciton localized at the opposite side of the cluster from the dye, near the dye, and on the dye for a system with an allyl group and a system with a butadienyl group.

Without  $\pi$  conjugation, the exchange rate for an exciton localized in the cluster to the dye is much lower than with  $\pi$  conjugation (Tables 4.9, 4.10).

A simulation of quantum yield as a function of exciton decay rate was performed using equation [4.2] assuming the exciton randomly localizes in the near and far basin. Even at fairly low decay rates, the quantum yield of the allylic substituent quickly fell to zero, while the butadienyl system maintained a high quantum yield even at high decay rates,

The minimum energy pathway energy as function of reaction coordinate for the silica-allyl system has all the salient features relevant to our model (Figure 4.7). The initial snapshot is that of an exciton localized in the glass, and the final snapshot is that of the exciton localized in the  $\pi$

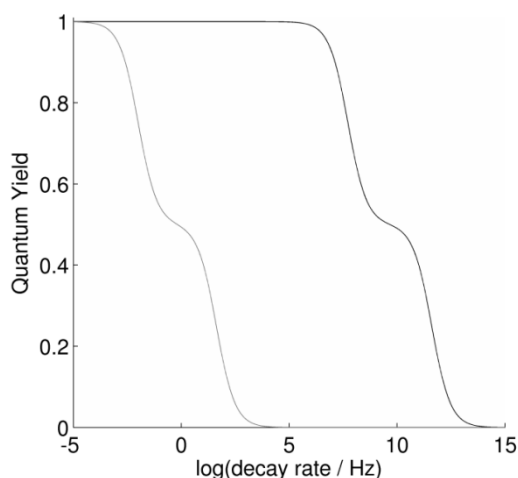


Figure 4.9: The simulated quantum yield as a function of decay.

We use equation [4.2] and our calculated exchange rates. A gray line represents the allylic system, while a black line represents the butadienyl system.

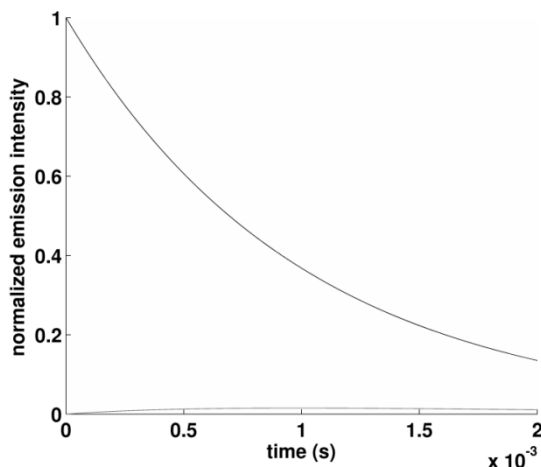


Figure 4.10: The simulated emission intensity as a function of time.

Units are arbitrary. A gray line represents the allylic system, while a black line represents the butadienyl system.

suggesting that  $\pi$  conjugation leads to faster exchange of excitons from glass to exciton supporting dye. The emission of the excitonic system as a function of time was simulated assuming the exciton localizes on the farther basin in the allyl and butadienyl silica systems. This simulation showed that the allylic system will radiate much less than the butadienyl system. We observed that the  $\pi$  conjugated butadienyl system had much higher emission, and reaches peak emission much sooner than the allylic system due to the much higher exciton exchange rate from the glass to the dye in the butadienyl system.

#### 4.6. Discussion

The lower energy of the exciton when it localizes in the exciton supporting substituents, relative to the energy when the exciton is delocalized or localizes in the glass, suggests that the dye localized exciton is the most thermodynamically stable excited state. The higher relaxation energy for localized excitons is a result of the deformation of nucleons in the vicinity of localized excitons; this energy represents the heat dissipated when the exciton localizes. For delocalized excitons, there is minimal relaxation to the minimum energy triplet state. The spin density plots showed that spin density localizes in broken and distorted bonds within the silica structure, while localization results in a deformation of nucleons forming the  $\pi$  conjugated carbon backbone. The key result is that  $\pi$  conjugated systems, even those with only a single  $\pi$  bond, support excitons. Systems without  $\pi$

conjugation do not support self trapping of excitons. The exception to this rule is the methoxide containing system, in which self trapping results in the dissociation of the methoxide group from silica, which corresponds to a radiationless decay pathway as the energy is dissipated into kinetic motion of the ions.

Self trapping occurs within the silica system when the substituent is not present or does not support exciton self trapping, which shows that our model silica cluster can support self trapped excitons consistent with experiment (16, 21-24) and theory of clusters (25, 26) and bulk-like states (6, 27, 28). Furthermore, the simulated self trapping in the silica cluster when we have exciton supporting dyes adsorbed shows that there is an energy barrier to exciton transport from the self trapped state in the silica to the exciton supporting dye. This energy barrier is also observed for self trapped excitons near the organic-inorganic interface. Our NEB model shows that the self trapped exciton is not necessarily permanently trapped in the glass. The transfer rate is highly sensitive on the organic group. Excitons transfer from the inorganic silica to a model conjugated  $\pi$  system extremely rapidly compared to an unconjugated  $\pi$  system.

The consistent results as more complete basis sets were used show that we have a sufficiently complete basis set for our simulations. The agreement between double zeta and triple zeta results also suggested that our basis set is sufficiently complete. Increasing the basis set did not lower the minimum energy nor did it significantly change the excitation and relaxation energies of the systems studied. The consistent results between simulations with diffuse and polarization functions on hydrogen and simulations with no diffuse or polarization functions on hydrogen showed that these are not needed for our simulation. Thus we expect reasonable results when using a double zeta basis with polarization and diffuse functions on heavy nuclei only when analyzing self trapping and exciton exchange.

Simulations of excitation modeled with TDDFT showed that the lowest excitation is the ground state singlet to triplet excitation in all systems. This validated our technique of using the ground state triplet found via DFT as a model for analyzing the behavior of low lying excitonic behavior. As expected, the TDDFT method produced lower energy solutions to the Schrödinger equation than the single determinant DFT method. Even for  $\pi$  conjugated inorganic systems with phenyl and butadienyl groups, which are

representative of fluorophores, the triplet DFT energy was reasonably close to that found via TDDFT.

Systems with multiple acceptors, such as our model systems with eight vinyl groups and eight allyl groups, have a lower excitation energy, which showed that there is reasonable coupling between each of these groups. Otherwise, if there is no coupling, the excitation energy would be equal to that of a single dye. Because there is coupling across the silica system from dye to dye, we expect a reasonable amount of coupling from an exciton localized inside the silica cluster to an acceptor on the surface as the distance through space is smaller than that between dyes.

The comparable excitation energies for all systems (see Table 4.3) suggested that transition energies are dominated by the electron withdrawing  $\text{SiO}_2$  system. With no electron withdrawing effects, we expected to see a trend of longer wavelength, smaller energy transitions for these substituents. An explanation is that electron density is drawn away by the  $\text{SiO}_2$  cluster. The 3 to 4 eV transition energy corresponds to a wavelength of 300 to 400 nm, which is much greater than the UV spectroscopy absorbance band expected for these substituents. This shift is consistent with the electron withdrawal from the  $\pi$  conjugated system.

Smaller energy transitions occurred with increasing  $\pi$  conjugation (Table 4.5). After relaxation, the exciton was localized completely in the dye, so we obtained the result from UV spectroscopy that greater conjugation results in smaller energy splitting between the highest occupied molecular orbital and lowest unoccupied molecular orbital. This served as verification that we are correctly modeling low lying excitons. The agreement between the vertical excitation energy for eight hydroxides, eight methyl groups and eight methoxide groups suggests that the energy of the low lying exciton is not strongly dependant on the properties of surface groups. It also shows that the exciton will localize within the silica even if groups are chemisorbed to the silica cluster when no exciton supporting dyes are present. Likewise, the lower excitation energy for exciton supporting dyes suggests that excitons will be thermodynamically driven to transfer from the silica to the dye.

For the systems without exciton supporting dyes, the low excitation energies (less than that of bulk silica) are consistent with excitation to a low lying state within the band gap of silica. Our results show that exciton transport to fluorophores is thermodynamically

favorable, there is not an observed benefit to using triple zeta basis, or the diffuse and polarization functions on hydrogen, and that the Pople basis set does not generate chemically intuitive results for all of our systems. Therefore analysis of exciton exchange can be performed using TDDFT with the double zeta Dunning basis set.

The fact that there is at least an order of magnitude difference in exchange rate calculated from our method and that of LZ and Eyring show that it is not appropriate to use either in the regime of moderate coupling. Furthermore, when the region of coupling does not fall on the saddle point (an assumption of LZ and Marcus) the error is exacerbated. The combination of energetic barrier and moderate coupling (Figure 4.7) make it unclear whether a LZ approach or an Eyring approach is appropriate, or if either are appropriate, so we developed our own method that is appropriate in the regime of moderate coupling. We showed the correspondence of our method with that of Marcus, Eyring and LZ methods in the theory section. The smooth transition from our own model between the result using Eyring theory and the result using LZ theory (Figure 4.2A) show that it correctly combines the properties of the two theories at their limits. The correspondence between our method and Eyring theory at the high coupling limit is intuitive, as in the limit of high coupling the system will remain on the lower adiabatic surface throughout the course of reaction. Likewise, at the low coupling limit, the system will be limited by coupling as the system has a low chance to transition between diabatic surfaces regardless of how fast the nuclei are moving. We see this match at low coupling with our model. Since our model is correct at the high and low coupling limits, we believe it is also correct in the regime of moderate coupling which our systems occupy.

The result of the LZ approximation agrees well with the transition probability found by propagating a system with linear, parabolic and Brownian motion sweep profiles. This shows that the assumption that energy must sweep indefinitely does not need to be valid to produce reasonable results. Agreement was also observed between the LZ approximation result, the linear sweep, and the parabolic sweep corresponding to the change in velocity as our system climbed the lower adiabatic surface through the region of coupling. This shows that LZ theory is viable even if the region of coupling does not fall on the saddle point. Because of this agreement, it is safe to use the LZ approximation in our model. Because we generate our own sweep profile via NEB (Figure 4.7), this is actually not necessary. We can replace the LZ transition probability in equation 4.7 with a probability generated by numerically propagating the system using the converged NEB

energy profile. However, our results indicate that there is no benefit to doing so. Therefore while our theory does not require the LZ approximation, it is reasonable to use it in the interest of saving computation time.

Figures 4.2, 4.3 and 4.4 show why the approximation is valid. Since the time in which the diabatic surfaces couple well is small relative to the total time required for the exciton to transfer even for moderately coupled systems, the energy sweep through the coupling region is close to linear. When Brownian motion is added to the linear sweep, the decrease in transition probability from the added Brownian sweep speed is partially negated by the repeated sweeping through the region of coupling. Therefore the deviation is marginal. As coupling decreases, the speed at which transfer between diabatic surfaces occurs effectively also decreases. At the low coupling limit, the rate matches that of the LZ approximation. We ignore this effect because this deviation is small at low coupling, and because the time required for our system with kinetic energy  $kT$  to traverse the minimum energy pathway from reactions to products is not significantly longer than the vibrational period (thus there is not much opportunity for the system to change trajectory).

The relaxation energies during exciton relaxation show good agreement between Pople and Dunning basis sets and between double and triple Zeta basis sets with the exception of the allylic substituent (Table 4.4). The energy lost is diffused as phonons into the surrounding material. As the dye becomes larger, nuclear motion is less constrained, so the relaxation energy becomes larger.

The results generated via ELZ theory show that energy exchange to the unconjugated allylic system is not competitive with the rate of decay of approximately 1000 Hz. (29) However, with  $\pi$  conjugation, the forward exchange rate is high enough to compete with that of spontaneous decay. This fast exchange rate, combined with the high difference in energy between the silica localized and dye localized systems (Figure 4.6) indicates that the excitons will be thermodynamically driven into the dye in our system. The increase of exchange rate with  $\pi$  conjugation is likely a result of a combined effect of less distortion of the  $\pi$  conjugated system, and stronger transition dipole moment of the dye. In any case, because the exchange rate increases with degree of  $\pi$  conjugation, we expect self trapped excitons to be thermodynamically driven into larger dyes as well. The exchange rate for butadiene decreases with distance, as expected if the coupling is mediated by dipole-dipole interaction or electron overlap. Even when displaced from the dye, the exciton

transport rate is reasonably high which suggests that this phenomenon can occur even if the exciton self traps in a region that is not in the immediate vicinity of an exciton acceptor.

The quantum yield simulations of exciton transport to dyes shows that the ratio of exciton transfer to exciton relaxation is critical. Exciton transfer to fluorophores is likely to occur even if an exciton has self trapped within the silica network assuming reasonable values of radiationless decay in the silica.

#### **4.7. Conclusions**

We have shown that Eyring theory, used for strongly coupled systems, and LZ theory, used for weakly coupled systems, can be bridged. We have derived a model that is valid in the regime of moderate coupling, shown that it is consistent with previously developed theories, and shown how to use our theory to calculate exchange rates and quantum yields for arbitrary systems.

Our results indicate that exciton transport from amorphous silica to chemisorbed dyes falls into a moderate coupling regime if the exciton localizes in the vicinity of the surface.

Extrapolating from our results, exciton transport from self trapped excitons to nearby dyes will be thermodynamically driven for  $\pi$  conjugated exciton acceptors.

#### **Acknowledgement**

The authors would like to thank the University of Arizona High Performance Computing Center and Pacific Northwest National laboratory for access to computation resources.

The authors would like to thank Dr Marty Pagel for assistance with technical writing.

CHAPTER 5

FUTURE DIRECTIONS

## 5.1. Measuring Chemical Exchange Rates with CEST MRI Analysis Methods

### 5.1.1. Summary of Current Status

Before our contributions to the CEST MRI research field, three non-linear and four linear analysis methods had been developed to measure chemical exchange rates using CEST MRI results. The non-linear analysis methods included Bloch fitting, QUEST, and QUESP analyses (1,2). The linear analysis methods included LB-QUESP (also known as the “Omega Plot” method), and LB-conc, EH-conc, and HW-conc analyses (3,4). These seven methods for measuring chemical exchange rates had not been compared to assess their relative accuracies and precisions, or to evaluate their relative dependencies on experimental conditions. Furthermore, these methods were developed to measure slow chemical exchange rates of CEST agents, and had not been tested to determine their accuracies or precisions when measuring fast chemical exchange rates.

Our contributions to this field evaluated these analysis methods through theoretical simulations and experimental evaluations. During our analyses, we discovered one additional non-linear analysis method, QUESPT, and five linear analysis methods, EH-QUESP, HW-QUESP, L-QUEST, RL-QUEST and UL-QUEST methods (5,6). We compared the accuracies and precisions of the previously known analysis methods and our new methods, determined the relative dependencies on experimental conditions for each method, and assessed systems that have slow and fast chemical exchange rates.

Our results determined that the Bloch fitting method provides the best accuracy and precision when estimating slow and fast chemical exchange rates. However, this method requires substantial expertise and computation time to provide reliable results. For comparison, HW-QUESP provides excellent accuracy and precision when measuring fast chemical exchange rates, which is a facile linear analysis method that is relatively insensitive to experimental conditions. RL-QUEST and LB-QUESP provide excellent measurement accuracies and precisions for systems with slow chemical exchange rates, as long as a high saturation power is used.

Our research studies also validated that the Lorentzian line fitting method can provide accurate and precise estimates of the amplitudes of CEST effects, including the fitting of multiple proton pools within the same spectrum. However, this fitting method has lower accuracy when the signal-to-noise of the CEST spectrum is low (i.e., when CEST effects

have low amplitude) and when high saturation powers cause the features of the CEST spectrum to become very broad.

## **5.1.2. Further Method Developments**

### **5.1.2.1. In vivo CEST-MRI Methods**

Because we now understand the performance characteristics of each of the 13 analysis methods, under different experimental conditions and for slow and fast chemical exchange rates, applying these analysis methods to measure chemical exchange rates within in vivo systems is a natural next step. Our research group has pioneered the development of CEST MRI protocols for pre-clinical in vivo studies. Our initial protocol designs optimized the type and parameters of the acquisition period of the MRI protocol based on the  $T_1$  relaxation rate of the CEST agent, and then optimized the CEST saturation period based on the type of MRI acquisition period that was selected. Our subsequent protocol designs used a fast MRI acquisition protocol known as Fast Imaging with Steady state Precession (FISP), which greatly reduced the need to consider the  $T_1$  relaxation rate of the CEST agent during data acquisition. [7] Subsequently, the CEST saturation period did not need to be optimized relative to the FISP MRI acquisition period. Therefore, our CEST-FISP MRI protocol provides the opportunity to use a range of saturation powers or saturation times for the CEST saturation period without affecting the FISP MR image acquisition. This is a profound advantage for translating our methods to pre-clinical in vivo studies.

### **5.1.2.2. Methods for Analysing CEST Spectra**

Our evaluations of the Lorentzian line fitting method for measuring the amplitudes of CEST effects in CEST spectra showed that this analysis method can produce inaccurate results when trying to fit noisy or broad features in CEST spectra. Our current solution to this problem is to ensure that the saturation time and power used for experimental studies produce CEST spectra with sufficient signal amplitudes and sufficiently narrow widths for reasonable fittings. However, other analysis methods may provide better fittings of CEST spectra that are noisy or have broad features.

For example, Bayesian analysis has been applied to evaluate NMR spectra with relatively few spectral features, and this methodology may be applied to analyse CEST spectra. [8]

Bayesian analysis estimates the probability of the existence of spectral features, and works well when a limited number of features are present. Our initial studies with Bayesian analyses have not produced promising results, but additional studies are warranted to further investigate this methodology.

Also, cubic spline fittings have been used to fit CEST spectra, and polynomial fittings may provide yet another methodology for fitting CEST spectra (9). Initial studies of these methods have indicated that cubic spline and polynomial fitting methods provide no additional benefit relative to Lorentzian line fitting methods, and are slower than Lorentzian line fittings. Yet additional studies are warranted to investigate whether these alternative methods improve the fittings of CEST spectra with low CEST amplitudes and broad spectral features.

Another approach to mitigating the effects of experimental noise in CEST spectra is to fit via variational Bayesian inference instead of fitting CEST spectra using a least squares minimization approach. While performing our previous studies, we observed that fitting via non-linear least squares had the possibility of over fitting into experimental noise. So using CEST spectra to determine chemical properties may be problematic when the spectra are noisy.

The salient differences between least squares fitting and variational Bayesian inference are that distributions of parameters are fit instead of parameters, and experimental noise of the data is fit along with parameters. These both tend to result in noise being ignored instead of being used to over fit data. A distribution with mean and variance is fitted for each model parameter. Thus instead of fitting a single curve, a distribution of curves that capture all data points is fit. The fit converges when this distribution captures each of the data points to within the fitted value for noise. When using variational Bayesian inference, noisy data results in large variance for fitted distributions of parameters instead of the curve “locking” onto a local minimum that arises from a noisy data point. As a further advantage, the variational Bayesian method has lower bounds that are the evidence for fitting. This lower bound is obtained from the free energy function. The free energy is analogous to the residual of least squares fitting. While the normalizing factor cannot be easily obtained, using this evidence function allows one to compare the quality of fits between experiments in units that are proportional to the log likelihood of the fit being correct. As another advantage to the variational Bayesian method, a comparison of the

fitted parameters to noise can be made to decide if CEST measurements are large enough to be statistically significant since noise is fit along with the experimental data.

### **5.1.2.3. Methods for Developing CEST Saturation Periods with Shaped Pulses**

To date, the CEST research field has primarily used a single, long, continuous wave (CW) saturation pulse during the entire saturation period of a CEST-NMR study with chemical solutions. A CW pulse provides the greatest saturation efficiency, and the small volume of the NMR sample experiences little or no heating (10). The saturation period during in vivo CEST MRI studies typically cannot use a similar CW saturation pulse because the larger volume of a mouse or patient in the MRI magnet would experience substantial heating that would exceed the safety limit known as the Specific Absorption Ratio (11). Therefore, most in vivo CEST MRI studies have used a series of shorter Gaussian-shaped saturation pulses that generate little or no heating to tissue while still providing good saturation efficiency.

Using a Gaussian-shaped saturation pulse saturates a range of MR frequencies, with a Gaussian-shaped profile of saturation amplitude centered at the MR frequency of the saturation pulse. Yet measuring the features of a CEST spectrum may require the saturation of a narrow band of frequencies centred at the MR frequency of a single exchangeable proton, to avoid saturating additional protons or to avoid direct saturation of water. Selective saturation may be especially problematic for DIACEST agents due to the narrow range of MR frequencies of these agents. Yet PARACEST agents can generate broad features in CEST spectra which can create overlap if the agent generates multiple CEST effects of a CEST effect has a MR frequency close to water. Therefore, a Gaussian-shaped saturation pulse is clearly not ideal for generating CEST spectra.

The Bloch fitting methods developed and used in our research studies can be directly applied to simulate the effects of saturation pulses that have other shapes. These shapes can have evolving phases as well as amplitudes, so that these pulse shapes are two-dimensional. These simulations are accomplished by modelling the shaped pulse via a series of short time pulses that approximate the waveform of the simulated pulse, analogous to the way that a Riemann sum approximates an arbitrary function. Our initial studies have used a naïve approach that used delta functions on resonance with each proton pool with a power density proportional to the optimal power density for generating

the expected CEST spectra features. This approach generated promising results that simulated CEST spectra of iopromide with greater CEST amplitudes. However, experimental investigations must be conducted to assess our simulated results. Additional simulations should be performed to assess the effects of  $B_0$  and  $B_1$  inhomogeneities, and the limited MR frequency resolution of CEST spectra, when optimizing saturation pulse shapes. Finally, the optimization of saturation pulse shapes for detecting PARACEST agents should be investigated.

An extension of the work presented in this thesis is the application of data fitting to noisy CEST spectra. Fitting may be improved by refining the experiment or improving the analysis of experimental data. To improve the experiment, we propose to use shaped pulses guided by Bloch simulation. We can simulate a shaped pulse by combining multiple short block pulses together, analogously to approximating a function with a Riemann sum. By defining a fitness function representing a desired outcome, such as contrast to noise ratio, we can tune the power, phase and frequency of each individual block pulse to generate a pulse waveform that best achieves the desired outcome. We propose extending the analysis done in this work by using the variational Bayesian method. This method will help avoid over fitting of noise as it fits the noise of the spectrum and a distribution of parameters instead of achieving a best fit of the CEST spectrum.

The Bloch simulation software developed to model methods explained in this work can be directly applied to the simulation of shaped pulses. This is done by modelling the shaped pulse via a series of short time pulses that approximate the waveform of the simulated pulse analogously to the way a Riemann sum approximates an arbitrary function. Shaped pulses have the potential to enhance contrast from CEST agents by exciting multiple proton pools via a multi-bandwidth pulse. A naïve approach would generate a shaped pulse that results in delta functions on resonance with each proton pool with a power density proportional to the optimal power density for CEST. Because of time constraints, the frequency resolution for measuring the CEST spectrum is limited. Therefore shaping the pulse bandwidth so that there is significant signal with a slightly off resonance pulse may result in better CEST spectra.

The measurement precision of properties such as pH is limited by the precision of CEST measurements for each proton pool. If the CEST effects from both proton pools are difficult to assess in a CEST spectrum, and are buried in experimental noise, then

measurements of pH are problematic. A solution to this problem is to apply a dual bandwidth pulse that will generate two peaks that can be fit well via either Lorentzian line shape fitting or Bloch-McConnell equations. By applying a waveform that excites both proton pools instead of a single pool, we hypothesize that both proton pools will generate CEST effects that are greater than experimental noise.

### **5.1.3. Biomedical Molecular Imaging Applications**

Our research group currently uses in vivo CEST MRI to measure the extracellular pH in solid tumor tissues (12,13,14), and to detect enzyme activities in biochemical solutions (15,16) and within tumor tissues (17). A critical design criterion of our experimental approach is the use of a ratio of the amplitudes of two CEST effects. This ratiometric method is required because each CEST amplitude is dependent on the endogenous  $T_1$  relaxation time and the concentration of water in the tissue, in addition to the chemical exchange rate of the CEST agent. Conversely, a ratio of two CEST amplitudes is independent of endogenous  $T_1$  relaxation time and the concentration of water in tissue. Furthermore, our previous studies have shown that incomplete saturation affects the amplitude of each CEST effect, but does not affect a ratio of these CEST amplitudes, which eliminates a potential pitfall during in vivo studies with poor  $B_1$  magnetic field inhomogeneities (18).

Directly measuring the chemical exchange rate of a CEST effect provides another method for eliminating the effects of endogenous  $T_1$  relaxation time, water concentration and incomplete saturation. This may be an improvement relative to our current ratiometric method, because only one CEST effect would need to be accurately measured. This improvement may be particularly important for DIACEST agents, because these agents have a narrow range of NMR chemical shifts that may overlap, especially under experimental conditions with high saturation powers that cause broad features in CEST spectra. Creating DIACEST agents with only one exchangeable proton can improve the analysis of CEST spectra. In addition, reducing the minimum number of exchangeable protons on a CEST agent from two (for the ratiometric approach) to one (for approaches that directly measure a chemical exchange rate) may provide flexibility in designing new CEST agents for molecular imaging.

For example, our research group has pioneered the use of iopromide (Ultravist™, Bayer Healthcare, Inc.) to measure extracellular pH in solid tumor tissues via the ratio of two CEST effects. Iopromide has two amide protons that exchange with water and have different MR chemical shifts, which can generate two CEST effects. Other research colleagues have measured pH in tumors and kidney tissues using iopamidol (Isovue™, Bracco Diagnostics, Inc.) (19), which also has two amide protons that exchange with water and have different MR chemical shifts. For comparison, ioxaglate (Hexabrix™, Guerbet LLC) is similar to iopromide and iopamidol because it has two amide protons that exchange with water. However, the symmetry of the chemical structure of ioxaglate causes both exchangeable amide protons to have the same MR chemical shift, so that ioxaglate cannot be used to measure pH using a ratio of two detected CEST effects. Yet ioxaglate has the advantage of generating twice as much CEST amplitude per molecule due to the degeneracy of this MR chemical shift of its amide protons. Therefore measuring the chemical exchange rate of ioxaglate may provide a method for measuring tumor pH while improving the detected CEST signal by a factor of two. Considering that our CEST MRI methods that measure tumor pH are limited by image noise, this two-fold improvement in CEST signal is a major potential advantage.

Our analysis of the power response of CEST can be applied to the OPARACHEE method [1]. In this method, CEST is performed by tipping the net magnetic vector of water with a WALTZ-16 pulse. If there are no labile protons, the WALTZ pulse will result in a 360° flip back to the Z axis. If a water proton exchanges with a solute proton during the WALTZ pulse, these two protons will no longer be aligned with the magnetization vector of the other water protons. This is because a change of the precession frequency during the WALTZ pulse prevents the protons from experiencing the full 360° of the WALTZ pulse.

Because CEST response to pulse power can be used to generate a concentration independent method of measuring exchange rate, we hypothesize that a similar concentration independent method of measuring exchange rate exists for the OPARACHEE method. By measuring the OPARACHEE contrast as a function of WALTZ pulse saturation power, we will be able to very rapidly measure the total rate of proton exchange from solute to water.

## 5.2. Modelling Exciton Exchange Rates in Chemical Systems

### 5.2.1. Summary of Current Status

Previously, exchange rates have been modelled using methods derived for the weak coupling limit such as Forster Resonant Energy Transfer (FRET), Landau-Zener theory and Marcus theory, or for the strong coupling limit such as Eyring theory. Before our work, it was unclear what method is appropriate for modelling exciton exchange in the moderate coupling limit. We've shown that intermediate coupling can be modelled acceptably via Landau-Zener type approaches (Marcus, FRET). The primary result of our work with modelling exciton transfer in disordered systems is that our model for the intermediate coupling regime gives results that are within an order of magnitude of models that are derived and only valid in the weak coupling limit.

### 5.2.2. Weak Coupling

Further work with our moderate coupling regime model should use systems that are more tractable and more directly relevant to exciton exchange. We selected a system for our initial study that had an amorphous donor system, which made comparison with experimental results difficult. Experimental emission spectra of this amorphous system show a Gaussian shaped emission profile as a result of the multitude of self trapped states. This made the comparison of emission rates calculated via Einstein coefficients to experiment impossible. In order to better verify our method we could perform similar analysis on systems that are better understood and better studied. Experimentally relevant systems that do not involve amorphous donors or acceptors include an exciton supporting ordered crystal, or Fluorescein or Chlorophyll at a distance appropriate to the critical distance calculated by Forster. While our work showed that the assumptions made using these methods calculate the exciton transfer rate to within an order of magnitude, this would serve as a way to validate the theory against experimental data. With simple donor-acceptor systems such as above the exchange rates can be validated in terms of accuracy and also qualitative behaviour, such as the well known  $1/R^6$  fall off of transfer efficiency with distance.

With the system we use, we do not reproduce the Urbach rule (Figure 5.1). The size of the system required to obtain

representative self trapped states reproducing the Urbach rule is much larger than what is tractable with the density functional theory implementation we used. With our model cluster, the energy barrier along the minimum energy pathway from the initial state to the final state is likely much higher than the barrier would be if calculated with a larger

system because the pathway permitted for reaction is constrained. Assuming a naïve implementation of DFT, time requirements for a larger system will scale as the cube of system size because of the matrix operations involved in diagonalizing the Hamiltonian. Since convergence of the minimum energy pathway for our cluster took on the order of a week for each pathway, a system twice as large would take on the order of months. This does not include converging each basin, calculating Hessians and solving for excitations with TDDFT. For larger systems to be modelled, we would need to use a linear scaling DFT method that assumes locality of interaction of the electronic density.

Complimentary models to our Glass donor – Dye acceptor would be a Dye donor – Glass acceptor, and a glass donor – glass acceptor. With the dyes we used in our model, the self trapping reorganizational energy is too high any relevant exchange from dye to glass. However, we have shown that the reorganizational energy is lower for larger dyes. With a dye such as a porphyrin ring, Fluorescein, or other rigid exciton supporting dye, the reorganizational energy is sufficiently low (on the order of .3 eV) that exciton transfer to the glass may be sufficiently high for exciton transfer to compete favourably with spontaneous relaxation.

Based on our results there is not any significant transfer of energy throughout the glassy system after localization of the exaction in the dye. Exchange rates through space after localization are approximately zero. However, the theory developed for localized excitons can be extended to delocalized excitons that are in higher energy states. Since these

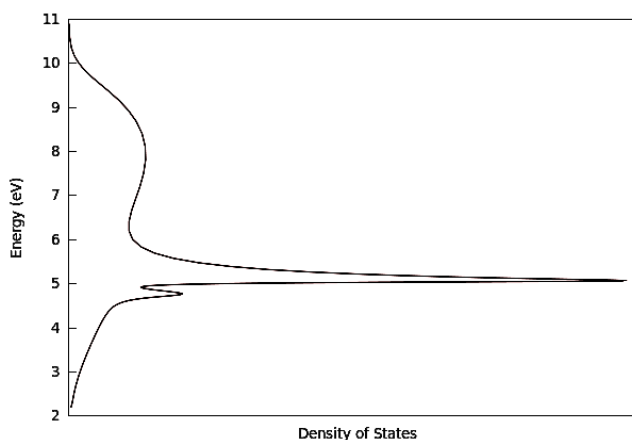


Figure 5.1: Density of self trapped exciton states as a function of energy for our model cluster.

states are delocalized, a plane wave type approach with higher states calculated via TDDFT would model exciton transport through a glass.

The biggest hurdle to performing the exchange rate analysis in chapter 4 was the computational cost of generating and solving the minimum energy pathway of reaction via NEB. A natural extension of this method is to use a rising NEB method with a single bead to capture the transition state. The rising NEB method would reduce the number of dimensions of the problem by requiring only the single rising bead to tightly converge. For our systems we used eight beads to loosely converge, then eight more beads in the vicinity of the saddle point and point of coupling to accurately estimate the activation energy and coupling parameter. By using a modified rising NEB algorithm where the objective function in the unnudged direction is coupling, it is possible to systematically search for both the point of coupling and the saddle point with a single bead. This would reduce the time requirements for search by an order of magnitude.

### **5.3. CEST Exchange Modelling**

Modelling exchange rates of CEST agents is a non-trivial problem. Eyring theory cannot be applied directly because proton tunnelling may contribute significantly to the proton exchange rate. By modelling the exchanging protons with wave functions, our model developed in chapter 4 can be directly applied to proton tunnelling during exchange from solute to water. Furthermore, because the heavy ions experience only a minor change in position during the exchange of protons, the parabolic ionic potential of Marcus theory is valid. The external potential determining the shape of the wave functions for the exchanging protons can be determined via a Hessian calculation. Once the wave functions are generated, we can directly calculate the dipole-dipole interaction and wave function overlap which will capture the nuclear Overhauser effect and chemical exchange.

The simulation of exchange rate will facilitate our understanding of the effects of various functional groups near the labile protons on the CEST effect. This also will enable the study of CEST effects in novel chemical structures. By modelling the exchange rate, one can direct synthesis efforts towards molecules that are most likely to have the properties needed for a particular CEST experiment.

#### **5.4. Preclinical & Clinical MRI**

Shaped pulses and the extension to analysis of noisy data will facilitate in-vivo pre-clinical and clinical CEST MRI studies where restrictions on time, specific absorption ratio and cost limit the quality of data. Because we have developed methods that facilitate measurement of chemical properties, and quantified how well they perform, the next step is to move toward preclinical and clinical applications. This entails programming of MRI scanners to perform presaturation experiments with an imaging sequence that is fast enough and precise enough to generate a large number of contrast images at a level of precision that enables the data to be analyzed well.

## APPENDIX A

REVIEW OF CALCULATIONS  
OF ELECTRON TRANSFER RATES

### A.1. Motivation for Developing Eyring-Landau-Zener Theory

There are many theories for modelling energy transfer between chemical systems and within a chemical system. These can roughly be classified into those that are derived for strongly coupled systems, which would be Eyring Transition State Theory, and those that are derived for weakly coupled systems, which would be Landau-Zener theory, Förster Resonant Energy Transfer (FRET) theory, Dexter theory and Marcus theory. Our system described in chapter 4 does not fall into either category. The coupling is weak enough that Eyring Transition State theory gives poor results, but strong enough that it is not clear if the weak coupling theories are valid. Furthermore, Marcus and FRET theories are derived to be used with experimental data, so are not conducive to analyzing energy transfer rates from *ab initio* calculations. A literature search did not provide an approach for the intermediate coupling regime, nor was it clear which of these theories was appropriate. To meet this need, we developed our own theory that is derived from Eyring theory and Landau-Zener theory, and produces the same result as Marcus theory. While not shown in our work, one could replace the coupling element from our theory with that of a dipole-dipole interaction to reproduce the results of Förster, or with electron orbital overlap to reproduce the results of Dexter. Several of the models of energy transport are visually depicted in figure A.1.

In this introduction, a short explanation of coupling will be provided. We will explain the adiabatic and diabatic basis, and how coupling affects states expressed in each basis. Afterwards, we will review briefly the common models for energy transfer.

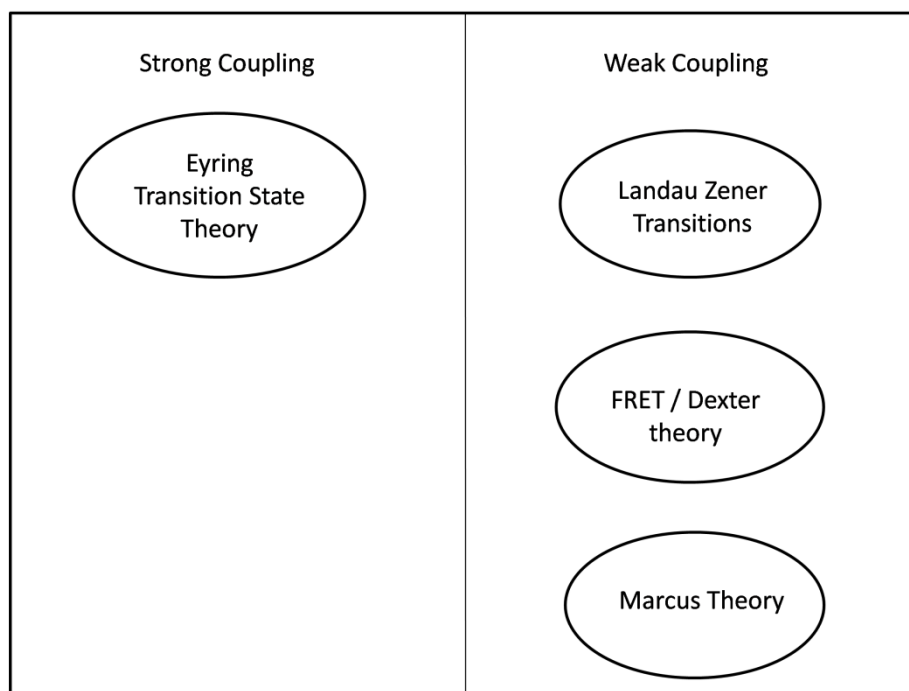


Figure A.1: A visual representation of kinetic theories relevant to exciton transport.

## A.2. Coupling

Coupling refers to coherent transfer of energy between diabatic basis states. The classical example is two masses attached by a spring. Energy will resonate between the two masses with a frequency equal to the beat frequency of the gerade and ungerade swinging of the two masses. If the masses are heavy, and the spring weak, the period of energy transfer will be longer than the eigenvectors of the system with the shortest period ( $1/H_{ab} \gg 1/|H|$ , where  $H_{ab}$  is coupling and  $|H|$  is the Hilbert-Schmidt norm of the Hamiltonian) and the oscillation will visibly transfer from one mass to the other. In this work, we refer to this phenomenon as weak coupling. If the masses are light, and the spring strong, the period of energy transfer will be much less than the period of eigenvectors of the system ( $1/H_{ab} \ll 1/|H|$ ) and the transfer will not be discernable from the oscillation of the masses. Therefore energy will transfer with a period on the order of that of eigenvectors of the system. In this work, we refer to this phenomenon as strong coupling.

If we replace the masses with electrons, and the spring with coulombic interaction and orbital overlap, we can analogously have weakly coupled states when the orbital overlap and coulombic interaction is low, or strongly coupled states when the orbital overlap and coulombic interaction is high.

## A.3. Adiabatic and Diabatic Basis

A diabatic energy surface as a function of external potential represents the energy of the system if the electronic energy does not transfer through space. This would represent the energy of a single exciton supporting entity as the nucleons are distorted through space.

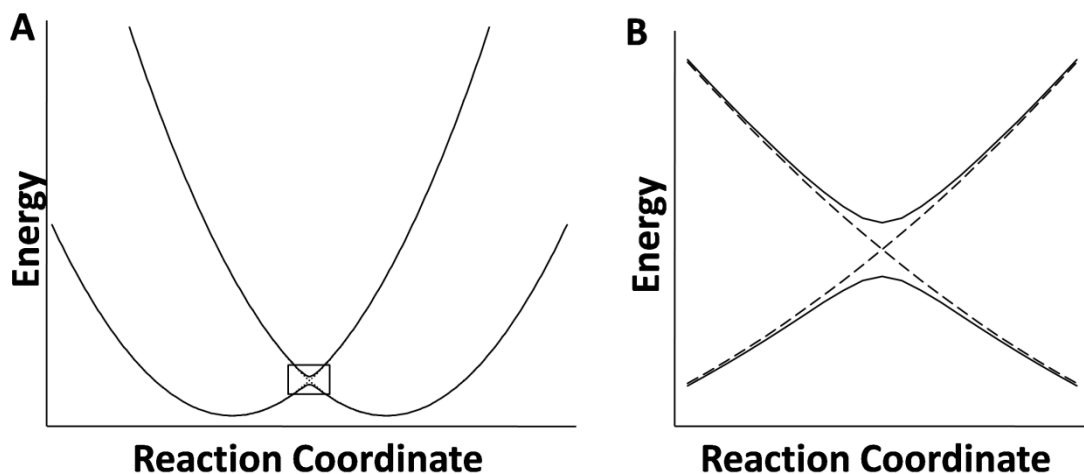


Figure A.2: Energy level diagram of diabatic and adiabatic surfaces. The Y axis is energy, the x axis is the reaction coordinate. The adiabatic energy surfaces are solid lines while the diabatic energy surfaces are dotted lines. A) shows the energy surfaces for a typical chemical reaction, with a box showing the detail for figure B). At the point of intersection, the solid lines are separated from the point of intersection by a value equal to  $|H_{ab}|^2$ . The total splitting is twice the value of coupling.

In this work the external potential is the coulombic interaction of nucleons with electrons.

Figure 2A shows two such diabatic surfaces, represented with dotted lines. There is a diabatic energy surface on the left side of figure 2A, with a parabolic shape consistent with Hook's law. There is another on the right side of figure 2A. Figure 2B shows a detail of figure 2A in the region where the two diabatic energy surfaces intersect.

Adiabatic energy surfaces follow eigenvalues of the Hamiltonian. They are related to diabatic surfaces via the following formulas:

$$H(r) = \begin{bmatrix} H_a & -iH_{ab} \\ iH_{ab} & H_b \end{bmatrix} \quad [\text{A.1}]$$

$$H\varphi = E\varphi \quad [\text{A.2}]$$

H is the Hamiltonian,  $H_a$  is the energy of diabatic surface a,  $H_b$  is the energy of diabatic surface b,  $H_{ab}$  is the coupling between the diabatic states, and E is the eigenvalue associated with eigenvector  $\varphi$ . It is an eigenvector / eigenvalue problem to find the energy, E, of the adiabatic surfaces. As per the usual method:

$$\det(H - EI) = 0 \quad [\text{A.3}]$$

$$H_a \cdot H_b - |H_{ab}|^2 - (H_a + H_b) \cdot E + E^2 = 0 \quad [\text{A.4}]$$

$$H_a \cdot H_b - |H_{ab}|^2 - (H_a + H_b) \cdot E + E^2 = 0 \quad [\text{A.5}]$$

$$E = \frac{(H_a + H_b) \pm \sqrt{(H_a + H_b)^2 - 4(H_a \cdot H_b - |H_{ab}|^2)}}{2} \quad [\text{A.6}]$$

$$E = \frac{(H_a + H_b) \pm \sqrt{(H_a - H_b)^2 - 4|H_{ab}|^2}}{2} \quad [\text{A.7}]$$

In the case where coupling,  $H_{ab}$ , is zero, we derive

$$E = \frac{(H_a + H_b) \pm \sqrt{(H_a - H_b)^2}}{2} \quad [\text{A.8}]$$

$$E = \frac{H_a + H_b \pm H_a \mp H_b}{2} \quad [\text{A.9}]$$

$$E = \{H_a, H_b\} \quad [\text{A.10}]$$

This shows that the diabatic basis represents independent systems with no coupling.

At the point where each diabatic basis energy surface intersects:

$$H_a = H_b \quad [\text{A.11}]$$

$$E = H_a \pm |H_{ab}| = H_b \pm |H_{ab}| \quad [\text{A.12}]$$

This result shows that the adiabatic surfaces have an avoided crossing. They are separated by twice the coupling between the diabatic states at the point of intersection.

The adiabatic and diabatic bases are essentially the same unless the system is in the region of coupling. We are interested in the region of coupling, as we are concerned with nucleon motion over the potential energy barrier at the intersection of diabatic surfaces, and we are concerned with energy transfer between diabatic surfaces as the nucleons deform along the reaction coordinate pathway.

#### A.4. Exchange Models

##### A.4.1. Landau-Zener theory

Landau-Zener theory is a semiclassical closed form solution to the Schrödinger equation that provides the chance of transition between lower and upper adiabatic surfaces as the external potential sweeps through the region where diabatic surfaces intersect.

The chance of an adiabatic transition (a transition from the lower to upper adiabatic surfaces as the nucleons sweep through the region of coupling) is the following (6):

$$P_{\text{adiabatic transition}} \left( H_{ab}, \frac{dE_{ab}}{dt} \right) = e^{-\frac{2\pi |H_{ab}|^2}{\hbar \frac{dE_{ab}}{dt}}} \quad [\text{A.13}]$$

Normalizing probability measure to 1,

$$P_{\text{diabatic transition}} \left( H_{ab}, \frac{dE_{ab}}{dt} \right) = 1 - P_{\text{adiabatic transition}} \left( H_{ab}, \frac{dE_{ab}}{dt} \right) = 1 - e^{-\frac{2\pi |H_{ab}|^2}{\hbar \frac{dE_{ab}}{dt}}} \quad [\text{A.14}]$$

This theory assumes a linear sweep rate for  $E_{ab}$ , the difference in energy between the diabatic energy levels, throughout the region of coupling. In a real system, it is not clear if this is valid.

##### A.4.2. Marcus theory

Marcus theory treats nuclear motion as an external perturbation. As the nucleons sweep from the initial to final configuration, the eigenvalues for each eigenvector will sweep by each other, separated by twice the coupling value. This theory can be derived directly by solving for the intersection of two parabolas to find the activation energy, and applying equation [A.14] assuming the weak coupling limit to obtain the prefactor. If coupling is

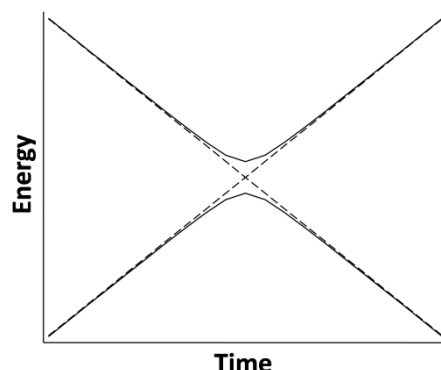


Figure A.3: Landau-Zener sweep. Diabatic energy for states a and b as a function of time are plotted as dotted lines. Adiabatic energies for upper and lower surfaces are also plotted. Note the similarity to figure A.2B. Time and reaction coordinate are linearly related because of the assumption that sweep rate is constant.

weak, the nucleons could sweep past the transition state many times without the system transitioning to the final diabatic surface. For this reason, the exchange rate is dominated by the coupling between initial and final states.

#### A.4.3. **Eyring theory**

Eyring theory, also known as transition state theory, uses statistical mechanics to estimate prefactors and exponential terms for chemical reactions. The prefactor is a ratio of the phase space available at the transition state and the ratio available at the initial state. The exponential is the usual activation energy incorporated into the Boltzmann distribution. This theory assumes transition from initial to final state on the first nucleon sweep. For this reason the exchange rate is determined from the activation energy, with a minor effect from the ratio of available phase space.

In cases where transfer has a moderate chance to occur with each nucleon sweep, then neither theory is appropriate. The exchange rate will be lower than the exchange rate determined by Eyring theory, as multiple sweeps will be expected for energy transfer. Also the exchange rate will be higher than the rate determined by Landau-Zener theory, because the exchange rate is limited by an energetic barrier.

## APPENDIX B

DERIVATION OF OMEGA PLOT, LINEAR QUEST,  
QUESP, QUEST AND QUESPT FROM THE BLOCH EQUATIONS

## B.1. Derivation of Omega Plot / Linear QUESP from the Bloch-McConnell Equations

We start with the Bloch equations modified for chemical exchange.

$$A = \begin{bmatrix} -\frac{1}{T_2 \text{ solvent}} - k_{ba}\chi & -(\omega_{\text{larmor solvent}} - \omega_{RF}) & -\omega_{\text{nutatation y}} & k_{ba} & 0 & 0 \\ (\omega_{\text{larmor solvent}} - \omega_{RF}) & -\frac{1}{T_2 \text{ solvent}} - k_{ba}\chi & -\omega_{\text{nutatation x}} & 0 & k_{ba} & 0 \\ \omega_{\text{nutatation y}} & \omega_{\text{nutatation x}} & -\frac{1}{T_1 \text{ solvent}} - k_{ba}\chi & 0 & 0 & k_{ba} \\ k_{ba}\chi & 0 & 0 & -\frac{1}{T_2 \text{ solute}} - k_{ba} & -(\omega_{\text{larmor solute}} - \omega_{RF}) & -\omega_{\text{nutatation y}} \\ 0 & k_{ba}\chi & 0 & (\omega_{\text{larmor solute}} - \omega_{RF}) & -\frac{1}{T_2 \text{ solute}} - k_{ba} & -\omega_{\text{nutatation x}} \\ 0 & 0 & k_{ba}\chi & \omega_{\text{nutatation y}} & \omega_{\text{nutatation x}} & -\frac{1}{T_1 \text{ solute}} - k_{ba} \end{bmatrix} \quad [\text{B.1a}]$$

$$b = \begin{bmatrix} 0 \\ 0 \\ \frac{(1-\chi)}{T_1 \text{ solvent}} \\ 0 \\ 0 \\ \frac{\chi}{T_1 \text{ solute}} \end{bmatrix} \quad [\text{B.1b}]$$

The symbolic evaluation of the 6 by 6 A matrix is not tractable for parsing by a human. So we make the assumption that only longitudinal magnetization is relevant. Thus we reduce the problem to only longitudinal magnetization. We replace the upper left 3 by 3 Bloch plus exchange matrix of A with the element at (3,3), the lower left 3 by 3 exchange matrix with the element at (6,3), the upper right 3 by 3 exchange matrix with the element (3,6) and the lower right Bloch plus exchange matrix with the element at (6,6). Because power density scales as field strength squared, and the rate of excitation will scale with power density, we include the square of the nutation rate in the (6,6) element times the absorption lineshape. Normalized, this scales as the inverse of the line width. The experimental result is that the  $T_2$  of the solute doesn't affect Bloch fitting, so we only include chemical exchange in the line width. Notice that the line width in Hz is needed for unit agreement.

For the inhomogeneous terms, we include elements 3 and 6 as these correspond to longitudinal magnetization. Thus, A and b become:

$$A = \begin{bmatrix} -\frac{1}{T_1 \text{ solvent}} - k_{ba}\chi & k_{ba} \\ k_{ba}\chi & -\frac{1}{T_1 \text{ solute}} - k_{ba} - \omega_{\text{nutatation}}^2 \cdot \frac{1}{k_{ba}} \end{bmatrix} \quad [\text{B.2a}]$$

$$b = \begin{bmatrix} \frac{(1-\chi)}{T_1 \text{ solvent}} \\ \frac{\chi}{T_1 \text{ solute}} \end{bmatrix} \quad [\text{B.2b}]$$

At steady state, the derivative of magnetization with respect to time is zero.

$$\frac{d}{dt}M_{ss} = AM_{ss} + b = 0 \quad [\text{B.3}]$$

Solving for steady state magnetization,  $M_{ss}$ :

$$M_{ss} = A^{-1}b \quad [\text{B.4}]$$

Solving symbolically using Mupad or Mathematica, the first element of  $M_{ss}$  corresponding to the magnetization of water is:

$$M_{ss} = \frac{\left(\omega_{\text{mutation}}^2 + k_{ba}^2 \cdot \left(1 + \chi \cdot \frac{T_{1 \text{ solvent}}}{T_{1 \text{ solute}}}\right)\right) + \frac{k_{ba}}{T_{1 \text{ solute}}}}{\left(\omega_{\text{mutation}}^2 + k_{ba}^2 \cdot \left(1 + \chi \cdot \frac{T_{1 \text{ solvent}}}{T_{1 \text{ solute}}}\right) + k_{ba} \cdot T_{1 \text{ solvent}} \cdot \chi \cdot \omega_{\text{mutation}}^2\right) + \frac{k_{ba}}{T_{1 \text{ solute}}}} \quad [\text{B.5}]$$

The second element, corresponding to the equilibrium magnetization of the solute, is irrelevant so it can be ignored.

Based on our work and previous results (1,2) the value for  $T_{1 \text{ solute}}$  is not relevant for CEST. Furthermore, for reasonable values of  $k_{ba}$  and  $T_{1 \text{ solute}}$ ,  $\frac{k_{ba}}{T_{1 \text{ solute}}}$  will be far less than the nutation rate squared or exchange rate squared. So we assume  $T_{1 \text{ solute}}$  is long enough that it does not affect a CEST experiment. Also, we assume the mole fraction  $\chi$  is much less than one. This is valid if the solute is much lower in concentration than 110 molar.

Thus the following:

$$M_{ss} = \frac{(\omega_{\text{nutation}}^2 + k_{ba}^2)}{(\omega_{\text{nutation}}^2 + k_{ba}^2 + k_{ba} \cdot T_{1 \text{ solvent}} \cdot \chi \cdot \omega_{\text{nutation}}^2)} \quad [\text{B.6}]$$

Simplifying:

$$M_{ss} = \frac{1}{\left(1 + \frac{k_{ba} \cdot T_{1 \text{ solvent}} \cdot \chi \cdot \omega_{\text{nutation}}^2}{\omega_{\text{nutation}}^2 + k_{ba}^2}\right)} \quad [\text{B.7}]$$

This is our result for  $M_{ss}$ . To verify, we compare our result to that of Dixon (74). We do this as follows:

$$\frac{M_{ss}}{M_0 - M_{ss}} = \frac{\frac{1}{\left(1 + \frac{k_{ba} \cdot T_{1 \text{ solvent}} \cdot \chi \cdot \omega_{\text{nutation}}^2}{\omega_{\text{nutation}}^2 + k_{ba}^2}\right)}}{1 - \frac{1}{\left(1 + \frac{k_{ba} \cdot T_{1 \text{ solvent}} \cdot \chi \cdot \omega_{\text{nutation}}^2}{\omega_{\text{nutation}}^2 + k_{ba}^2}\right)}} \quad [\text{B.8a}]$$

$$\frac{M_{ss}}{M_0 - M_{ss}} = \frac{1}{1 + \frac{k_{ba} \cdot T_{1 \text{ solvent}} \cdot \chi \cdot \omega_{\text{nutation}}^2}{\omega_{\text{nutation}}^2 + k_{ba}^2} - 1} \quad [\text{B.8b}]$$

$$\frac{M_{ss}}{M_0 - M_{ss}} = \frac{1}{\frac{k_{ba} \cdot T_{1 \text{ solvent}} \cdot \chi \cdot \omega_{\text{mutation}}^2}{\omega_{\text{mutation}}^2 + k_{ba}^2}} \quad [\text{B.8c}]$$

$$\frac{M_{ss}}{M_0 - M_{ss}} = \frac{\omega_{\text{mutation}}^2 + k_{ba}^2}{k_{ba} \cdot T_{1 \text{ solvent}} \cdot \chi \cdot \omega_{\text{mutation}}^2} \quad [\text{B.8d}]$$

$$\frac{M_{ss}}{M_0 - M_{ss}} = \frac{1}{k_{ba} \cdot T_{1 \text{ solvent}} \cdot \chi} + \frac{k_{ba}}{T_{1 \text{ solvent}} \cdot \chi \cdot \omega_{\text{mutation}}^2} \quad [\text{B.8e}]$$

Here we use the following definition:

$$R_{1 \text{ solvent}} \equiv \frac{1}{T_{1 \text{ solvent}}} \quad [\text{B.8f}]$$

$$\frac{M_{ss}}{M_0 - M_{ss}} = \frac{R_{1 \text{ solvent}}}{k_{ba} \cdot \chi} + \frac{k_{ba} \cdot R_{1 \text{ solvent}}}{\chi \cdot \omega_{\text{mutation}}^2} \quad [\text{B.8g}]$$

$$\frac{M_{ss}}{M_0 - M_{ss}} = \frac{k_{ba} \cdot R_{1 \text{ solvent}}}{k_{ba}^2 \cdot \chi} + \frac{k_{ba} \cdot R_{1 \text{ solvent}}}{\chi \cdot \omega_{\text{mutation}}^2} \quad [\text{B.8h}]$$

$$\frac{M_{ss}}{M_0 - M_{ss}} = \frac{k_{ba} \cdot R_{1 \text{ solvent}}}{\chi} \left( \frac{1}{k_{ba}^2} + \frac{1}{\omega_{\text{mutation}}^2} \right) \quad [\text{B.8i}]$$

This is the result of Dixon, and is our starting point for our linearized power response methods.

We have shown the correspondence between the Omega Plot and QUESP methods in chapter 2.

## **B.2. Derivation of QUEST from the Bloch McConnell Equations**

The derivation of the QUEST method is done by examining the eigenvalue of the A matrix that has the lowest magnitude. Since all eigenvalues are negative, this term determines the long term behaviour of the system. The eigenvector corresponding to this eigenvalue has a larger inner product with the vector corresponding to magnetization on water than it does to the vector corresponding to magnetization on the solute. In short, this is the value that is determined by the behaviour of magnetization on water as a function of time. The other eigenvalue corresponds to the loss of magnetization of the solute during irradiation.

We substitute  $T_{1 \text{ solute}}$  with  $T_{1 \text{ solvent}}$ . While this approximation is reasonable, it is not necessary. We only include this in an attempt to make the derivation less tedious.

$$A = \begin{bmatrix} -\frac{1}{T_{1 \text{ solvent}}} - k_{ba} \chi & k_{ba} \\ k_{ba} \chi & -\frac{1}{T_{1 \text{ solvent}}} - k_{ba} - \omega_{\text{mutation}}^2 \cdot \frac{1}{k_{ba}} \end{bmatrix} \quad [\text{B.9}]$$

The relevant eigenvalue is the following:

$$\lambda = \frac{1}{T_{1 \text{ solvent}}} + \frac{1}{2 \cdot k_{ba}} \cdot \left( -\sqrt{\left( k_{ba}^4 \cdot (1 + \chi)^2 + 2 \cdot k_{ba}^2 \cdot \omega_{\text{mutation}}^2 \cdot (1 - \chi) + \omega_{\text{mutation}}^4 \right)} \right. \\ \left. + k_{ba}^2 \cdot (1 + \chi) + \omega_{\text{mutation}}^2 \right) \quad [\text{B.10}]$$

We evaluate the radical in the vicinity of  $\chi \ll 1$ , which is true if the molarity of the solute is much less than 110 molar.

$$\text{radical}(\chi) = \text{radical}(\chi)|_{\chi=0} + \chi \cdot \left( \frac{d}{d\chi} \text{radical}(\chi) \right)|_{\chi=0} + O(\chi^2) \quad [\text{B.11a}]$$

$$\text{radical}(\chi) = \sqrt{\left( k_{ba}^4 + 2 \cdot k_{ba}^2 \cdot \omega_{\text{mutation}}^2 + \omega_{\text{mutation}}^4 \right)} \\ + \chi \cdot \frac{\left( 2 \cdot k_{ba}^4 - 2 \cdot k_{ba}^2 \cdot \omega_{\text{mutation}}^2 \right)}{\sqrt{\left( k_{ba}^4 + 2 \cdot k_{ba}^2 \cdot \omega_{\text{mutation}}^2 + \omega_{\text{mutation}}^4 \right)}} + O(\chi^2) \quad [\text{B.11b}]$$

$$\text{radical}(\chi) = \left( k_{ba}^2 + \omega_{\text{mutation}}^2 \right) \\ + \chi \cdot \frac{\left( 2 \cdot k_{ba}^4 - 2 \cdot k_{ba}^2 \cdot \omega_{\text{mutation}}^2 \right)}{\left( k_{ba}^2 + \omega_{\text{mutation}}^2 \right)} + O(\chi^2) \quad [\text{B.11c}]$$

Plugging this into the eigenvalue:

$$\lambda = - \left( \frac{1}{T_{1 \text{ solvent}}} + \frac{1}{2 \cdot k_{ba}} \cdot \left( - \left( \left( k_{ba}^2 + \omega_{\text{mutation}}^2 \right) + \chi \cdot \frac{\left( 2 \cdot k_{ba}^4 - 2 \cdot k_{ba}^2 \cdot \omega_{\text{mutation}}^2 \right)}{\left( k_{ba}^2 + \omega_{\text{mutation}}^2 \right)} \right) \right. \right. \\ \left. \left. + k_{ba}^2 \cdot (1 + \chi) + \omega_{\text{mutation}}^2 \right) \right) \quad [\text{B.12a}]$$

$$\lambda = - \left( \frac{1}{T_{1 \text{ solvent}}} + \frac{1}{2 \cdot k_{ba}} \cdot \left( - \left( \chi \cdot \frac{\left( 2 \cdot k_{ba}^4 - 2 \cdot k_{ba}^2 \cdot \omega_{\text{mutation}}^2 \right)}{\left( k_{ba}^2 + \omega_{\text{mutation}}^2 \right)} \right) \right) \right) \quad [\text{B.12b}]$$

Now we expand around mutation rate equal to exchange rate:

$$u = \left( \chi \cdot \frac{\left( 2 \cdot k_{ba}^4 - 2 \cdot k_{ba}^2 \cdot \omega_{\text{mutation}}^2 \right)}{\left( k_{ba}^2 + \omega_{\text{mutation}}^2 \right)} \right) \quad [\text{B.13a}]$$

$$u(\omega_{\text{mutation}}^2) = u(\omega_{\text{mutation}}^2)|_{\omega_{\text{mutation}}^2 = k_{ba}^2} \\ + \omega_{\text{mutation}}^2 \cdot \left( \frac{d}{d\omega_{\text{mutation}}^2} u(\omega_{\text{mutation}}^2) \right)|_{\omega_{\text{mutation}}^2 = k_{ba}^2} + O(\omega_{\text{mutation}}^4) \quad [\text{B.13b}]$$

$$u = \chi \cdot \omega_{\text{mutation}}^2 \cdot \left( \frac{\left( -2 \cdot k_{ba}^2 \right)}{\left( k_{ba}^2 + \omega_{\text{mutation}}^2 \right)} \right) \quad [\text{B.14a}]$$

$$u = -\chi \cdot \omega_{\text{nut}}^2 \simeq -\chi \cdot k_{ba}^2 \quad [\text{B.14b}]$$

$$\lambda = -\left(\frac{1}{T_{1 \text{ solvent}}} + \frac{1}{2 \cdot k_{ba}} \cdot (-(-\chi \cdot k_{ba}^2) + k_{ba}^2 \cdot \chi)\right) \quad [\text{B.14c}]$$

$$\lambda = -\left(\frac{1}{T_{1 \text{ solvent}}} + \frac{1}{2 \cdot k_{ba}} \cdot (2 \cdot k_{ba}^2 \cdot \chi)\right) \quad [\text{B.14d}]$$

$$\lambda = -(R_{1 \text{ solvent}} + k_{ba} \cdot \chi) \quad [\text{B.14e}]$$

Including boundary conditions, we get the following for Magnetization as a function of time:

$$M(t) = M_0 + (M_{ss} - M_0) \cdot (1 - \exp(-(R_{1 \text{ solvent}} + k_{ba} \cdot \chi) \cdot t)) \quad [\text{B.15a}]$$

$$\frac{M(t)-M_0}{M_0} = \left(\frac{M_{ss}-M_0}{M_0}\right) \cdot (1 - \exp(-(R_{1 \text{ solvent}} + k_{ba} \cdot \chi) \cdot t)) \quad [\text{B.15b}]$$

$$\frac{M(t)-M_0}{M_0} = \text{prefactor} \cdot (1 - \exp(-(R_{1 \text{ solvent}} + k_{ba} \cdot \chi) \cdot t)) \quad [\text{B.15c}]$$

This is the result of McMahon (1).

The additional assumptions here were  $T_{1 \text{ solvent}} = T_{1 \text{ solute}}$ , and  $\omega_{\text{nut}}^2 \simeq k_{ba}^2$ . We get the same result if the former assumption is wrong. The answer is inaccurate by a factor of as much as two if the latter assumption is wrong. This is consistent with our experimental results of CEST response to time at different nutation rates in chapter 3.

## REFERENCES

**Chapter 1**

1. Carr DH, Brown J, Bydder GM, Weinmann HJ, Speck U, Thomas DJ, Young IR. Intravenous chelated gadolinium as a contrast agent in NMR imaging of cerebral tumours. *Lancet*. 1984; 1(8375): 484-486.
2. Prince MR. Gadolinium enhanced MR aortography. *Radiology*. 1994; 191: 155-164.
3. Li SP, Padhani AR. Tumor response assessments with diffusion and perfusion MRI. *J. Magn. Reson. Imaging*. 2012; 35(4): 745-763.
4. Weissleder R, Ross BD, Rehemtulla A, Gambhir SS. *Molecular Imaging: Principles and Practice*. People's Medical Publishing House: Shelton CT, 2010.
5. Sullivan DC. Imaging as a quantitative science. *Radiology*. 2008; 248(2): 328-332.
6. Haake EM, Brown RW, Thompson MR, Venkatesan R. *Magnetic Resonance Imaging: Physical Principles and Sequence Design*. John Wiley & Sons: New York, 1999.
7. Ward KM, Aletras AH, Balaban RS. A new class of contrast agents for MRI based on proton chemical exchange dependent saturation transfer (CEST). *J. Magn. Reson*. 2000; 143(1): 79-87.
8. McMahon MT, Gilad AA, DeLiso MA, Berman SM, Bulte JW, van Zijl PC. New "multicolor" polypeptide diamagnetic chemical exchange saturation transfer (DIACEST) contrast agents for MRI. *Magn. Reson. Med*. 2008; 60(4): 803-812.
9. Zhang S, Merritt M, Woessner DE, Lenkinski RE, Sherry AD. PARACEST agents: modulating MRI contrast via water proton exchange. *Acc. Chem. Res*. 2003; 36(10): 783-790.
10. Liu G, Ali M, Yoo B, Griswold MA, Tkach JA, Pagel MD. PARACEST MRI with improved temporal resolution. *Magn. Reson. Med*. 2009; 61: 399-408.
11. Grad J, Bryant RG. Nuclear magnetic cross-relaxation spectroscopy. *J. Magn. Reson*. 1990; 90: 1-8.
12. Woessner DE, Zhang S, Merritt ME, Sherry AD. Numerical solution of the Bloch equations provides insights into the optimum design of PARACEST agents for MRI. *Magn. Reson. Med*. 2005; 53: 790-799.
13. Rourke DE. Solutions and linearization of the nonlinear dynamics of radiation damping. *Concept. Magnetic. Res*. 2002; 14(2): 112-129.
14. Earnst R, Bodenhausen G, Wokaun A. *Principles of Nuclear Magnetic Resonance in One and Two Dimensions*, Oxford University Press, Oxford, 1987.
15. Lauffer R. Paramagnetic metal complexes as water proton relaxation agents for NMR imaging: theory and design. *Chem. Rev*. 1987; 87: 901-927.
16. Liu G, Song X, Chan K Y, McMahon MT. Nuts and bolts of chemical exchange saturation transfer MRI, *NMR Biomed*. 2013; 26: 810-828.
17. Sheth VR, Liu G, Li Y, Pagel MD. Improved pH measurements with a single PARACEST MRI contrast agent, *Contrast Media Mol. Imaging*. 2012; 7: 26-34.
18. Henkelman M, Huang X, Xiang QS, Stanisiz GJ, Swanson SD, Bronskill MJ. Quantitative interpretation of magnetization transfer. *Magn. Reson. Med*. 1993; 29(6): 759-766.
19. Stancanella J, Terreno E, Castelli D, Cabella C, Uggeri F, Aime S. Development and validation of a smoothing-splines-based correction method for improving the analysis of CEST-MR images. *Contrast Media Mol. Imaging*. 2008; 3(4): 136-149.
20. Yadav NN, Chan KW, Jones CK, McMahon MT, van Zijl PC. Time domain removal of irrelevant magnetization in chemical exchange saturation transfer Z-spectra. *Magn. Reson. Med*. 2013; 70(2): 547-555.

21. Chappell MA, Groves AR, Whitcher B, Woolrich MW. Variational Bayesian inference for a nonlinear forward Model. *IEEE Trans. Signal Process.* 2009; 57(1): 223-226.
22. Liu G, Ali MM, Yoo B, Griswold MA, Tkach JA, Pagel MD. PARACEST MRI with improved temporal resolution. *Magn. Reson. Med.* 2009; 61(2): 399-408.
23. Shah T, Lu L, Dell KM, Pagel MD, Griswold MA, Flask CA. CEST-FISP: a novel technique for rapid chemical exchange saturation transfer MRI at 7 T. *Magn. Reson. Med.* 2011; 65(2): 432-437.
24. Soesbe TC, Togao O, Takahashi M, Sherry AD. SWIFT-CEST: a new MRI method to overcome  $T_2$  shortening caused by PARACEST contrast agents. *Magn. Reson. Med.* 2012; 68(3): 816-821.
25. Varma G, Lenkinski RE, Vinogradov E. Keyhole chemical exchange saturation transfer. *Magn. Reson. Med.* 2012; 68(4): 1228-1233.
26. Sun PZ, Zhou J, Sun W, Huang J, van Zijl PCM. Suppression of lipid artifacts in amide proton transfer imaging. *Magn. Reson. Med.* 2005; 54: 222-225.
27. Kim M, Gillen J, Landman A, Zhou J, van Zijl PCM. Water saturation shift referencing (WASSR) for chemical exchange saturation transfer (CEST) experiments. *Magn. Reson. Med.* 2009; 61(6): 1441-1450.
28. Jin T, Kim S. Quantitative chemical exchange sensitive MRI using irradiation with toggling inversion preparation. *Magn. Reson. Med.* 2012; 68(4): 1056-1064.
29. Zu Z, Janve VA, Li K, Does MD, Gore JC, Gochberg DF. Multi-angle ratiometric approach to measure chemical exchange in amide proton transfer imaging. *Magn. Reson. Med.* 2012; 68: 711-719.
30. Zu Z, Janve VA, Xu J, Does MD, Gore JC, Gochberg DF. A new method for detecting exchanging amide protons using chemical exchange rotation transfer. *Magn. Reson. Med.* 2013; 69: 637-647.
31. Vinogradov E, Soesbe TC, Balschi JA, Sherry AD, Lenkinski RE. pCEST: positive contrast using chemical exchange saturation transfer. *J. Magn. Reson.* 2012; 215: 64-73.
32. Vinogradov E, Zhang S, Lubag A, Balschi JA, Sherry AD, Lenkinski RE. On-resonance low  $B_1$  pulses for imaging of the effects of PARACEST agents. *J. Magn. Reson.* 2005; 176: 54-63.
33. Li AX, Suchy M, Li C, Gati JS, Meakin S, Hudson RHE, Menon RS, Bartha R. In vivo detection of MRI-PARACEST agents in mouse brain tumors at 9.4 T. *Magn. Reson. Med.* 2011; 66: 67-72.
34. Vinogradov E, He H, Lubag A, Balschi JA, Sherry AD, Lenkinski RE. MRI detection of paramagnetic chemical exchange effects in mice kidneys in vivo. *Magn. Reson. Med.* 2007; 58: 650-655.
35. Friedman JI, McMahon MT, Stivers JT, Van Zijl PCM. Indirect detection of labile solute proton spectra via the water signal using frequency-labeled exchange (FLEX) transfer. *J. Am. Chem. Soc.* 2010; 132: 1813-1815.
36. Yadav NN, Jones CK, Xu J, Bar-Shir A, Gilad AA, McMahon MT, van Zijl PCM. Detection of rapidly exchanging compounds using on-resonance frequency-labeled exchange (FLEX) transfer. *Magn. Reson. Med.* 2012; 68: 1048-1055.
37. Lin C, Yadav NN, Friedman JI, Ratnakar J, Sherry AD, van Zijl PCM. Using frequency-labeled exchange transfer to separate out conventional magnetization transfer effects from exchange transfer Effects When Detecting ParaCEST Agents. *Magn. Reson. Med.* 2012; 67: 906-911.
38. Song X, Gilad AA, Joel S, Liu G, Bar-Shir A, Liang Y, Gorelik M, Pekar JJ, van Zijl PCM, Bulte JWM, McMahon MT. CEST phase mapping using a length and offset VARied saturation (LOVARS) scheme. *Magn. Reson. Med.* 2012; 68: 1074-1086.

39. Närväinen J, Hubbard PL, Kauppinen RA, Morris GA. Z-spectroscopy with alternating-phase irradiation. *J. Magn. Reson.* 2010; 207: 242–250.
40. Lee J, Regatte RR, Jerschow A. Isolating chemical exchange saturation transfer contrast from magnetization transfer asymmetry under two-frequency RF irradiation. *J. Magn. Reson.* 2012; 215: 56–63.
41. Sun PZ. Simplified quantification of labile proton concentration-weighted chemical exchange rate ( $k(ws)$ ) with RF saturation time dependent ratiometric analysis (QUESTRA): normalization of relaxation and RF irradiation spillover effects for improved quantitative chemical exchange saturation transfer (CEST) MRI. *Magn. Reson. Med.* 2012; 67(4): 936–942.
42. McMahan MT, Gilad AA, Zhou J, Sun PZ, Bulte JWM, van Zijl PCM. Quantifying exchange rates in chemical exchange saturation transfer agents using the saturation time and saturation power dependencies of the magnetization transfer effect on the magnetic resonance imaging signal (QUEST and QUESP): pH calibration for poly-L-lysine and a starburst dendrimer. *Magn. Reson. Med.* 2006; 55: 836–847.
43. Dixon WT, Ren J, Lubag AJM, Ratnakar J, Vinogradov E, Hancu I, Lenkinski RE, Sherry AD. A concentration-independent method to measure exchange rates in PARACEST agents. *Magn. Reson. Med.* 2010; 63: 625–632.
44. Woessner DE, Zhang S, Merritt ME, Sherry AD. Numerical solution of the Bloch equations provides insights into the optimum design of PARACEST agents for MRI. *Magn. Reson. Med.* 2005; 53: 790–799.
45. Mubase K, Tainki N. Numerical solutions to the time-dependent Bloch equations revisited. *Magn. Reson. Imag.* 2011; 29: 126–131.
46. Yoo B, Pagel MD. A PARACEST MRI contrast agent to detect enzyme activity. *J. Am. Chem. Soc.* 2006; 128: 14032–14033.
47. Yoo B, Raam MS, Rosenblum RM, Pagel MD. Enzyme-responsive PARACEST MRI contrast agents: a new biomedical imaging approach for studies of the proteasome. *Contrast Media Mol. Imaging.* 2007; 2: 189–198.
48. Hingorani DV, Randtke EA, Pagel MD. A CatalyCEST MRI contrast agent that detects the enzyme-catalyzed creation of a covalent bond. *J. Am. Chem. Soc.* 2013; 135(17): 6396–6398.
49. Liu G, Li Y, Pagel MD. Design and characterization of a new irreversible responsive PARACEST MRI contrast agent that detects nitric oxide. *Magn. Reson. Med.* 2007; 58: 1249–1256.
50. Yoo B, Pagel MD. An overview of responsive MRI contrast agents for molecular imaging. *Front. Biosci. (Landmark Ed.)* 2008; 13: 1733–1752.
51. Aime S, Barge A, Castelli DD, Fedeli F, Mortillaro A, Nielsen FU, Terreno E. Paramagnetic Lanthanide(III) complexes as pH-sensitive chemical exchange saturation transfer (CEST) contrast agents for MRI applications. *Magn. Reson. Med.* 2002; 47(4): 639–648.
52. Sheth VR, Li Y, Chen LQ, Howison CM, Flask CA, Pagel MD. Measuring in vivo tumor pH with CEST-FISP MRI. *Magn. Reson. Med.* 2012; 67(3): 760–768.
53. Liu G, Li Y, Sheth VR, Pagel MD. Imaging in vivo extracellular pH with a single paramagnetic chemical exchange saturation transfer magnetic resonance imaging contrast agent. *Molec. Imaging.* 2012; 11(1): 47–57.
54. Zhang S, Merritt M, Woessner DE, Lenkinski RE, Sherry AD. ParaCEST agents: modulating MRI contrast via water proton exchange. *Acc. Chem. Res.* 2003; 36(10): 783–790.

## **Chapter 2**

1. Yoo B, Pagel MD. An overview of responsive MRI contrast agents for molecular imaging. *Front. Biosci.* 2007; 13: 1733-1752.
2. Liu G, Li Y, Sheth VR, Pagel MD. Imaging in vivo extracellular pH with a single PARACEST MRI contrast agent. *Molec. Imaging.* 2012; 11: 47-57.
3. Sun PZ, Sorensen AG. Imaging pH using the chemical exchange saturation transfer (CEST) MRI: Correction of concomitant RF irradiation effects to quantify CEST MRI for chemical exchange rate and pH. *Magn. Reson. Med.* 2008; 60: 390-397.
4. Sun PZ. Simultaneous determination of labile proton concentration and exchange rate utilizing optimal RF power: Radio frequency power (RFP) dependence of chemical exchange saturation transfer (CEST) MRI. *J. Magn. Reson.* 2010; 202:155-161.
5. Sun PZ, van Zijl PCM, Zhou J. Optimization of the irradiation power in chemical exchange dependent saturation transfer experiments. *J. Magn. Reson.* 2005; 175: 193-200.
6. Liu G, Ali, M, Yoo B, Griswold MA, Tkach JA, Pagel MD. PARACEST MRI with improved temporal resolution. *Magn. Reson. Med.* 2009; 61: 399-408.
7. Soesbe TC, Togao O, Takahashi M, Sherry AD. SWIFT-CEST: A new MRI method to overcome  $T_2$  shortening caused by PARACEST contrast agents. *Magn. Reson. Med.* 2012; 68: 816-821.
8. Woessner DE, Zhang S, Merritt ME, Sherry AD. Numerical solution of the Bloch equations provides insights into the optimum design of PARACEST agents for MRI. *Magn. Reson. Med.* 2005; 53: 790-799.
9. McMahon MT, Gilad AA, Zhou J, Sun PZ, Bulte JW, van Zijl PC. Quantifying exchange rates in chemical exchange saturation transfer agents using the saturation time and saturation power dependencies of the magnetization transfer effect on the magnetic resonance imaging signal (QUEST and QUESP): pH calibration for poly-L-lysine and a starburst dendrimer. *Magn. Reson. Med.* 2006; 55: 836-847.
10. Dixon WT, Ren J, Lubag AJM, Ratnakar J, Vinogradov E, Hancu I, Lenkinski RE, Sherry AD. A concentration-independent method to measure exchange rates in PARACEST agents. *Magn. Reson. Med.* 2010; 63: 625-632.
11. Ali MM, Liu G, Shah T, Flask CA, Pagel MD. Using two chemical exchange saturation transfer magnetic resonance imaging contrast agents for molecular imaging studies. *Acc. Chem. Res.* 2009; 42: 915-924.
12. Sun PZ, Wang E, Cheung JS, Zhang X, Benner T, Sorensen AG. Simulation and optimization of pulsed radio frequency irradiation scheme for chemical exchange saturation transfer (CEST) MRI---Demonstration of pH-weighted pulsed-amide proton CEST MRI in an animal model of acute cerebral ischemia. *Magn. Reson. Med.* 2011; 66: 1042-1048.
13. Sun PZ. Simplified quantification of labile proton concentration-weighted chemical exchange rate ( $k_{ws}$ ) with RF saturation time dependent ratiometric analysis (QUESTRA): Normalization of relaxation and RF irradiation spillover effects for improved quantitative chemical exchange saturation transfer (CEST) MRI. *Magn. Reson. Med.* 2012; 67: 936-942.
14. Ward KM, Aletras AH, Balaban RS. A new class of contrast agents for MRI based on proton chemical exchange dependent saturation transfer (CEST). *J. Magn. Reson.* 2000; 143: 79-87.
15. Zhang S, Merritt M, Woessner DE, Lenkinski RE, Sherry AD. PARACEST agents: modulating MRI contrast via water proton exchange. *Acc. Chem. Res.* 2003; 36: 783-790.
16. Lineweaver H, Burk D. Determination of enzyme dissociation constants. *J. Am. Chem.*

- Soc. 1934; 56: 658–666.
17. Hofstee BH. On the evaluation of the constants  $V_m$  and  $K_M$  in enzyme reactions. *Science* 1952; 116(3013): 329–331.
  18. Hanes CS. Studies on plant amylases: The effect of starch concentration upon the velocity of hydrolysis by the amylase of germinated barley. *Biochem. J.* 1932; 26(5): 1406–1421.
  19. Sheth VR, Liu G, Li Y, Pagel MD. Improved pH measurements with a single PARACEST MRI contrast agent. *Contrast Media Molec. Imaging.* 2012; 7: 26-34.
  20. Van Geet AL. Calibration of the methanol and glycol nuclear magnetic resonance thermometers with a static thermistor probe. *Anal. Chem.* 1968; 40: 2227-2229.
  21. Murase K, Tanki M. Numerical solutions to the time-dependent Bloch equations revisited. *Magn. Reson. Imaging* 2011; 29: 126-131.
  22. Tee YK, Khrapitchev AA, Sibson NR, Payne SJ, Chappell MA. Evaluating the use of a continuous approximation for model-based quantification of pulsed chemical exchange saturation transfer (CEST). *J. Magn. Reson.* 2012; 222: 88–95.
  23. Desmond KL, Stanisz GJ. Understanding quantitative pulsed CEST in the presence of MT. *Magn. Reson. Med.* 2012; 67: 979-990.
  24. Sun PZ, Farrar CT, Sorensen AG. Correction for artifacts induced by  $B_0$  and  $B_1$  field inhomogeneities in pH-sensitive chemical exchange saturation transfer (CEST) imaging. *Magn. Reson. Med.* 2007; 58: 1207-1215.
  25. Li Y, Sheth VR, Liu G, Pagel MD. A self-calibrating PARACEST MRI contrast agent that detects esterase enzyme activity. *Contrast Media Molec. Imaging.* 2011; 6: 219-228.

### **Chapter 3**

1. Yoo B, Pagel MD. An overview of responsive MRI contrast agents for molecular imaging. *Front. Biosci.* 2007; 13: 1733-1752.
2. Grad J, Bryant RG. Nuclear magnetic cross-relaxation spectroscopy. *J. Magn. Reson.* 1990; 90: 1–8.
3. Liu G, Li Y, Sheth VR, Pagel MD. Imaging in vivo extracellular pH with a single PARACEST MRI contrast agent. *Molec. Imaging* 2012; 11: 47-57.
4. Sun PZ, Sorensen AG. Imaging pH using the chemical exchange saturation transfer (CEST) MRI: Correction of concomitant RF irradiation effects to quantify CEST MRI for chemical exchange rate and pH. *Magn. Reson. Med.* 2008; 60: 390-397.
5. Sun PZ. Simultaneous determination of labile proton concentration and exchange rate utilizing optimal RF power: Radio frequency power (RFP) dependence of chemical exchange saturation transfer (CEST) MRI. *J. Magn. Reson.* 2010; 202: 155-161.
6. Sun PZ, van Zijl PCM, Zhou J. Optimization of the irradiation power in chemical exchange dependent saturation transfer experiments. *J. Magn. Reson.* 2005; 175: 193-200.
7. Liu G, Ali, M, Yoo B, Griswold MA, Tkach JA, Pagel MD. PARACEST MRI with improved temporal resolution. *Magn. Reson. Med.* 2009; 61: 399-408.
8. Soesbe TC, Togao O, Takahashi M, Sherry AD. SWIFT-CEST: A New MRI method to overcome  $T_2$  shortening caused by PARACEST contrast agents. *Magn. Reson. Med.* 2012; 68: 816-821.
9. Woessner DE, Zhang S, Merritt ME, Sherry AD. Numerical solution of the Bloch equations provides insights into the optimum design of PARACEST agents for MRI. *Magn. Reson. Med.* 2005; 53: 790–799.
10. McMahan MT, Gilad AA, Zhou J, Sun PZ, Bulte JW, van Zijl PC. Quantifying exchange

- rates in chemical exchange saturation transfer agents using the saturation time and saturation power dependencies of the magnetization transfer effect on the magnetic resonance imaging signal (QUEST and QUESP): pH calibration for poly-L-lysine and a starburst dendrimer. *Magn. Reson. Med.* 2006; 55: 836-847.
11. Dixon WT, Ren J, Lubag AJM, Ratnakar J, Vinogradov E, Hancu I, Lenkinski RE, Sherry AD. A concentration-independent method to measure exchange rates in PARACEST agents. *Magn. Reson. Med.* 2010; 63: 625–632.
  12. Ali MM, Yoo B, Pagel MD. Tracking the relative in vivo pharmacokinetics of nanoparticles with PARACEST MRI. *Molec. Pharmaceutics.* 2009; 6(5): 1409-1416.
  13. Sheth VR, Liu G, Li Y, Pagel MD. Improved pH measurements with a single PARACEST MRI contrast agent. *Contrast Media Molec. Imaging.* 2012; 7: 26-34.
  14. Murase K, Tanki M. Numerical solutions to the time-dependent Bloch equations revisited. *Magn. Reson. Imaging.* 2011; 29: 126-131.
  15. Randtke EA, Chen LQ, Corrales RA, Pagel MD. The Hanes-Woolf Linear QUEST method provides the most accurate determination of fast chemical exchange rates for CEST MRI contrast agents. *Proc ISMRM 2014*; 1908.
  16. Sun PZ. Simplified quantification of labile proton concentration-weighted chemical exchange rate ( $k_{ws}$ ) with RF saturation time dependent ratiometric analysis (QUESTRA): Normalization of relaxation and RF irradiation spillover effects for improved quantitative chemical exchange saturation transfer (CEST) MRI. *Magn. Reson. Med.* 2012; 67: 936-942.
  17. Ng MC, Hua J, Hu Y, Luk KD, Lam EY. Magnetization transfer (MT) asymmetry around the water resonance in human cervical spinal cord. *J. Magn. Reson. Imaging.* 2009; 29: 523–528.
  18. Ali MM, Liu G, Shah T, Flask CA, Pagel MD. Using two chemical exchange saturation transfer magnetic resonance imaging contrast agents for molecular imaging studies. *Acc. Chem. Res.* 2009; 42: 915-924.
  19. Van Geet AL. Calibration of the methanol and glycol nuclear magnetic resonance thermometers with a static thermistor probe. *Anal. Chem.* 1968; 40(14): 2227–2229.

#### **Chapter 4**

1. Zeng H, Huang W, Shi J, A covalently bonded  $AlQ_3/SiO_2$  hybrid material with blue light emission by a conventional sol-gel approach. *Chem. Commun.* 2006; 8: 880-881.
2. Liu F, Rao BS, Nunzi JM, A dye functionalized silver–silica core–shell nanoparticle organic light emitting diode. *Org. Electron.* 2011; 12(7): 1279-1284.
3. Schulz-Ekloff G, Wöhrle D, van Duffel B, Schoonheydt RA, Chromophores in porous silicas and minerals: preparation and optical properties. *Microporous Mesoporous Mater.* 2002; 51(2): 91-138.
4. Lim Y, Park Y, Kang Y, Jang DY, Kim JH, Kim J, Sellinger A, Yoon DY, Hole injection/transport materials derived from heck and sol-gel chemistry for application in solution-processed organic electronic devices. *J. Am. Chem. Soc.* 2011; 133(5): 1375-1382.
5. Corrales LR, Song J, Van Ginhoven RM, Jonsson H, Computational studies of self-trapped excitons in silica. defects in  $SiO_2$  and related dielectrics, Springer Science + Business Media, Dordrecht, 2000; 2: 329-337.
6. Van Ginhoven RM, Jonsson H, Corrales LR, Characterization of exciton self-trapping in amorphous silica. *J. Non-Cryst. Solids*, 2006; 352(23-25): 2589-2595.
7. Song J., Van Ginhoven RM, Corrales LR, Jónsson H., Self-trapped excitons at the quartz(0001) surface. *Faraday Discuss.*, 2000; 117: 303-311.

8. Parr RG, Density functional theory. *Annu. Rev. Phys. Chem.* 1983; 34: 631-656.
9. Eyring H. The activated complex in chemical reactions. *J. Chem. Phys.*, 1935. 3(2): 107-115.
10. Zener C, Non-adiabatic crossing of energy levels. *Proc. R. Soc. London, Ser. A.* 1932; 137(833): 696-702.
11. Wittig C. The Landau-Zener formula. *J. Phys. Chem. B.* 2005; 109(17): 8428-8230.
12. Born M, Fock V, Beweis des adiabatenatzes. *Z. Phys.* 1928; 51(3-4): 165-180.
13. Förster T. Zwischenmolekulare energiewanderung und fluoreszenz. *Ann. Phys.* 1948; 437(1-2): 55-75.
14. Dexter DL, A theory of sensitized luminescence in solids. *J. Chem. Phys.* 1953; 21(5): 836-850.
15. Marcus RA, Sutin N, Electron transfers in chemistry and biology. *Biochim. Biophys. Acta.* 1985; 811(3): 265-322.
16. Griscom DL. Self-trapped holes in amorphous-silicon dioxide. *Phys. Rev. B.* 1989; 40(6): 4224-4227.
17. Tenenbaum M, Pollard H. *Ordinary Differential Equations.* Dover, New York, 1985: 82-90
18. Marcus RA, Chemical and electrochemical electron-transfer theory. *Annu. Rev. Phys. Chem.* 1964; 15(1): 155-196.
19. Mulliken RS, Electronic population analysis on LCAO-MO molecular wave functions. *J. Chem. Phys.* 1955; 23(10): 1833-1840.
20. Crank J, Nicolson PA. Practical method for numerical evaluation of solutions of partial differential equations of the heat-conduction type. *Proc. Cambridge Philos. Soc.* 1947; 43(1): 50-67.
21. Itoh C, Tanimura K, Itoh N, Optical studies of self-trapped excitons in SiO<sub>2</sub>. *Journal of Physics C-Solid State Physics*, 1988; 21(26): 4693-4702.
22. Trukhin AN, Excitons in SiO<sub>2</sub> - a review. *J. Non-Cryst. Solids.* 1992; 149(1-2): 32-45.
23. Kalceff MAS, Thorogood GJ, Short KT, Charge trapping and defect segregation in quartz. *J. of Appl. Phys.* 1999; 86(1): 205-208.
24. Skuja L, The Origin of the intrinsic 1.9 eV luminescence band in glassy SiO<sub>2</sub>. *J. Non-Cryst. Solids* 1994; 179: 51-69.
25. Fisher AJ, Hayes W, Stoneham AM, Theory of the structure of the self-trapped exciton in quartz. *Journal of Physics-Condensed Matter.* 1990; 2(32): 6707-6720.
26. Ricci D, Pacchioni G, Szymanski MA, Shluger AL, Stoneham AM, Modeling disorder in amorphous silica with embedded clusters: The peroxy bridge defect center. *Phys. Rev. B.* 2001; 64(22): 224104-224111.
27. Corrales LR, Song J, Van Ginhoven RM, Jónsson H, *Computational studies of self-trapped excitons in silica, defects in SiO<sub>2</sub> and related dielectrics: Science and Technology*, Springer, Netherlands, 2000. 329-337.
28. Du JC, Corrales LR; Tsemekhman K; Bylaska EJ, Electron, hole and exciton self-trapping in germanium doped silica glass from DFT calculations with self-interaction correction. *Nucl Instrum Methods B.* 2007; 255(1): 188-194.
29. Glinka YD, Lin SH, Hwang LP, Chen YT, Tolk NH, Size effect in self-trapped exciton photoluminescence from SiO<sub>2</sub>-based nanoscale materials. *Phys. Rev. B.* 2001; 64(8): 085421-085431
30. Dunning TH, Gaussian basis sets for use in correlated molecular calculations. I. The atoms boron through neon and hydrogen. *J. Chem. Phys.*, 90 (2): 1007-23
31. Woodward RB, Structure and the Absorption Spectra of  $\alpha,\beta$ -Unsaturated Ketones. *J. Am. Chem. Soc.* 63 (4): 1123-1126

## **Chapter 5**

1. Woessner DE, Zhang S, Merritt ME, Sherry AD. Numerical solution of the Bloch equations provides insights into the optimum design of PARACEST agents for MRI. *Magn. Reson. Med.* 2005; 53: 790–799.
2. McMahon MT, Gilad AA, Zhou J, Sun PZ, Bulte JWM, van Zijl PCM. Quantifying exchange rates in chemical exchange saturation transfer agents using the saturation time and saturation power dependencies of the magnetization transfer effect on the magnetic resonance imaging signal (QUEST and QUESP): pH calibration for poly-L-lysine and a starburst dendrimer. *Magn. Reson. Med.* 2006; 55: 836–847.
3. Dixon WT, Ren J, Lubag AJM, Ratnakar J, Vinogradov E, Hancu I, Lenkinski RE, Sherry AD. A concentration-independent method to measure exchange rates in PARACEST agents. *Magn. Reson. Med.* 2010; 63: 625–632.
4. Ali MM, Liu G, Shah T, Flask CA, Pagel MD. Using two chemical exchange saturation transfer magnetic resonance imaging contrast agents for molecular imaging studies. *Acc. Chem. Res.* 2009; 42(7): 915–924.
5. Randtke EA, Chen LQ, Corrales LR, Pagel MD. The Hanes-Woolf linear QUESP method improves the measurements of fast chemical exchange rates with CEST MRI. *Magn. Reson. Med.* 2013; In press.
6. Randtke EA, Chen LQ, Corrales LR, Pagel MD. The reciprocal linear QUEST analysis method facilitates the measurements of chemical exchange rates with CEST MRI. *Contrast Media. Molec. Imaging.* 2013; In press.
7. Shah T, Lu L, Dell KM, Pagel MD, Griswold MA, Flask CA. CEST-FISP: a novel technique for rapid chemical exchange saturation transfer MRI at 7 T. *Magn. Reson. Med.* 2011; 65(2): 432-437.
8. Chappell MA, Groves AR, Whitcher B, Woolrich MW. Variational Bayesian inference for a nonlinear forward Model. *IEEE Trans. Signal Process.* 2009; 57(1): 223-226
9. Stancanella J, Terreno E, Castelli D, Cabella C, Uggeri F, Aime S. Development and validation of a smoothing-splines-based correction method for improving the analysis of CEST-MR images. *Contrast Media Mol. Imaging.* 2008; 3(4): 136-49.
10. Sun PZ, Benner T, Kumar A, Sorensen AZ. An investigation of optimizing and translating pH-sensitive pulsed-chemical exchange saturation transfer (CEST) imaging to a 3 T clinical scanner. *Magn. Reson. Med.* 2008; 60(4): 834–841.
11. Liu G, Song S, Chan KY, McMahon MT. Nuts and bolts of chemical exchange saturation transfer MRI. *NMR Biomed.* 2013; 26: 810-828.
12. Sheth VR, Li Y, Chen LQ, Howison CM, Flask CA, Pagel MD. Measuring in vivo tumor pHe with CEST-FISP MRI. 2012; *Magn. Reson. Med.* 67: 760–768.
13. Chen LQ, Howison C, Jeffery J, Robey I, Kuo PH, Pagel MD. Evaluations of extracellular pH within in vivo tumors using acidoCEST MRI. *Magn. Reson. Med.*, epub ahead of print.
14. Liu G, Li Y, Sheth VR, Pagel MD. Imaging in vivo extracellular pH with a single paramagnetic chemical exchange saturation transfer magnetic resonance imaging contrast agent. *Molecular Imaging.* 2011: 1-11.
15. Yoo B, Sheth VR, Howison CM, Douglas MJK, Pineda CT, Maine EA, Baker AF, Pagel MD. Detection of in vivo enzyme activity with CatalyCEST MRI. *Magn. Reson. Med.* 2013; In Press.
16. Yoo B, Pagel MD. A PARACEST MRI contrast agent to detect enzyme activity. *J. Am. Chem. Soc.* 2006; 128(43): 14032-14033.
17. Yoo B, Raam MS, Rosenblum RM, Pagel MD. Enzyme-responsive PARACEST MRI contrast agents: a new biomedical imaging approach for studies of the proteasome. *Contrast Media Mol. Imaging.* 2007; 2: 189-198.

18. Sheth VR, Liu G, Li Y, Pagel MD, Improved pH measurements with a single PARACEST MRI contrast agent. *Contrast Media Mol. Imaging.* 2012; 7: 26-34.
19. Longo DL, Dastrù W; Digilio G, Keupp J, Langereis S, Lanzardo S, Prestigio S, Steinbach O, Terreno E, Uggeri F, Aime S. Iopamidol as a responsive MRI-chemical exchange saturation transfer contrast agent for pH mapping of kidneys: In vivo studies in mice at 7 T. 2011; *Magn. Reson. Med.* 65: 202–211.

### **Appendix A**

1. Eyring H. The activated complex in chemical reactions. *J. Chem. Phys.* 1935; 3(2): 107-115.
2. Zener C. Non-adiabatic crossing of energy levels. *Proceedings of the Royal Society of London Series a-Containing Papers of a Mathematical and Physical Character.* 1932; 137(833): 696-702.
3. Förster T, Zwischenmolekulare energiewanderung und fluoreszenz. *Annalen der Physik.* 1948; 437(1-2): 55-75.
4. Dexter DL. A theory of sensitized luminescence in solids. *J. Chem. Phys.* 1953; 21(5): 836-850.
5. Marcus RA, Sutin N. Electron transfers in chemistry and biology. *Biochimica. Et. Biophysica. Acta.* 1985; 811(3): 265-322.
6. Wittig C. The Landau-Zener formula. *Journal of Physical Chemistry B,* 2005. 109(17): 8428-8430.

### **Appendix B**

1. McMahon MT, Gilad AA, Zhou J, Sun PZ, Bulte JWM, van Zijl PCM. Quantifying exchange rates in chemical exchange saturation transfer agents using the saturation time and saturation power dependencies of the magnetization transfer effect on the magnetic resonance imaging signal (QUEST and QUESP): pH calibration for Poly-L-Lysine and a starburst dendrimer. *Magn. Reson. Med.* 2006; 55: 836–847.
2. Dixon WD, Ren J, Lubag AJM, Ratnakar J, Vinogradov E, Hancu I, Lenkinski RE, Sherry AD. A concentration-independent method to measure exchange rates in PARACEST agents. 2010; *Magn. Reson. Med.* 63: 625–632.